

1995

Image fusion using multi-resolution decomposition and LMMSE filter

Jaewon Yim
Iowa State University

Follow this and additional works at: <https://lib.dr.iastate.edu/rtd>

 Part of the [Electrical and Electronics Commons](#)

Recommended Citation

Yim, Jaewon, "Image fusion using multi-resolution decomposition and LMMSE filter " (1995). *Retrospective Theses and Dissertations*. 10744.

<https://lib.dr.iastate.edu/rtd/10744>

This Dissertation is brought to you for free and open access by the Iowa State University Capstones, Theses and Dissertations at Iowa State University Digital Repository. It has been accepted for inclusion in Retrospective Theses and Dissertations by an authorized administrator of Iowa State University Digital Repository. For more information, please contact digirep@iastate.edu.

INFORMATION TO USERS

This manuscript has been reproduced from the microfilm master. UMI films the text directly from the original or copy submitted. Thus, some thesis and dissertation copies are in typewriter face, while others may be from any type of computer printer.

The quality of this reproduction is dependent upon the quality of the copy submitted. Broken or indistinct print, colored or poor quality illustrations and photographs, print bleedthrough, substandard margins, and improper alignment can adversely affect reproduction.

In the unlikely event that the author did not send UMI a complete manuscript and there are missing pages, these will be noted. Also, if unauthorized copyright material had to be removed, a note will indicate the deletion.

Oversize materials (e.g., maps, drawings, charts) are reproduced by sectioning the original, beginning at the upper left-hand corner and continuing from left to right in equal sections with small overlaps. Each original is also photographed in one exposure and is included in reduced form at the back of the book.

Photographs included in the original manuscript have been reproduced xerographically in this copy. Higher quality 6" x 9" black and white photographic prints are available for any photographs or illustrations appearing in this copy for an additional charge. Contact UMI directly to order.

UMI

**A Bell & Howell Information Company
300 North Zeeb Road, Ann Arbor, MI 48106-1346 USA
313/761-4700 800/521-0600**



Image fusion using multi-resolution decomposition and LMMSE filter

by

Jaewon Yim

A Dissertation Submitted to the
Graduate Faculty in Partial Fulfillment of the
Requirements for the Degree of
DOCTOR OF PHILOSOPHY

Department: Electrical and Computer Engineering
Major: Electrical Engineering (Communication and Signal Processing)

Approved:

Signature was redacted for privacy.

In Charge of Major Work

Signature was redacted for privacy.

For the Major Department

Signature was redacted for privacy.

For the Graduate College

Iowa State University
Ames, Iowa

1995

UMI Number: 9531811

UMI Microform 9531811

Copyright 1995, by UMI Company. All rights reserved.

This microform edition is protected against unauthorized
copying under Title 17, United States Code.

UMI

300 North Zeeb Road
Ann Arbor, MI 48103

TABLE OF CONTENTS

	Page
CHAPTER I. INTRODUCTION	1
1.1 Data Fusion of NDE Images	1
1.2 Literature Review	5
1.3 Dissertation Summary	7
CHAPTER II. IMAGE DEGRADATION IN ULTRASONIC AND EDDY CURRENT IMAGING APPLICATIONS	8
2.1 Overview of NDE	8
2.2 Electromagnetic NDE	11
2.3 Principles of Eddy Current Inspection	11
2.4 Differential Eddy Current Inspection	17
2.5 Multiple Frequency Eddy Current Techniques	21
2.6 Ultrasonic Test Methods	24
2.7 Degradation in Ultrasonic Images	29
2.8 Conventional Envelope Detection of Ultrasonic A-scan Signals	33
2.9 Improved Envelope Detection of Ultrasonic A-scan Signals	34
2.10 Interpolation of Ultrasonic A-scan Signals	35
2.11 Degradation in Eddy Current Images	38
CHAPTER III. IMAGE FUSION USING NEURAL NETWORKS	40
3.1 Pixel-level Fusion	40
3.2 Image Fusion Using Neural Networks	42
3.3 Experimental Results	48
CHAPTER IV. MULTIPLE INPUT LINEAR MINIMUM MEAN SQUARE ERROR FILTER	54
4.1 LMMSE Filter for Multiple Input System	54
4.2 LMMSE Filter for the System with Multiple Inputs with Additive Noise	56

4.3 LMMSE Filter for a System with Multiple Degenerated Inputs with Additive Noise	60
4.4 Mean Square Error for a Multiple Input LMMSE Filter with Additive Noise	68
4.5 Multiple Input LMMSE Filter for the Two-Dimensional Discrete Case	71
4.6 Experimental Verification	71
CHAPTER V. DATA FUSION USING MULTI-RESOLUTION DECOMPOSITION TECHNIQUES	75
5.1 Two Input Multi-resolution Filter	75
5.2 Multi-resolution Decomposition	77
5.3 Multi-resolution Decomposition Using Orthogonal Transforms	82
5.4 Fusion in Transform Domain	87
5.5 Wavelet Based Decomposition	92
5.6 Decomposition and Reconstruction Algorithm in Two Dimensions	100
5.7 Image Fusion Using Wavelet Transform	105
CHAPTER VI. CONCLUSIONS	106
6.1 Summary of Dissertation	106
6.2 Future Work	107
BIBLIOGRAPHY	109

LIST OF TABLES

	Page
Table 2.1: Depth of penetration, δ , (<i>mm</i> unit)	23

LIST OF FIGURES

	Page
Figure 2.1: The general structure of an NDE system.	10
Figure 2.2: Directions of primary and induced current relating to an alternating current carrying coil over a conducting material.	12
Figure 2.3: Complex impedance plane trajectory.	13
Figure 2.4: Bridge circuit used to measure impedance changes in eddy current probe.	14
Figure 2.5: Impedance plane trajectory of a coil over a non-ferromagnetic specimen with and without defect.	15
Figure 2.6: Typical differential eddy current probe.	18
Figure 2.7: Typical eddy current scanning system.	24
Figure 2.8: Typical ultrasonic pulse echo system.	27
Figure 2.9: B-scan display.	27
Figure 2.10: Typical ultrasonic imaging system.	28
Figure 2.11: A-scan signal in the time domain.	30
Figure 2.12: Spectrum of the A-scan signal.	30
Figure 2.13: Sampled version of the A-scan signal.	31
Figure 2.14: Block diagram of an interpolator that increases the sampling rate by L .	37
Figure 2.15: Model of the eddy current scanning scheme.	39

Figure 3.1:	MAX and MIN image in the pixel domain. a) Eddy current image; b) Ultrasonic image; c) Image obtained by selecting the maximum valued pixels; d) Image obtained by selecting the minimum valued pixels; e) Differentiated image; f) Averaged image.	41
Figure 3.2:	Multilayer perceptron network used for fusing images.	44
Figure 3.3:	Radial basis function network.	45
Figure 3.4:	Test specimen 1 used to obtain ultrasonic and eddy current images.	49
Figure 3.5:	Images used for fusion. a) Raw ultrasonic image data obtained with 60 MHz transducer; b) Raw eddy current image with 8 kHz excitation.	49
Figure 3.6:	Fused images using MLP and RBF network. a) Fused image obtained using MLP network with 2 hidden layer nodes; b) Fused image obtained using RBF network with 2 hidden layer nodes; c) Fused image obtained using RBF network with 5 hidden layer nodes and K-means algorithm for identifying the centers.	51
Figure 3.7:	Test specimen 2 used for obtaining eddy current images.	52
Figure 3.8:	Fusion of multifrequency eddy current images using an RBF network. a) Low frequency (6 kHz) eddy current image; b) High frequency (20 kHz) eddy current image; c) Fused image obtained with RBF network employing K-means algorithm to determine the 5 centers.	53
Figure 4.1:	Model for linear signal fusion.	55
Figure 4.2:	Multiple input LMMSE filter without degradation.	56
Figure 4.3:	Model for computing the cross-correlation for multiple terminal outputs.	62

Figure 4.4:	Multiple input LMMSE filtered image. a) Original image; b) Degraded image 1 with additive noise; c) Degraded image 2 with additive noise; d) Multiple input LMMSE filtered image.	73
Figure 4.5:	Comparison with one input LMMSE filter. a) 1-input LMMSE filtered image of Figure 4.3 (b); b) 1-input LMMSE filtered image of Figure 4.3 (c); c) Average of images shown in (a) and (b).	74
Figure 5.1:	Pyramidal image structure for one-dimensional signal.	79
Figure 5.2:	Pyramidal image structure for two-dimensional signal.	80
Figure 5.3:	Vector decomposition.	81
Figure 5.4:	Scale-space resolution.	82
Figure 5.5:	Ultrasonic image and eddy current image. a) Ultrasonic image with noise; b) Eddy current image with noise.	89
Figure 5.6:	Sub-band images for ultrasonic image.	90
Figure 5.7:	Sub-band images for eddy current.	91
Figure 5.8:	Ratio of spectra of ultrasonic and eddy current images. a) Ratio of spectrum of ultrasonic / eddy current images; b) Ratio of spectrum of eddy current / ultrasonic images.	93
Figure 5.9:	Fused image obtained using transform domain techniques employing a 4x4 block.	94
Figure 5.10:	Fused image obtained using transform domain techniques employing a 6x6 block.	94
Figure 5.11:	Fused image obtained using transform domain techniques employing a 8x8 block.	95

Figure 5.12:	Scale and wavelet functions used. a) Wavelet function $\psi(x)$; b) Scale function $\phi(x)$.	98
Figure 5.13:	QMF for forward wavelet transform.	99
Figure 5.14:	QMF for inverse wavelet transform.	99
Figure 5.15:	Sub-band wavelet images for the ultrasonic image.	101
Figure 5.16:	Sub-band wavelet images for the eddy current image.	102
Figure 5.17:	Fused image obtained using wavelet transformation employing a 4x4 block.	103
Figure 5.18:	Fused image obtained using wavelet transformation employing a 6x6 block.	103
Figure 5.19:	Fused image obtained using wavelet transformation employing a 8x8 block.	104

ACKNOWLEDGMENTS

I would like to express my deep gratitude to my advisor, Dr. Satish S. Udpa, for his invaluable guidance, support and encouragement throughout the graduate program. He is a respectable person for me not only as a professor but also as a senior of life.

I would like to extend my thanks to Dr. Lalita Udpa and Dr. William Lord for sharing their rich knowledge and helpful discussions.

I would also like to appreciate Dr. J. Davison, Dr. L. Miller and Dr. M. Mina for willfully taking the time to serve on my graduate committee.

I would particularly like to express my thanks to my parents and family for their encouragement and support.

CHAPTER I

INTRODUCTION

1.1 Data Fusion of NDE Images

The subject of data fusion has received significant attention in recent years. The objective of signal processing is to extract as much information as possible from the given input signal, which is usually derived from several sensors. Research on the subject of data fusion has been motivated by a desire to obtain more comprehensive information about the system being analyzed by employing the strategy of combining information from multiple sensors [1]. In practice it is often possible to employ different combinations of sensors. Choices may include using multiple sensors that are either identical or different. The latter case may involve the use of sensors that cover different spectral domains or employ completely dissimilar physical phenomena. For example, visible light and infra-red cameras using similar sensing mechanisms and generating similar type of data can be used as image acquisition devices. Similarly data from very different type of sensors, such as visual and touch sensors, can be combined together in applications such as robot motion sensing. Since there is considerable freedom with regard to the choice of sensors, there is confusion and ambiguity with regard to terminology associated with data fusion. This dissertation confines its attention to those approaches that employ multiple sensors to extract more comprehensive information.

Data fusion algorithms can be broadly classified as either phenomenological or non-phenomenological. Phenomenological algorithms utilize a knowledge of the underlying physical processes as a basis for deriving the procedure for fusing data. Several investigators are pursuing such approaches [2]. However, such methods are likely to be difficult to derive and cumbersome to implement. Non-phenomenological approaches, in contrast, tend to ignore the physical process and attempt to fuse information using the statistics associated with individual segments of data.

We can classify the non-phenomenological methods of data fusion into four different categories: signal level fusion, pixel level fusion, feature level fusion, and symbol level fusion [3]. Signal level fusion methods are usually applicable when the sensors have identical or similar characteristics, or when the relationship between the signals from different sensors is explicitly known. Pixel level fusion methods can be applied when sensors are used to generate data in the form of images. The statistical characteristics of the images combined with information concerning the relationship between the sensors is used to develop the fusion strategy. This dissertation focuses attention on data fusion techniques at the pixel level. In all subsequent discussions, the term image fusion will be used to denote image fusion at the pixel level. Feature level fusion implies the fusion of a reduced set of data representing the signal, called features. Features are an abstraction of the raw data intended to provide a reduced set that accurately and concisely represents the original data. The process of transforming the raw data into a feature vector is called feature extraction. Symbol level fusion represents the highest level of fusion. Such techniques call

for extracting abstract elements of information called symbols. The symbols are manipulated using reasoning as a basis to generate better information. Examples of application of symbol level fusion methods include the familiar knowledge based and decision tree method based systems. Higher levels fusion approaches are usually employed when the diversity of sensors is greater.

As an example of a different category of data fusion, knowledge based techniques such as those involving expert systems and logical templates can be used [4]. Knowledge based techniques may be based on either raw sensor data or extracted features. In either case there are two common features of knowledge based methods, (1) techniques for representing knowledge and (2) inference methods to process information to reach a conclusion.

Potential benefits of data fusion include more accurate characterization and often an ability to observe features that are otherwise difficult to perceive with a single sensor. The benefits are closely connected to the notion of redundant and complementary information [3]. We witness redundancy in information when sensors observe the same features from the test specimen. The fusion of such overlapping data improves the signal to noise ratio (SNR) and contributes directly to enhancing the characterization accuracy. In contrast, the fusion of complementary information allows features in the specimen to be observed that would otherwise not be seen. If the features observed are from different dimensions (as would be the case if we wish to fuse data from a heterogeneous sensor environment), the information provided by each sensor constitutes a subset of the features forming the

subspace in the feature space. The identification of the appropriate feature space for processing data from multiple sensors represents a major challenge. Another challenge to contend is the task of registration, since the features derived from each complementary sensor are from different dimensions.

This dissertation presents several new pixel level fusion algorithms that combine information from several sensors. Interesting applications involving the use of these algorithms for fusing information from nondestructive evaluation sensors are also presented.

The objective of nondestructive evaluation (NDE) is to detect and evaluate the severity of flaws in a test specimen without destroying its usefulness. NDE techniques rely largely on the interaction between some form of energy and the test specimen to provide information on the condition of the material. The type of energy utilized in the inspection process is related to the NDE method. Nearly all types of energy have been used in NDE, including electromagnetic, acoustic, x-ray and optical energy [16]. Ultrasonic methods use mechanical vibrations that propagate through the material under test. Energy scattered from the flaws provide information about the defect in the material. Similarly radiography methods use x-rays, gamma rays or even neutron beams to image the specimen.

Many NDE imaging technologies have been developed to detect flaws. Each technology offers its own set of advantages and disadvantages. As an example, ultrasonic imaging techniques offer excellent resolution. However, the method is sensitive to a wide variety of measurement conditions, including surface roughness and coupling. In contrast,

eddy current techniques do not require a couplant and are relatively insensitive to surface roughness conditions. The disadvantages associated with the eddy current method lies in its poor resolution capabilities. Although eddy current methods offer excellent flaw detection capabilities, they are not an effective method for characterizing small flaws due to their poor resolution characteristics. It is, therefore, obvious that a method that combines the advantages of both methods can be a powerful tool.

The objective of this research program is to develop methodologies for synergistically combining information from images generated using multiple nondestructive evaluation technologies. More specifically, this dissertation presents new techniques for combining acoustic microscopy and eddy current images to obtain a composite image of the object. It is anticipated that the resulting composite image is superior in some manner relative to the image obtained using either of the two techniques. The work done here indicates that the resulting image offers both superior resolution relative to the eddy current image as well as improved flaw detectability and SNR relative to the ultrasonic image.

1.2 Literature Review

Research in the field on data fusion is an ongoing activity that has resulted in the development of a number of interesting algorithms. As an example, Akerman [6], Huntsberger and Jawerth [10] use the pyramidal technique while Haberstroh and Kadar [7] use multilayer perceptron for multi-spectral data fusion.

Akerman uses a Gaussian pyramid decomposition technique to fuse monochrome TV and infrared images. A five-by-five Gaussian operator is repeatedly used to decompose the images. A Laplacian pyramid is then created by computing the differences between each layer in the Gaussian pyramid and an interpolated version of the image in the next layer. Candidate pixels are then identified from the layered images on the basis of a predetermined criterion. By reversing the image decomposition process, Akerman obtains the fused image.

Huntsberger and Jawerth [10] use two dimensional wavelet transforms to decompose images to generate multiresolution decomposition images. Logical operations are used to select / combine pixels at the each level of the decomposed pyramid.

Haberstroh and Kadar [7] use neural networks to discriminate between heavy and light objects from three band infrared surveillance data.

In addition to these non-phenomenological fusion methods which ignores the physical process, several investigators are pursuing phenomenological algorithms utilizing a knowledge of the underlying physical processes as a basis for deriving the procedure for fusing data [2]. However, such methods are likely to be difficult to derive and cumbersome to implement.

This dissertation presents several image fusion algorithms. The first set of algorithms are based on neural networks that involve training with exemplars. The second class of algorithms use a linear minimum mean square error approach for fusing information. Finally, the dissertation focuses its attention on the use of multiresolution techniques for combining information.

1.3 Dissertation Summary

This dissertation is concerned with developing efficient fusion techniques for NDE applications.

Chapter II presents a brief description of NDE imaging technology with special emphasis on eddy current and ultrasonic inspection techniques. The chapter reviews signal degradation mechanisms relating to each NDE imaging method, and introduces several useful methods for compensating or reducing those degradation effects.

Chapter III describes image fusion methods based on neural networks. Algorithms showing the use of multilayer perceptrons and radial basis function neural networks for enhancing NDE images are presented. Chapter IV introduces a multiple input linear minimum mean square error filter and shows several examples validating the approach. Chapter V presents image fusion methods using multi-resolution decomposition techniques based on both Fourier and two-dimensional wavelet transforms to decompose NDE images and reconstruct the fused image. Chapter VII summarizes the work described in the dissertation and presents several concluding remarks.

CHAPTER II

IMAGE DEGRADATION IN ULTRASONIC AND EDDY CURRENT IMAGING APPLICATIONS

This chapter presents a brief description of NDE imaging techniques with a special emphasis on eddy current and ultrasonic inspection methods. This chapter also reviews the image degradation processes associated with ultrasonic and eddy current inspection methods, and presents several techniques to compensate or reduce distortion.

2.1 Overview of NDE

Product evaluation and inspection for maintenance is an integral part of all manufacturing processes. The inspection procedure is crucial since we can not exclude the possibility of critical defects in any product.

There are two alternate approaches to testing; one is destructive while the other is nondestructive. Destructive testing can be divided into two basic categories. The first method performs tests under the most adverse conditions in which the products are likely to be used. These tests focus on the product's common failure point to guarantee safety margins of the product [12]. The other is environmental testing which is done under real life conditions, to evaluate the durability of the product. While the samples of the destructive tests are often destroyed and discarded, the objective of nondestructive testing (NDT) is to inspect and evaluate materials or products without adversely affecting their usability [13]. In this respect, the practical benefits of nondestructive inspection are

obvious. Also, compared to destructive testing methods which can be performed on only selected samples of the product, NDT techniques can be applied to every sample to find defects.

NDT serves not only to ensure quality in manufacturing processes but also to monitor the reliability and safety of the product after continued use, throughout its operational life. While NDT implies the testing procedure itself, the term non-destructive evaluation (NDE) is used to describe all the activities involved in obtaining a full description of the condition of the specimen. From this, a decision is made on the usability of the tested item based on pre-defined standards or background information.

NDE has gained in importance as a result of the rapid technological progress made during the past half-century in areas such as aerospace and nuclear energy, in which there are high risks, and strict precautions are required to avoid catastrophic failure. In order to meet the requirements of the diverse range of applications, a variety of basic physical principles have been used for NDE. In general, all methods of NDE rely on some form of energy as a probing source to interact with the specimen under test and produce an output response signal which is then analyzed and interpreted in terms of specimen properties. A general NDE procedure involves five essential steps as shown in Figure 2.1 [14], which includes energy source, input transducer, test specimen, output transducer, and signal processing step.

The method of testing is chosen depending on factors such as the type of material and its dimensions, the testing environment, the region of interest, e.g. whether internal or

surface defects are sought, and the environment for data acquisition and processing. Often, a combination of two or more methods may be required for the complete inspection of an object. This does not imply that they may be regarded as being alternative techniques because one of the methods can be used to complement another or to verify the findings of the other.

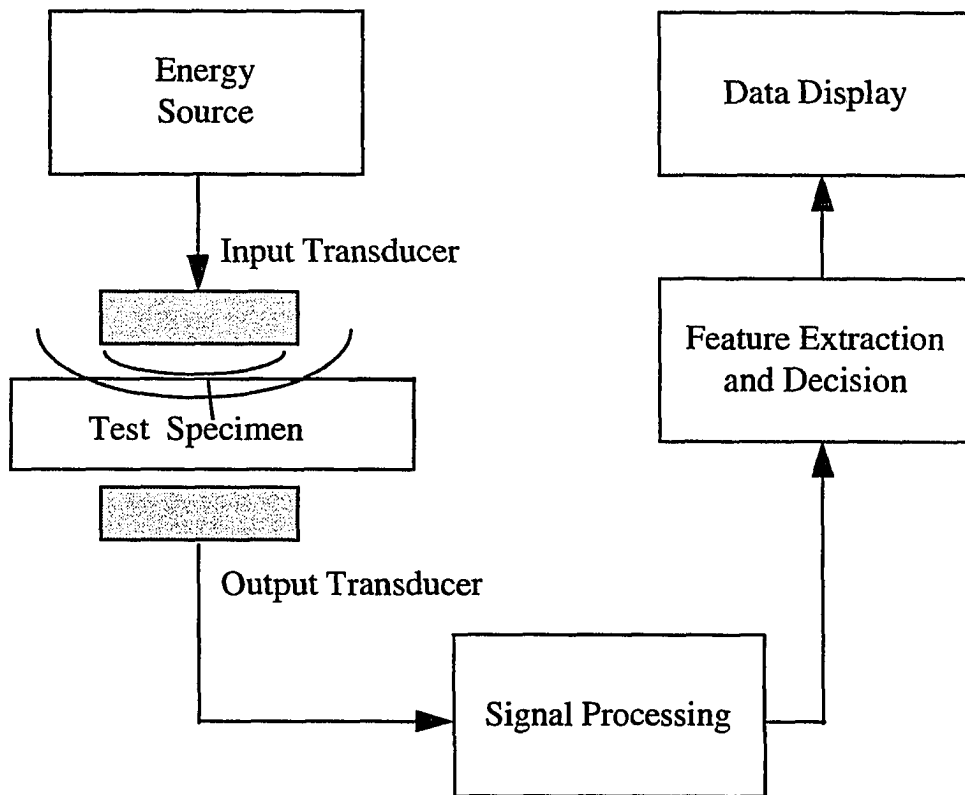


Figure 2.1. The general structure of an NDE system.

2.2 Electromagnetic NDE

Electromagnetic NDE methods include magnetic particle inspection, the magnetic flux leakage method, eddy current method, DC(direct current) and AC(alternating current) potential drop methods, and the microwave method. Magnetic particle and magnetic flux methods are normally used only for testing ferromagnetic materials. The eddy current methods are normally restricted to the testing of electrically conducting specimens. Microwave methods are usually confined to examining dielectric materials while potential drop methods can be used for testing semiconductors as well as good electrical conductors. The electromagnetic methods cover a wide range of frequencies from DC to millimeter waves. However, the common electromagnetic techniques are limited to active DC, residual and eddy current forms of excitation; all low frequency phenomena for which the displacement current effects can be neglected [15].

2.3 Principles of Eddy Current Inspection

The eddy current NDE method is based on the interaction between time varying electromagnetic fields and conductive materials. When a coil is excited by an alternating current source and placed near a conducting material, the magnetic field that is generated by the coil induces a current in the conducting material. The induced current is called eddy current. According to Lenz's law, the emf and induced current are in such a direction as to tend to oppose the change which produces them [18]. Figure 2.2 illustrates this phenomena.

Therefore, for a non-ferromagnetic material, the net flux linkages of the coil decreases due to the opposing field [19]. Since the self-inductance of the coil is defined as flux linkages per ampere, the inductance of the coil changes. If a defect exists or if there is a change in the material characteristics, the eddy currents are distorted resulting in a change in the value as shown in Figure 2.3. Several methods are used to measure the impedance of the eddy current probe coil.

In eddy current methods [17-25], a low frequency (typically below 10 MHz) electromagnetic field produced by a coil carrying an alternating current, forms the excitation source. The excitation levels are usually low and therefore for ferromagnetic materials, the operating point is around the origin of the B/H curve. When the coil is brought close to an electrically conducting test object, the time-varying magnetic field interacts with the test object according to the Maxwell-Faraday law,

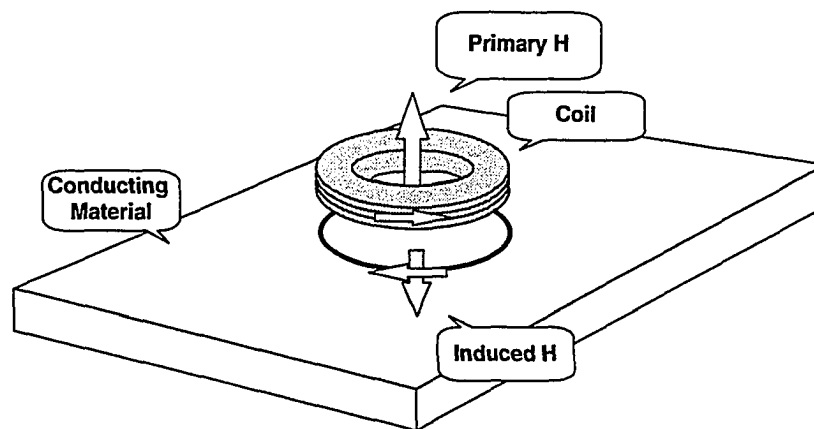


Figure 2.2. Directions of primary and induced current relating to an alternating current carrying coil over a conducting material. (after Udpa [17])

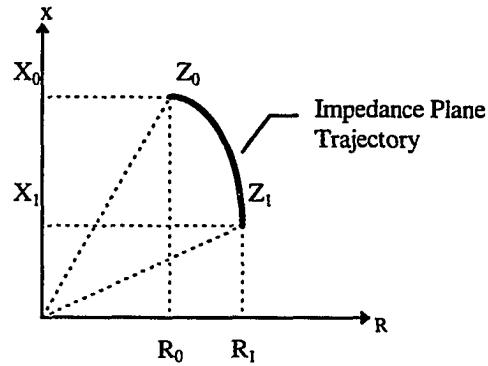


Figure 2.3. Complex impedance plane trajectory. (after Udpa[17])

$$\oint_c \vec{E} \cdot d\vec{l} = - \iint_s \vec{B} \cdot d\vec{s} \quad (2.1)$$

thus inducing eddy currents in the medium. These secondary currents produce their own magnetic field which opposes the changes in primary field in accordance with Lenz's law. In the case of a non-ferromagnetic specimen, this results in a reduction in the net flux linkages associated with the coil which, by definition, reduces the inductance of the coil. The resistance of the coil, on the other hand, increases because of eddy current losses within the material. The impedance of the excitation coil in air would therefore be different from that of the coil in the vicinity of the specimen. For ferromagnetic materials, counteracting the decrease in inductance due to the influence of eddy currents induced in the specimen is the increase in inductance owing to the higher permeability of the material. The latter effect is more predominant and consequently the inductance of the coil increases when it is brought close to a ferromagnetic specimen. The change in inductance is accompanied by an increase in resistance due to the eddy current losses. Since the eddy current distribution is

influenced by discontinuities or anomalies in the material their presence alters the impedance of the coil and all the electromagnetic properties of the test specimen affect the impedance of the coil. The changes in the complex probe impedance can be measured by an appropriate AC bridge as shown in Figure 2.4 and these measurements can be analyzed to estimate the surface and bulk properties of the specimen.

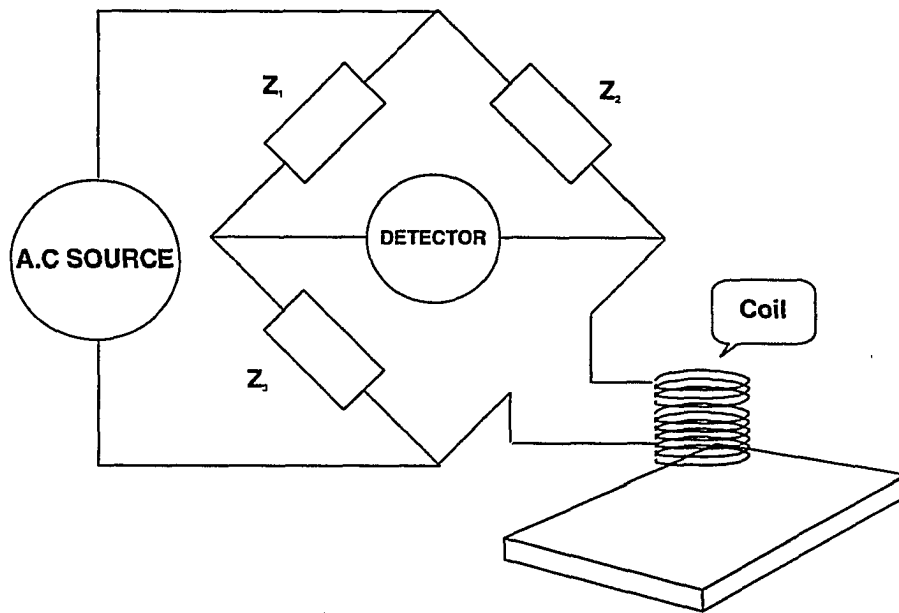


Figure 2.4. Bridge circuit used to measure impedance changes in eddy current probe.

(after Udpa [17])

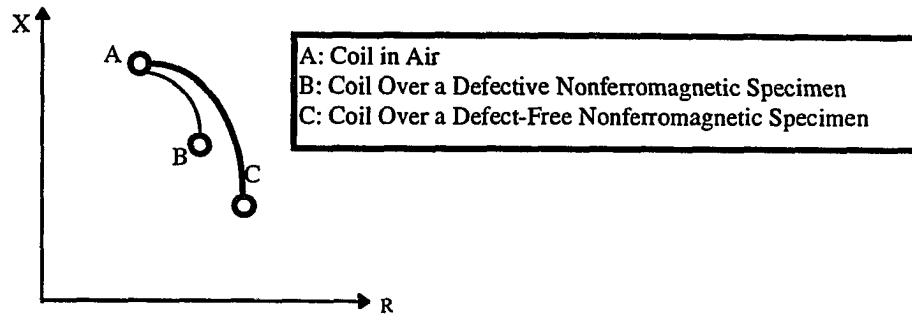


Figure 2.5. Impedance plane trajectory of a coil over a non-ferromagnetic specimen with and without defect. (after Udpa[17])

In practice, the variation in impedance is often displayed on a two dimensional complex plane. Since the horizontal and vertical data can be interpreted as the resistive and reactive components respectively of the complex impedance under steady state AC conditions, the eddy current test signal obtained is referred to as the impedance plane trajectory. Figure 2.5 shows the liftoff impedance plane trajectories of a coil over non-ferromagnetic and ferromagnetic specimens [21].

However, there are some difficulties in using an absolute coil. The factors that affect the eddy current characteristics are not only material and dimensional properties but also coil properties such as magnitude and frequency of the excitation current, geometry of the coil, liftoff, and core material properties. This abundance of properties affecting the test means that the effects of multiple properties may be superimposed. Isolating the effect of any one particular property can be very difficult. The coil impedance changes due to defects are often very small compared to the quiescent value of the coil impedance so that it can be difficult to detect such small changes. Changes in the coil parameters due to

environmental effects (e.g. temperature variations) can often mask changes due to defects, making signal interpretation very difficult. For this reason, many methods have been developed, among them the use of phase sensitive techniques, pulsed excitation [22,23], and multi-frequency and multi-parameter methods [51-53]. A variation of the absolute probe, which also overcomes these difficulties, is the differential eddy current probe.

Another difficulty in eddy current testing is due to the skin effect phenomenon. The skin effect restricts the deep penetration of eddy currents into conducting, ferromagnetic materials so that the conventional eddy current method is classified as a surface defect detection technique. In the testing of underground pipelines, for example, where an inner diameter (I.D.) eddy current probe is preferred due to the limitation of accessibility, this effect may limit the eddy current method to the detection of I.D. defects and prevent the detection of outer diameter (O.D.) defects if the wall thickness of the pipe is large enough. For this reason, the magnetic saturation technique using a permanent magnet has been developed to reduce the relative permeability of the tube to unity and increase the penetration depth [30-33]. Another breakthrough is the use of the remote field eddy current technique which is equally sensitive to both I.D. and O.D. defects [27].

2.4 Differential Eddy Current Inspection

A typical differential eddy current probe used for inspecting tubes is shown in Figure 2.6 [17]. In this method, two identical coils mounted on a common axis as the tube but spaced apart by a small distance, form the two arms of a bridge circuit which is initially nulled with the probe located in a defect-free segment of the tube. When the coil arrangement is moved past a narrow axisymmetric O.D. defect, whose width is considerably less than the spacing between the coils, the leading coil faces the defect first. The presence of the defect causes a variation in the coil impedance which in turn causes an imbalance in the bridge circuit. The bridge error signal, which is linked to the difference between the impedance of the two coils, is then used to obtain a trajectory. Similarly, when the trailing coil faces the defect, the change in impedance causes an imbalance in the bridge circuit. But, this time, the imbalance signal is in an opposite direction relative to that caused by the leading coil. During the intervening period when neither of the coils face the defect, the impedance trajectory remains stationary at the origin.

The differential nature of the probe makes the arrangement relatively insensitive to environmental effects. In addition, the differential connection results in the cancellation of the quiescent value of the coil impedance thereby highlighting the variations rather than the absolute value of the impedance. This makes measurement relatively easy. The differential probe, however, suffers from a disadvantage in that in the case of a long uniform defect running along the length of the tube, the changes in the differential impedance occur only at

the ends of the defect. This may be misinterpreted as two small defects instead of one long defect [17].

The equations that govern eddy current inspection can be derived from Maxwell's equations [46],

$$\nabla \times \mathbf{H} = \mathbf{J} + \frac{\partial \mathbf{D}}{\partial t} \quad (2.2)$$

$$\nabla \times \mathbf{E} = -\frac{\partial \mathbf{B}}{\partial t} \quad (2.3)$$

$$\nabla \cdot \mathbf{B} = 0 \quad (2.4)$$

$$\nabla \cdot \mathbf{D} = \rho \quad (2.5)$$

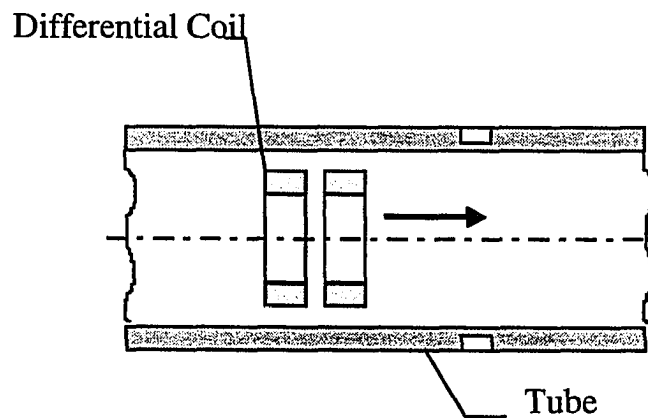


Figure 2.6. Typical differential eddy current probe.

For a linear, homogeneous, and isotropic conducting material, the following constitutive relations apply:

$$\mathbf{B} = \mu\mathbf{H} \quad (2.6)$$

$$\mathbf{D} = \epsilon\mathbf{E} \quad (2.7)$$

The conducting current density is:

$$\mathbf{J} = \sigma\mathbf{E} \quad (2.8)$$

At the quasi-static frequencies of interest, the displacement current term is negligible [5] and, consequently, equation (2.2) can be rewritten as:

$$\nabla \times \mathbf{H} = \mathbf{J} \quad (2.9)$$

Taking the curl of equation (2.9) and applying equation (2.8), we have:

$$\begin{aligned} \nabla \times (\nabla \times \mathbf{H}) &= \nabla \times \sigma\mathbf{E} \\ &= \sigma(\nabla \times \mathbf{E}) \end{aligned} \quad (2.10)$$

Using equation (2.3),

$$\nabla \times (\nabla \times \mathbf{H}) = -\sigma \frac{\partial \mathbf{B}}{\partial t} \quad (2.11)$$

Using the vector identity,

$$\nabla \times (\nabla \times \mathbf{H}) = \nabla \cdot (\nabla \cdot \mathbf{H}) - \nabla^2 \mathbf{H} \quad (2.12)$$

$$\nabla \cdot (\nabla \cdot \mathbf{H}) - \nabla^2 \mathbf{H} = -\sigma \frac{\partial \mathbf{B}}{\partial t} \quad (2.13)$$

Using equation (2.6),

$$\nabla \cdot \left(\nabla \cdot \frac{\mathbf{B}}{\mu} \right) - \nabla^2 \frac{\mathbf{B}}{\mu} = -\sigma \frac{\partial \mathbf{B}}{\partial t} \quad (2.14)$$

$$-\nabla^2 \frac{\mathbf{B}}{\mu} = -\sigma \frac{\partial \mathbf{B}}{\partial t} \quad (2.15)$$

$$-\nabla^2 \mathbf{H} = -\sigma \mu \mathbf{H} \quad (2.16)$$

Equation (2.16) constitutes the governing partial differential equation. Using a similar strategy, we can derive the governing equation for the electric field intensity and the current density:

$$\nabla^2 \mathbf{E} = \mu \sigma \mathbf{E} \quad (2.17)$$

$$\nabla^2 \mathbf{J} = \mu \sigma \mathbf{J} \quad (2.18)$$

The governing equation in this case, where the displacement current term can be negligible due to low operating frequencies (up to few MHz), is a parabolic diffusion equation given by

$$\nabla \times \frac{1}{\mu} (\nabla \times \bar{\mathbf{A}}) = \bar{\mathbf{J}}_s - \sigma \frac{\partial \bar{\mathbf{A}}}{\partial t} \quad (2.19)$$

where \bar{J}_s is an AC source current density. In a linear, isotropic, AC steady state case, it reduces to an elliptic partial differential equation,

$$\nabla \times \frac{1}{\mu} (\nabla \times \bar{A}) = -\mu \bar{J}_s + j\omega\sigma \bar{A} \quad (2.20)$$

Equation (2.20) assumes the Coulomb gauge, which is automatically satisfied in axisymmetric cases. The output NDE signal sought is the differential impedance and the impedance plane trajectory that is formed as the differential EC probe passes the defect.

2.5 Multiple Frequency Eddy Current Techniques

Another common difficulty in eddy current testing is due to the skin effect phenomenon. Eddy currents have a tendency to concentrate near the surface adjacent to the coil. This is popularly called *skin effect*. The skin effect equation [46] derived from Maxwell's equation by using the solenoidal property of steady currents ($\nabla \cdot \bar{J} = 0$), can be written as

$$\nabla^2 \bar{J} = \mu\sigma \frac{\partial \bar{J}}{\partial t} \quad (2.21)$$

where σ is the conductivity. This equation describes mathematically, the tendency for eddy currents to stay at the surface of conductors. As a simple example, in the case of an infinite AC current sheet over a conducting half-space, the current density solution to equation (2.21) is given by

$$J = J_0 \exp\left(-\frac{x}{\delta}\right) \sin\left(\omega t - \frac{x}{\delta}\right) \quad (2.22)$$

where $\omega = 2\pi f$ is the angular frequency, J_0 is the current density at the surface of the half-space, and δ is the depth of penetration or skin depth

$$\delta = (\pi f \mu \sigma)^{-1/2} \quad (2.23)$$

at which the current density drops to 36.8% of the value at the surface, J_0 and the phase of the current density lags that of J_0 by one radian. Although the exact value is not known for complex NDE geometries, the skin depth for a half-space of aluminum is estimated as 2.59×10^{-3} meters for an excitation frequency of 1 kHz, using the above expression. The corresponding value for steel is 5×10^{-4} meters. Therefore, eddy current methods are limited to the detection of flaws close to the surface even though low excitation frequencies may help extend the penetration depth to a certain degree.

From equation (2.23), we find that the skin depth is inversely proportional to the square root of the frequency. Table 2.1 shows typical values of skin depth for several materials [16].

As depicted in Table 2.1, at low frequencies the energy diffuses deeper into the conductor. Thus, eddy current techniques using low excitation frequencies are more sensitive to deeper defects. The method is sensitive to shallow defects when the frequency is increased. The multiple frequency eddy current NDE technique exploits the above property.

Table 2.1. Depth of penetration, δ , (*mm* unit).

Material	Excitation Frequency		
	1 kHz	10 kHz	50 kHz
Copper	2.00	0.64	0.28
Aluminum	2.65	0.84	0.04
Titanium	12.00	3.80	1.67
Cast Steel	0.50	0.15	0.07
Graphite	45.00	13.00	6.20
Zirconium	12.00	3.50	1.90

Multi-frequency eddy current inspection techniques involve testing at two or more excitation frequencies. Low frequency measurements are used to image defects that are located, not only at shallow depths, but also deep in the material. Higher frequency measurements are performed to image defects located at relatively shallow depths only. The two signals can be combined, not only to obtain a more comprehensive information about the specimen, but also to eliminate other artifacts such as those introduced by variations in probe lift-off. Using several frequencies, we obtain signals that contain information relating to a variety of depth ranges. Appropriate transformations can then be applied to selectively eliminate artifacts in the signal. This technique may be useful in reducing several types of extraneous or unwanted artifacts in eddy current signals.

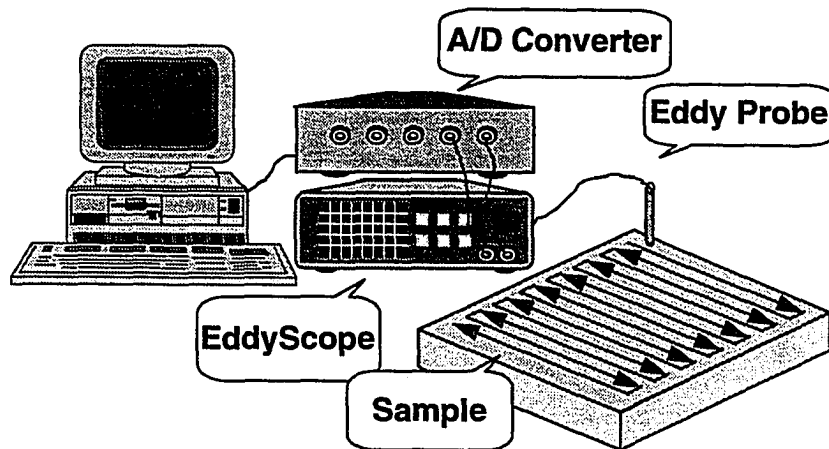


Figure 2.7. Typical eddy current scanning system.

Figure 2.7 depicts a typical scanning system used to obtain an eddy current image. The eddy scope is used to drive the probe and measure the change in its impedance. The impedance change is sampled and quantized using a high resolution A/D converter for further analysis. The results are displayed by the computer.

2.6 Ultrasonic Test Methods

Ultrasonic waves are caused by mechanical vibrations that occur because of the elastic properties of the material. These waves are induced by the vibration of particles in the material. When the particle vibration is sinusoidal, the wavelength, λ , is related to the velocity of the wave, c , in the material [47].

$$f = c\lambda$$

(2.24)

where f is the frequency of the vibration; i.e., the number of oscillations of the particle per second. Because of the material's elastic properties, the velocity of the wave is a function of the material's elastic property. Thus, the wavelength of the acoustic signal varies for different materials.

If a wave particle vibrates in the direction the wave is traveling, the wave is called a longitudinal or compressed wave. Such waves can propagate through solids, liquids and gases. In solid materials, the wave particle can vibrate at right angles to the direction in which the wave is traveling. Called a shear or transverse wave [48], this wave has a slower velocity than longitudinal waves. Shear waves cannot propagate through liquids. Also, depending on the situation, various types of surface waves can be generated in solid materials.

Ultrasonic waves can be generated using a number of methods, but in most non-destructive testing applications, piezoelectric transducers are used as both transmitter and receiver probes. A piezoelectric material has the property that produces electric charges on the surface when it is deformed by external pressure. If the pressure is reversed, the polarity of electric charges is reversed. If a piezoelectric material is placed between two electrodes and an electric field is applied, the material changes shape. This is called an inverse piezoelectric effect. While utilizing the effect, we can apply alternating electric current to the piezoelectric plate and generate mechanical oscillation. There are many varieties of materials that display piezoelectric properties. Natural crystals, such as quartz and lithium

sulphate, and fabricated polycrystalline ceramics, such as barium titanate, can be used as piezoelectric materials.

The ultrasonic wave is generated by applying an electrical pulse to the transmitter probe. The probe produces a short ultrasonic pulse that is propagated into the specimen through a coupling medium (Figure 2.8). The reflected portion of the ultrasonic wave returning to the transducer results in a small alternating voltage that is then fed to the amplifier. The amplified signal can be displayed on the CRT (cathode ray tube). This amplified signal provides both time of flight information as well as indication of the strength of the echo from discontinuities in the path of the ultrasonic wave. Normally, we observe echoes from the specimen's surface, the bottom surface, and the flaw. A one-dimensional display of the signal is called the A-Scan. The ultrasonic signal can be rectified and a peak detection operation performed to obtain a single maximum in each pulse.

The information can be displayed in other formats on the CRT screen. The B-Scan represents a cross-sectional view of the object on a plane that is normal to the surface of the probe scan as shown in Figure 2.9. The gray level of the image pixel is proportional to the strength of the echo. C-Scans show the plan view of the test specimen at a selected location in the specimen. In order to produce a C-Scan, the probe is mechanically scanned over the surface.

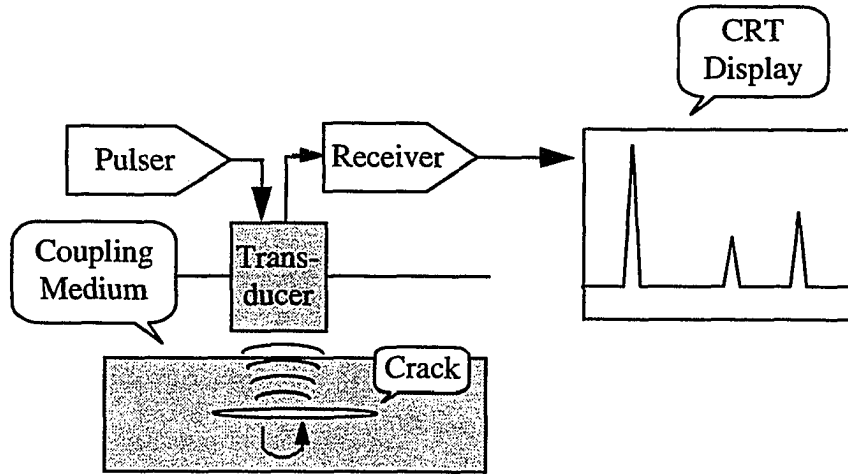


Figure 2.8. Typical ultrasonic pulse echo system.

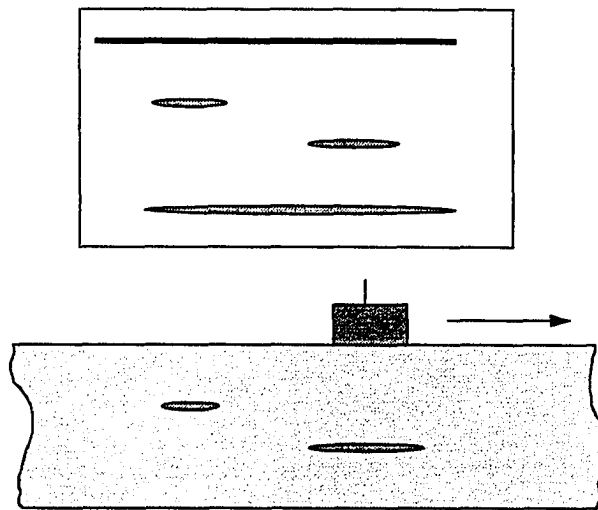


Figure 2.9 B-scan display.

The signals are windowed and the peak value of the signal within the window is estimated. An image whose gray levels are proportional to the peak values in the window is called a C-Scan. In order to ensure that the energy is effectively coupled into the material, a couplant is used. In acoustic microscope applications, the transducer and the specimens are immersed in a liquid and the ultrasonic probe is then scanned parallel to the specimen surface. The image that is generated resembles a radiograph. However, it does not contain any data relating to the depth of the flaw, in contrast to A- and B-Scan displays. Figure 2.10 shows a typical scanning system employed for obtaining ultrasonic images. A pulser/receiver is used to drive the piezo-electric transducer that is immersed in a water tank. The echo signal is amplified by the pulser/receiver and then fed to the analog-to-digital (A/D) converter prior to being transferred to a computer for generating the two-dimensional C-Scan image.

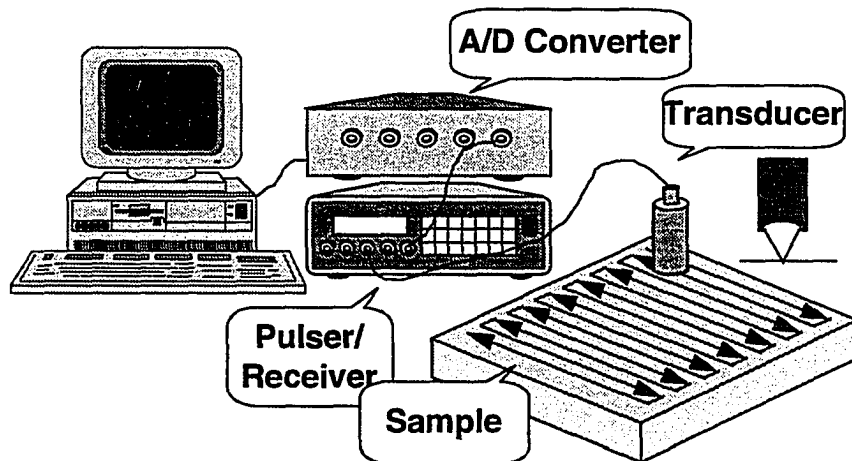


Figure 2.10. Typical ultrasonic imaging system.

The acoustic microscope responds to different properties in the object under examination from those responded to by the optical microscope. Since acoustic waves are related to mechanical properties, the contrast of the microscope is determined by variations in elasticity, density, and acoustic attenuation in the medium. The acoustic wave may not be transparent to the material although it may be transparent to light. Likewise acoustic waves can penetrate optically opaque materials. Another difference between acoustic microscope and X-ray systems is that conventional optical microscope and X-ray equipment are designed to use incoherent illumination with phase insensitive detectors, while acoustic inspection techniques tend to employ coherent methods and acoustic receiving transducers are phase sensitive.

2.7 Degradation in Ultrasonic Images

The ultrasonic A-scan signal is converted to the pixel value at each position and the inspection is repeated while the scanning is performed over a 2-dimensional area to construct an image. The 2D image is constructed from the A/D converted ultrasonic RF signal by associating the peak value with the gray level of the pixel at that point. There are two potential sources of noise in the imaging process. One is A/D converter quantization error involved in representing the amplitude of the signal while the other is related to uncertainty introduced due to sampling. Figure 2.11 and Figure 2.12 show examples of an A-scan signal in the time and frequency domain respectively. Figure 2.13 shows the effect of sampling the A-scan signal.

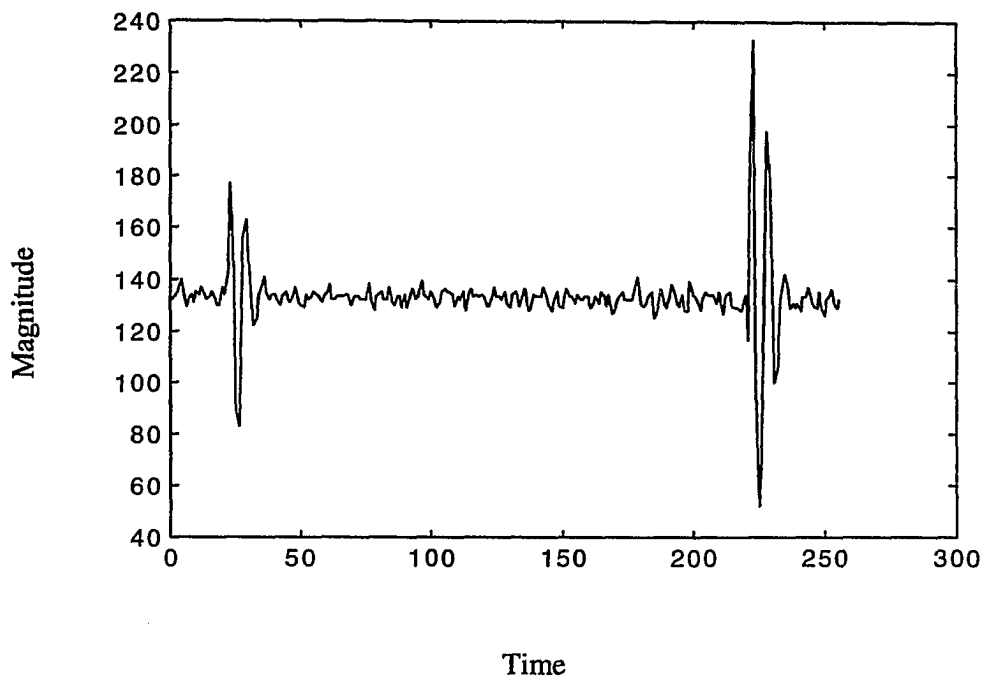


Figure 2.11. A-scan signal in the time domain.

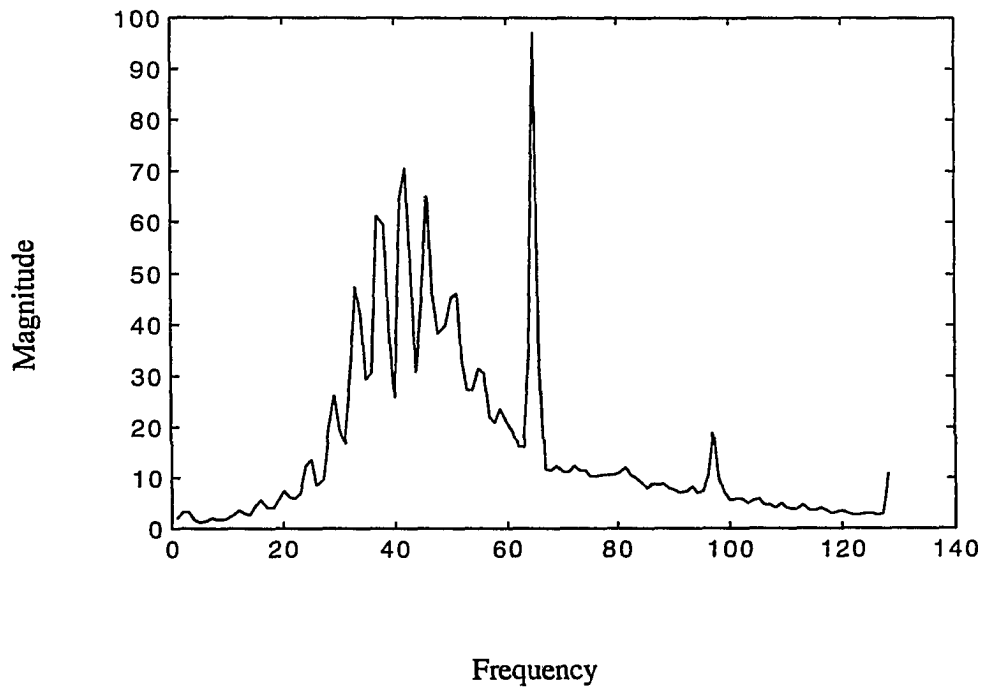


Figure 2.12. Spectrum of the A-scan signal.

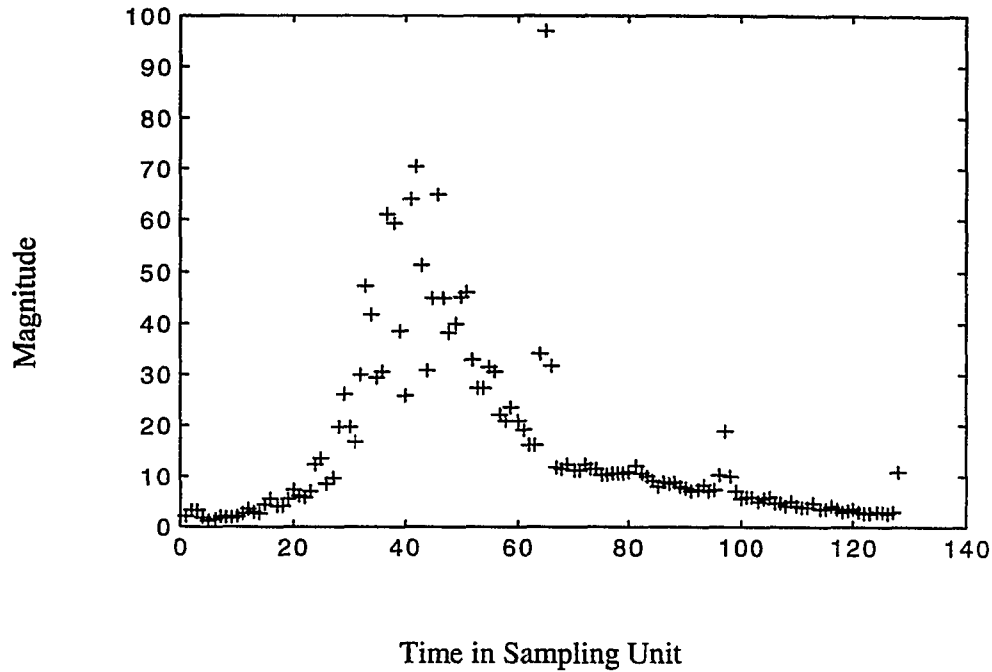


Figure 2.13. Sampled version of the A-scan signal.

We will analyze the effect of uncertainty in estimating the peak value due to sampling.

Let the sampling frequency be four times higher than the center frequency of the signal.

We assume that the ultrasonic signal can be written as $A(t)\cos(\omega t)$. The process of sampling can be explained as discretely picking a value of signal from the signal with random phase relation. Because we chose sampling frequency as 4 times higher than the center frequency ω_c , the maximum value sampled can be expressed as (2.25).

$$A(t)\cos(\omega t + \theta), \quad \pi/4 < \theta < 3\pi/4 \quad (2.25)$$

if $A(t)$ is bandlimited and its maximum frequency component is much smaller than $\frac{\omega_c}{2\pi}$.

Considering that the real peak value is $A(t)$, we can express the error $e(t)$ between the true value and its quantized value as (2.26)

$$e(t) = A(t) \{ 1 - \cos(\theta) \}, \quad \pi/4 < \theta < 3\pi/4 \quad (2.26)$$

The mean squared error (MSE) is given by:

$$\text{MSE} = 2 \frac{A^2(t)}{\pi} \int_{\pi/4}^{3\pi/4} (1 - \cos\theta)^2 d\theta \quad (2.27)$$

This corresponds to a mean square error that is approximately 30 % of the peak value.

This is the perhaps the biggest source of noise in the ultrasonic imaging system. One possible solution is to use a higher sampling rate, but this is costly and often difficult to implement. Since the error is introduced in estimate of the signal amplitude, we can model the associated degradation process as follows.

$$U'(m,n) = U(m,n) \{ 1 + N_1(m,n) \} + N_2(m,n) \quad (2.28)$$

Here $U(m,n)$: original image

$U'(m,n)$: acquired image

$N_1(m,n)$: peak detection error

$N_2(m,n)$: additive noise

In general the ultrasonic sample image can be described based on this model. The effect of A/D converter (quantization noise) is much smaller than the above noise particularly when the number of quantization bits used is large.

Median filters are often used for eliminating spot noise encountered in ultrasonic images. However, since median filtering is not a linear process, it is not easy to characterize the reduction in noise using analytical techniques.

2.8 Conventional Envelope Detection of Ultrasonic A-scan Signals

One of the solutions to reduce the peak detection error is to use an envelope detection circuit and sample the envelope signal instead of the RF (radio frequency) signal. This approach can minimize the effect of the peak detection error. This is due to the fact that the bandwidth of the envelope is significantly smaller than the bandwidth of the RF signal. As an example if the center frequency of the envelope signal is five times lower than the RF-signal frequency, the use of the envelope detection circuit is equivalent to increasing the effective sampling frequency by a factor of five.

The envelope detection circuit is simple to implement. However in order to ensure proper operation, the RF signal should have much a higher center frequency relative to envelope signal frequency. If the maximum frequency component of the envelope is less than 1/10 of the carrier frequency, the envelope detection approach can lead to error [78]. In the case of ultrasonic signals this condition is not always met, and in many cases the RF

signal center frequency is just a few times higher than the highest envelope frequency component.

To avoid errors, the time constant of the detection circuit cannot be too small since this can contribute to ripple in the signal. The ripple introduces error in the peak value estimates.

2.9 Improved Envelope Detection of Ultrasonic A-scan Signal

Let the A-scan signal be expressed as

$$x(t) = A(t)\cos(\omega t + \theta) \quad (2.29)$$

where $A(t)$ represents the envelope of the signal. If we square the received signal, then

$$\begin{aligned} f(t) &= x^2(t) \\ &= A^2(t)\cos^2(\omega t + \theta) \\ &= A^2(t)\left\{\frac{1 + \cos(2\omega t + 2\theta)}{2}\right\} \end{aligned} \quad (2.30)$$

Since the envelope is typically a low frequency signal, low pass filtering eliminates the carrier component. The square root of the filtered signal is given by.

$$y(t) = \sqrt{\frac{A^2(t)}{2}} = \frac{1}{\sqrt{2}} A(t) \quad (2.31)$$

This envelope detector is superior to the method based on rectification and filtering, although the circuit is more complicated and requires the use of a high quality low pass filter to separate the RF signal and envelope signal components.

2.10 Interpolation of Ultrasonic A-scan Signals

This section describes an alternative approach to reducing the peak detection error. When the envelope frequency is as high as half the center frequency, the envelope detection approach does not offer satisfactory performance. An alternate approach is to use interpolation techniques to increase the sampling rate. Using such interpolation techniques, the peak value can be estimated with a greater degree of accuracy.

The process of digitally converting the sampling rate of a signal from a given rate $f = 1/T$ to a different rate $f' = 1/T'$ is called sampling rate conversion [108]. When the new sampling rate is higher than the original sampling rate, that is,

$$f' > f \tag{2.32}$$

or

$$T' < T \tag{2.33}$$

the process is generally called interpolation since we are creating samples of the original physical process from a reduced set of samples.

If the sampling rate is increased by an integer factor L , then the new sampling period, T' , is

$$T' / T = 1/L \quad (2.34)$$

and the new sampling rate f' is

$$f' = Lf \quad (2.35)$$

This process of increasing the sampling rate (interpolation) of a signal $x(n)$ by L implies that we must interpolate $L - 1$ new sample values between each pair of sample values of $x(n)$. The process is similar to that of digital-to-analog conversion in which all continuous-time values of a signal $x_c(t)$ must be interpolated from its sequence $x(n)$.

The input signal $x(n)$ is “filled in” with $L - 1$ zero-valued samples between each pair of samples of $x(n)$, giving the signal

$$w(m) = \begin{cases} x\left(\frac{m}{L}\right), & m = 0, \pm L, \pm 2L, \dots \\ 0, & \text{otherwise} \end{cases} \quad (2.36)$$

The sampling rate expander is depicted with a block diagram symbol of an up-arrow with an integer corresponding to the increase in the sampling rate as given by equation (2.36). The Z-transform of the resulting signal $w(n)$ is

$$\begin{aligned} W(z) &= \sum_{m=-\infty}^{\infty} w(m)z^{-m} \\ &= \sum_{m=-\infty}^{\infty} x\left(\frac{m}{L}\right)z^{-m} \\ &= X(z^L) \end{aligned} \quad (2.37)$$

Evaluating $W(z)$ on the unit circle, $z = e^{j\omega}$, gives the result

$$W(e^{j\omega}) = X(e^{j\omega L}) \quad (2.38)$$

which is the Fourier transform of the signal $w(m)$ expressed in terms of the spectrum of the input signal $x(n)$. Figure 2.14 shows the block diagram of the interpolator.

The spectrum of $w(m)$ contains not only the baseband frequencies of interest (i.e., $-\pi/L$ to π/L) but also images of the baseband signal centered at harmonics of the original sampling frequency $\pm 2\pi/L, \pm 4\pi/L, \dots$. To recover the baseband signal of interest and eliminate the unwanted image components, it is necessary to filter the signal $w(m)$ with a digital lowpass filter which approximates the ideal characteristic

$$H(e^{j\omega'}) = \begin{cases} G, & |\omega'| \leq \frac{2\pi FT'}{2} = \frac{\pi}{L} \\ 0, & \text{otherwise} \end{cases} \quad (2.39)$$

It will be shown that in order to ensure that the amplitude of $y(m)$ is correct, the gain of the filter, G , must be L in the passband.

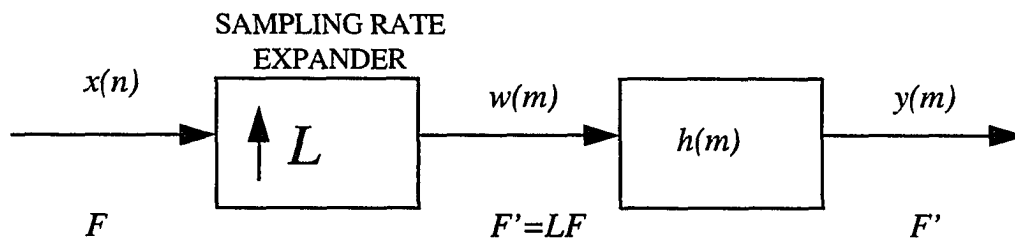


Figure 2.14. Block diagram of an interpolator that increases the sampling rate by L .

Letting $H(e^{j\omega'})$ denote the frequency response of an actual filter that approximates the characteristic in (2.39). It is seen that

$$Y(e^{j\omega'}) = H(e^{j\omega'})X(e^{j\omega'L}) \quad (2.40)$$

and using (2.39),

$$Y(e^{j\omega'}) = \begin{cases} GX(e^{j\omega'L}), & |\omega'| \leq \frac{\pi}{L} \\ 0, & \text{otherwise} \end{cases} \quad (2.41)$$

It is easy to see why we need a gain of G in $H(e^{j\omega'})$.

This approach represents an excellent method to reduce the peak detection error. However the procedure is also computationally intensive.

2.11 Degradation in Eddy Current Images

The biggest source of degradation associated with eddy current imaging methods is contributed by the finite size of the eddy current probe. We can approximate the image degradation process using the block diagram shown in Figure 2.15.

$$u'(\mu, \nu) = u(\mu, \nu) * h(\mu, \nu) + n(\mu, \nu) \quad (2.42)$$

Here, $h(\mu, \nu)$ accounts for the blurring caused by the eddy current probe geometry and $n(\mu, \nu)$ represents additive noise introduced due to quantization and circuit noise.

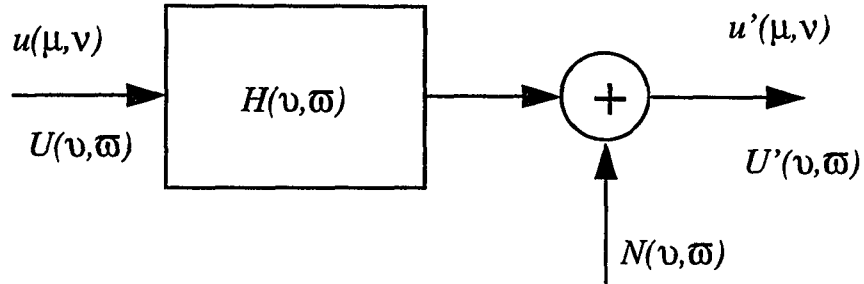


Figure 2.15. Model of the eddy current imaging scheme.

In the frequency domain

$$U'(\nu, \omega) = U(\nu, \omega)H(\nu, \omega) + N(\nu, \omega) \quad (2.43)$$

Classical methods of restoring the signal include the use of Wiener and Kalman filtering techniques. The method require an accurate estimate of the degradation kernel. The kernel $H(\nu, \omega)$ associated with degradation process is usually found using experimental data or by using numerical models representing the test set-up. A major problem with the use of Wiener filtering techniques is that a small amount of error in the estimate of the kernel $H(\nu, \omega)$ can result in large errors and ringing in the restored image.

CHAPTER III

IMAGE FUSION USING NEURAL NETWORKS

This dissertation describes three basic approaches to data fusion. The first of the approaches relies on the use of learning algorithms to identify the association rule for fusing the images. The other two techniques described in the following chapters rely on methods that minimize an appropriate functional or operate in transform domain that allow easy manipulation of image statistics. This chapter focuses its attention on techniques that use neural networks for fusing the data at the pixel level.

3.1 Pixel-level Fusion

The simplest technique for fusing multiple images is to perform logical operations on the images at the pixel level. As an example, the AND (maximum) operator allows features that are shared by the images to be emphasized. In contrast the OR (minimum) operation allows the synthesis of complementary information from the images. These heuristic approaches can be used for simple problems. Figure 3.1 shows an example of this approach. The concept can be extended further where the fusion rules are arrived at through learning approaches. The following section describes techniques for fusing images at the pixel level using trainable networks. These approaches offer a major advantage, in that the rules for fusing the pixels do not have to be specified a priori.

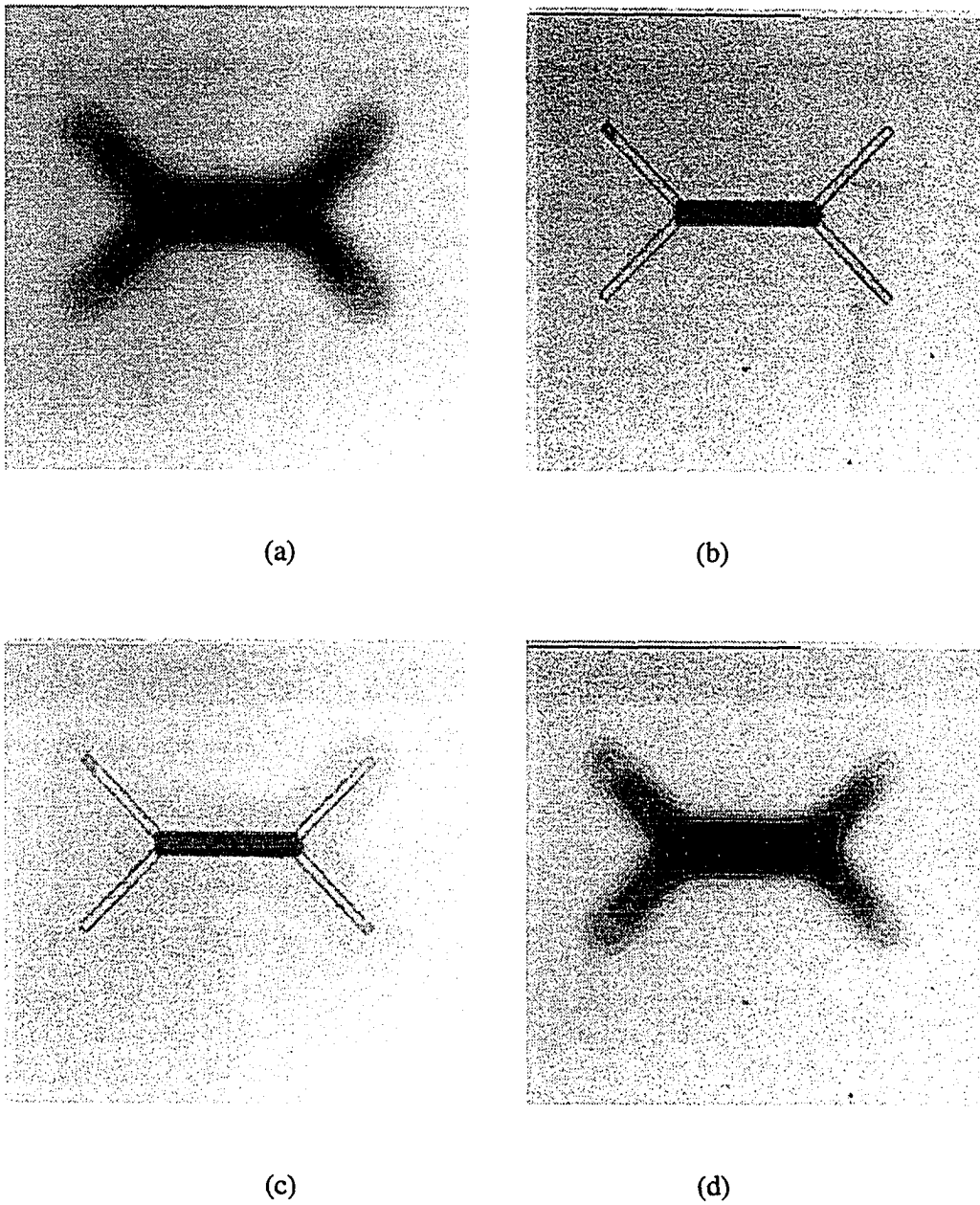


Figure 3.1. MAX and MIN image in the pixel domain. a) Eddy current image; b) Ultrasonic image; c) Image obtained by selecting the maximum valued pixels; d) Image obtained by selecting the minimum valued pixels; e) Differentiated image; f) Averaged image.

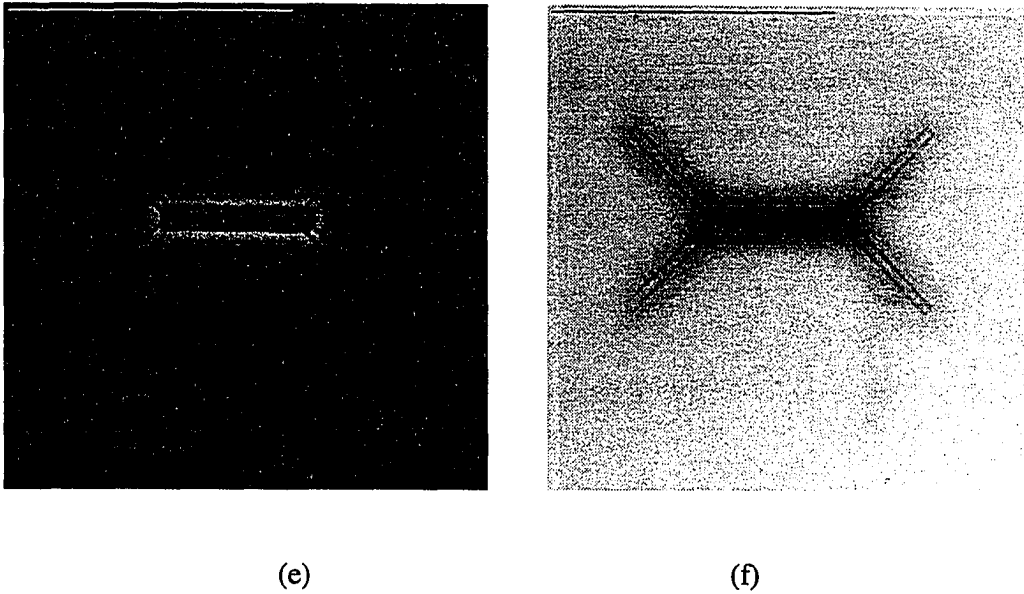


Figure 3.1. (Continued).

3.2 Image Fusion Using Neural Networks

This section presents some new neural network based approaches for combining information obtained using multiple inspection methodologies at the pixel level to obtain more comprehensive information about the condition of the test specimen. Two specific application examples, one involving an attempt to fuse eddy current and ultrasonic images, and the other to fuse multifrequency eddy current images are described. Networks that were evaluated for implementing the fusion algorithm include multi-layer perceptrons (MLP) as well as radial basis function (RBF) networks.

3.2.1 Image Fusion Using Multi-Layer Perceptron Networks

The first technique involves the use of multilayer perceptron networks [60] for fusing the images. The use of such networks have been proposed for the analysis of eddy current and ultrasonic NDE signals [17]. MLP networks consist of a set of simple nonlinear processing elements that are arranged in layers and connected via weights. The network is usually trained using an appropriate algorithm (such as the well known back-propagation algorithm) and a set of exemplars to estimate the interconnection weights.

We implement the data fusion algorithm using a perceptron with a single hidden layer as shown in Figure 3.2. Since a single output image is synthesized from two input images, we have two input nodes and one output node. The network is trained using pixel values in the defect and defect-free regions.

3.2.2 Image Fusion Using Radial Basis Function Networks

The Radial Basis Function network employs two layers. The output nodal values are a linear combination of the basis functions that are calculated by the hidden layer nodes. A variety of basis functions can be employed. The most common basis function that is employed is a Gaussian function.

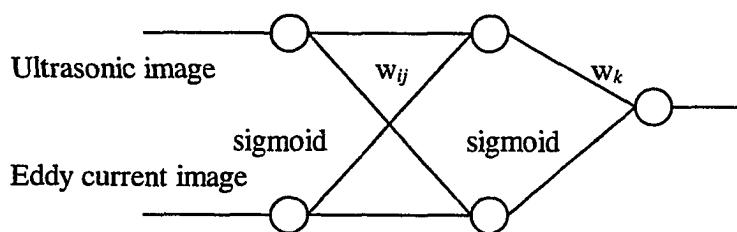


Figure 3.2. Multilayer perceptron network used for fusing images.

In this case, the output nodal value $f(k)$ is given by:

$$f(k) = \sum_{j=1}^M \lambda(j,k) \phi(\|x - y_j\|) \quad (3.1)$$

where $f(k)$ = value at the k^{th} output node.

x = input data vector.

y_j = center vector for j^{th} hidden layer node.

$\phi(x)$ = Gaussian basis function, $\exp(-2x^2)$.

$\lambda(j,k)$ = weight between j^{th} hidden layer node and k^{th} output node.

M = number of hidden layer nodes or centers.

As a single output image is synthesized from two input images, we have two input nodes and one output node, as indicated in Figure 3.3. The number of hidden layer nodes correspond to the number of center vectors that are used. Therefore, for this problem, we need to determine the center vectors and select the desired output values for these center vectors.

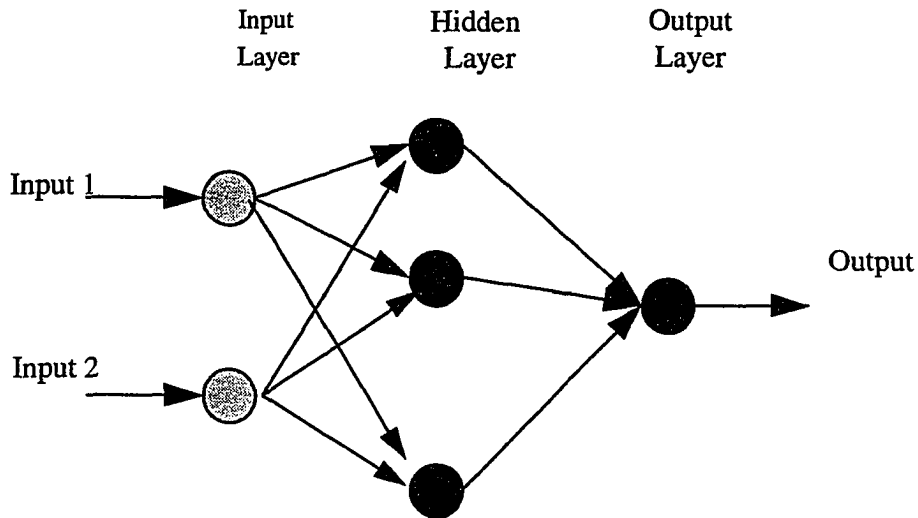


Figure 3.3. Radial basis function network.

In order to train the RBF network for fusing the ultrasonic and eddy current images, we use the following procedure:

- 1) Obtain the center vectors by selecting several regions within the input images and calculate the mean vectors of these regions.
- 2) Obtain the training inputs by using a pair of pixel values from each of the ultrasonic and eddy current images.
- 3) Select the desired output value for the each of the center vectors.

An alternative approach to using the above manual procedure is to use a clustering algorithm, such as the K-means algorithm, to cluster the data and determine the center vectors. The need to determine the output value that should be associated with the given input vector represents a major problem with this approach. This implies that we need to establish a general relation between the eddy current signal and the corresponding ultrasonic

signal value. Although both approaches have been attempted, the results reported here are based on the manual selection of center vectors.

From the given data, we need to estimate the weight values between the hidden layer nodes and the output node. Rewriting equation (3.1) [61], we have:

$$f_i = \sum_{j=1}^M \lambda(j) \phi(\|x_i - y_j\|) \quad (3.2)$$

$$A_{ij} \equiv \phi(\|x_i - y_j\|) \quad (3.3)$$

$$f_i = \sum_{j=1}^M \lambda(j) A_{ij} \quad (3.4)$$

where $i = 1, 2, \dots, N$

j hidden layer node number

N number of training samples

Using matrix notation:

$$\mathbf{A} = \begin{bmatrix} A_{11} & A_{12} & \dots & A_{1N} \\ A_{21} & A_{22} & \dots & A_{2N} \\ \vdots & \vdots & \ddots & \vdots \\ A_{M1} & A_{M2} & \dots & A_{MN} \end{bmatrix} \quad (3.5)$$

$$\mathbf{f} = \begin{bmatrix} f_1 \\ f_2 \\ \vdots \\ f_M \end{bmatrix} \quad (3.6)$$

$$\boldsymbol{\lambda} = \begin{bmatrix} \lambda_1 \\ \lambda_2 \\ \vdots \\ \lambda_N \end{bmatrix} \quad (3.7)$$

$$\mathbf{f} = \mathbf{A}\boldsymbol{\lambda} \quad (3.8)$$

Matrix \mathbf{A} can easily be calculated since the center vectors and the basis function are known. To determine the value $\boldsymbol{\lambda}$ for a given \mathbf{A} , and the desired output value \mathbf{f} , we need to solve (3.8). If the \mathbf{A} matrix is square and non-singular, equation (3.8) can be solved.

$$\boldsymbol{\lambda} = \mathbf{A}^{-1}\mathbf{f} \quad (3.9)$$

In this case, however, the number of input samples is greater than the number of center vectors, resulting in an over-determined system. Under these conditions, a least square estimate can be obtained from:

$$\boldsymbol{\lambda} = \mathbf{A}^+\mathbf{f} \quad (3.10)$$

$$(\mathbf{A}^T \cdot \mathbf{A}) \cdot \boldsymbol{\lambda} = \mathbf{A}^T \cdot \mathbf{f} \quad (3.11)$$

We use the Singular Value Decomposition (SVD) to obtain the least-square estimate of λ [63].

3.3 Experimental Results

In order to validate the approach, experimental data were obtained using two test specimens. The first specimen was obtained by drilling a 1/32" diameter hole in a 6 mm thick aluminum test specimen. The top surface was then partially covered by an adhesive backed 0.005" copper foil as shown in Figure 3.4. An ultrasonic c-scan image, shown in Figure 3.5 (a), was obtained using a scanning acoustic microscope system with a 60 MHz focused transducer. Figure 3.5 (b) shows the corresponding eddy current image obtained at 8 kHz excitation frequency using a Zetec® E-144-P pancake probe which has inner diameter of 0.11 inch with 0.05 inch ferrite core. The ultrasonic image shows artifacts introduced by surface roughness. Although the eddy current system is sensitive to the presence of the hidden hole, the image suffers from poor resolution due to the large diameter of the probe. The eddy current signal is relatively unaffected by the poor surface condition.

The eddy current and ultrasonic images were fused using both MLP and RBF networks. Figure 3.6 (a) shows the results obtained using the MLP. The quality of the image is clearly very poor. An analysis of the weight coefficients indicate that the synthesized image shows a far greater influence of the ultrasonic image relative to the eddy current image. Figure 3.6 (b) shows the fused image when an RBF network with two

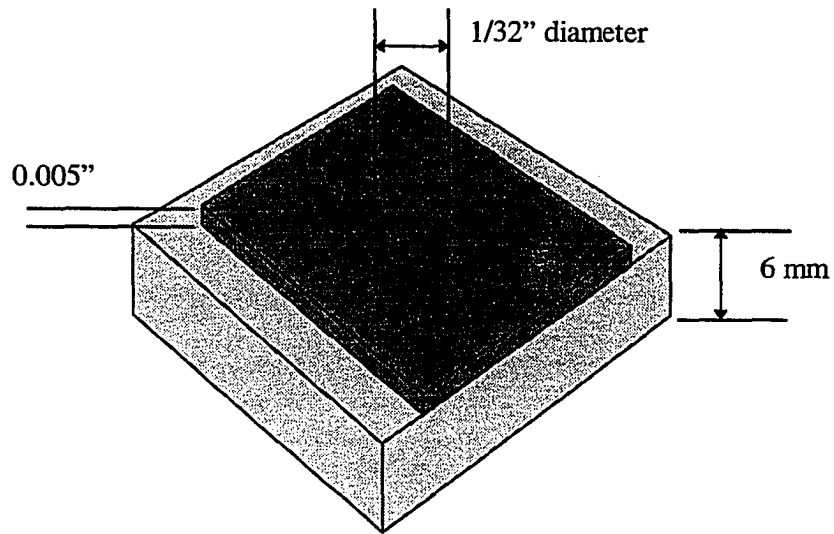


Figure 3.4. Test specimen 1 used to obtain ultrasonic and eddy current images.

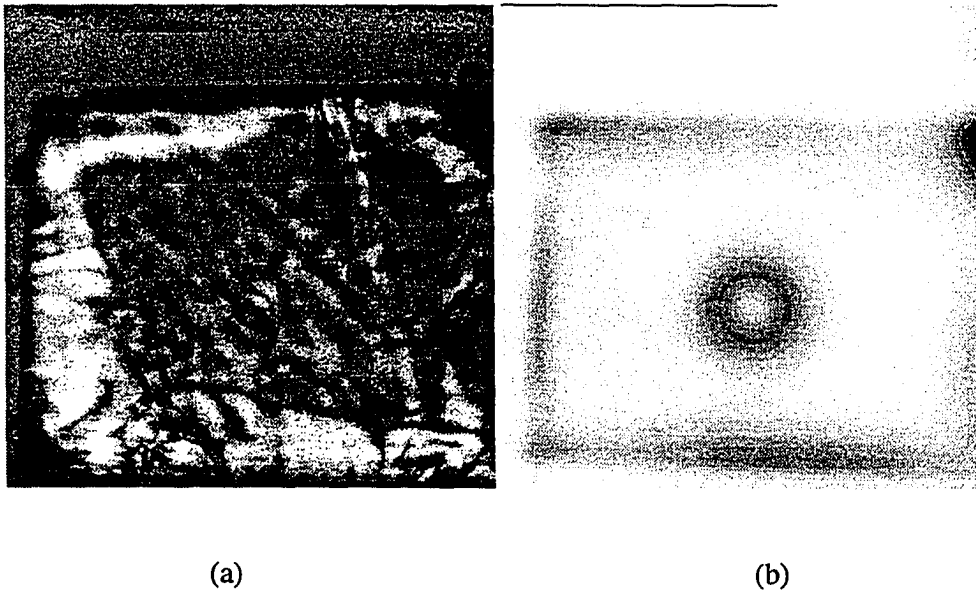


Figure 3.5. Images used for fusion. (a) Raw ultrasonic image data obtained with 60 MHz transducer; (b) Raw eddy current image with 8 kHz excitation.

manually chosen center vectors was used. Figure 3.6 (c) was obtained with a RBF network with five center vectors that were chosen using the K-means algorithm. The resulting images offer a higher SNR at the expense of lower resolution relative to the MLP synthesized image.

The second test specimen consisted of an 6 mm thick aluminum block with a 0.005” diameter 5.5 mm deep flat bottom hole as shown in Figure 3.7. The test specimen was inspected using an eddy current system. Figures 3.8 (a) and 3.8 (b) show eddy current images obtained at excitation frequencies of 6 kHz and 20 kHz respectively. The two eddy current images were fused using a RBF network with 5 hidden layer nodes with centers that were selected using the K-means clustering algorithm. Figure 3.8 (c) shows the resulting fused image. The fused image shows the sub-surface flaw relatively clearly.

The results appear to indicate that the fusion of ultrasonic image eddy current images can increase the reliability of inspection. The multi-layer perceptron based algorithm is sensitive to the choice of exemplars during the training phase, and sometimes generates a result which is biased either towards the ultrasonic or eddy current image. The radial basis function based system fuses the image inputs smoothly reflecting information from both input images. The noise in the ultrasonic image was reduced by the fusion, and output image also offers good resolution.

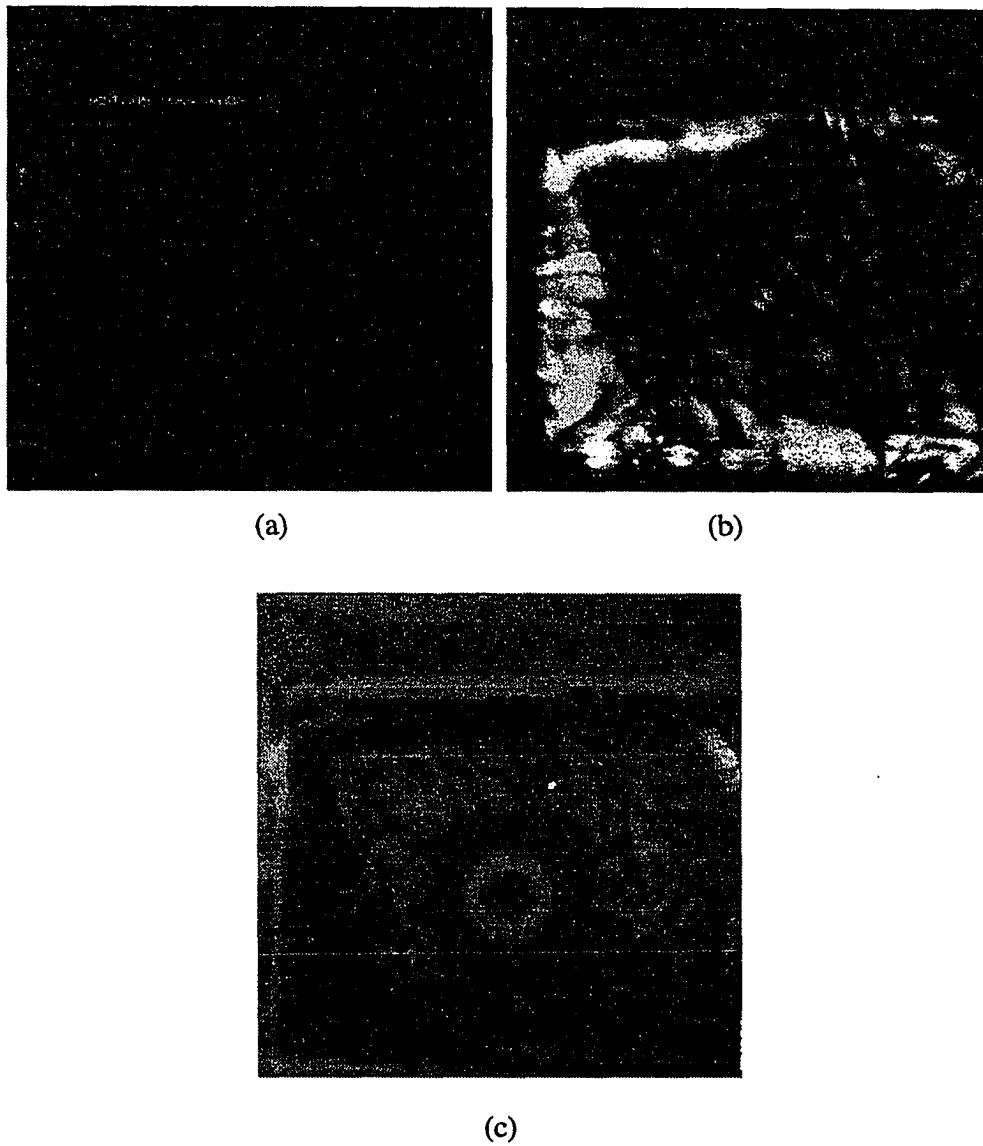


Figure 3.6. Fused images using MLP and RBF network.

- a) Fused image obtained using MLP network with 2 hidden layer nodes;
- b) Fused image obtained using RBF network with 2 hidden layer nodes;
- c) Fused image obtained using RBF network with 5 hidden layer nodes and K-means algorithm for identifying the centers.

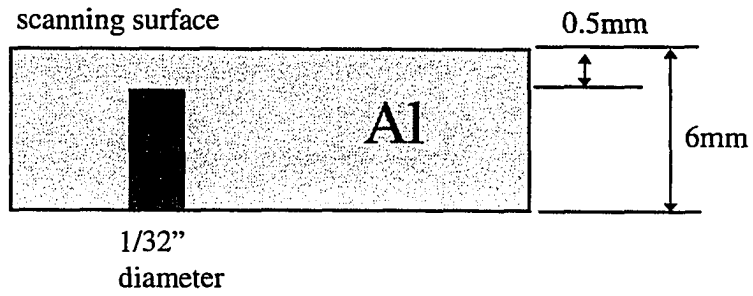


Figure 3.7. Test specimen 2 used for obtaining eddy current images.

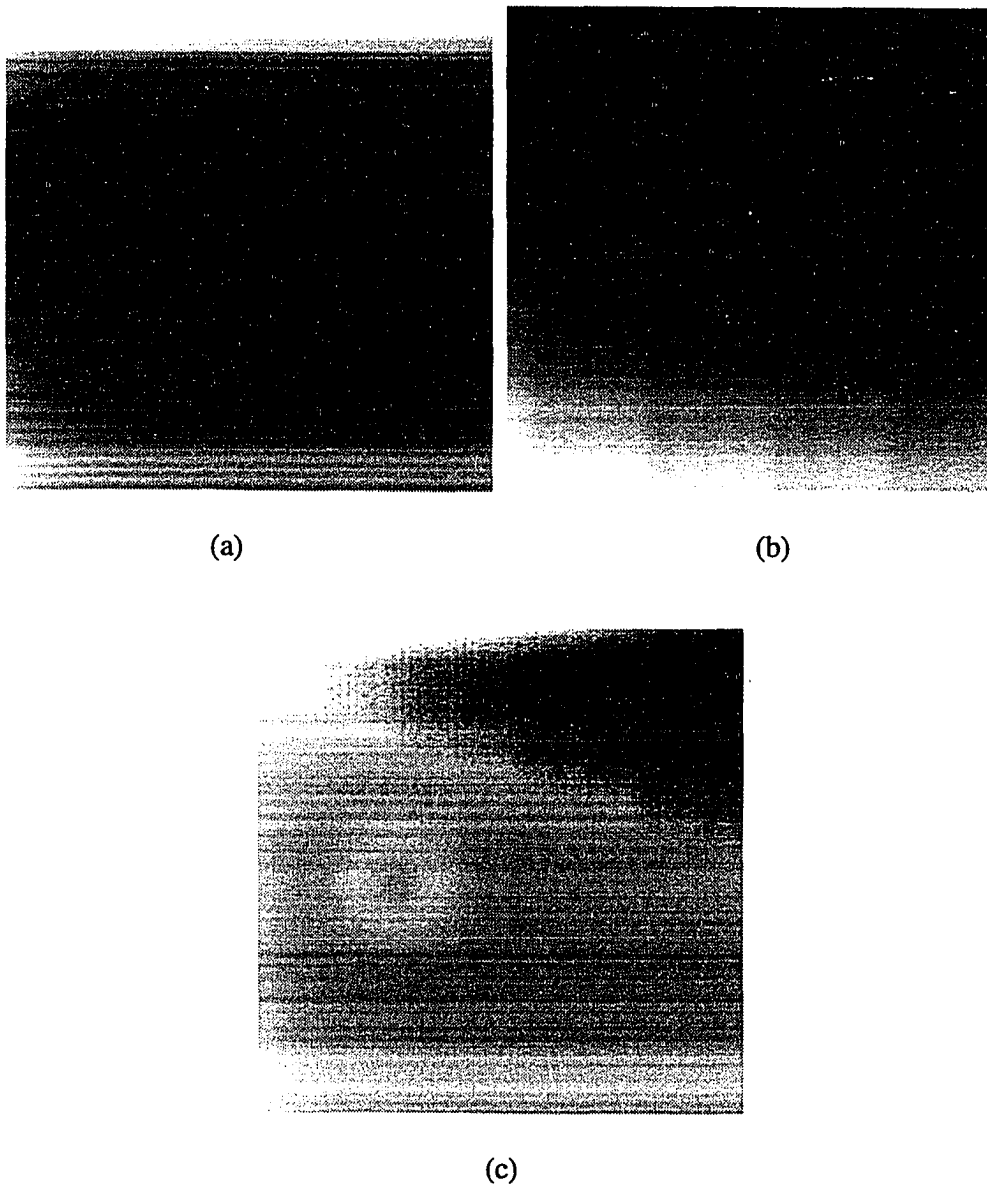


Figure 3.8. Fusion of multifrequency eddy current images using an RBF network.

(a) Low frequency (6 kHz) eddy current image; (b) High frequency (20 kHz) eddy current image; (c) Fused image obtained with RBF network employing K-means algorithm to determine the 5 centers.

CHAPTER IV

MULTIPLE INPUT LINEAR MINIMUM MEAN SQUARE ERROR FILTER

This chapter presents an optimal approach for fusing images derived from a heterogeneous sensor environment. The method uses a linear minimum mean square error (LMMSE) filter to fuse multiple images. We will begin with a discussion on a multiple input LMMSE filter for a one dimensional system and extend it to a two dimensional system later. We may call it a multiple input Wiener filter as well.

4.1 LMMSE Filter for Multiple Input System

We assume that the signals are linearly degraded as shown in Figure 4.1, and both signal and noise are random processes, and that we have knowledge of their spectral characteristics. We also assume that the signals are registered. Under these assumptions we can derive a filter that minimizes the mean-square error (MSE). The linear system used for fusion, consists of N filters whose outputs are summed together to generate the fused signal $\hat{s}(t)$, as shown in Figure 4.1. We call the linear filter which minimizes the mean square error as a multiple input LMMSE filter, and call the conventional LMMSE filter with a single input as a single input LMMSE filter. We also assume in the derivation that the system and signals are real and stationary.

The terminology used in this chapter is summarized below.

$s(t)$: original signal.

$\hat{s}(t)$: restored signal.

$h_j(t)$: transfer function associated with j -th degradation stage, $1 \leq j \leq N$.

$y_j(t)$: degraded signal corresponding to the j -th stage, $1 \leq j \leq N$.

$n_j(t)$: additive noise at the input of the j -th stage restoration filter, $1 \leq j \leq N$.

$x_j(t)$: input to the filter at the j -th stage, $1 \leq j \leq N$.

$g_j(t)$: restoration filter at the j -th stage, $1 \leq j \leq N$.

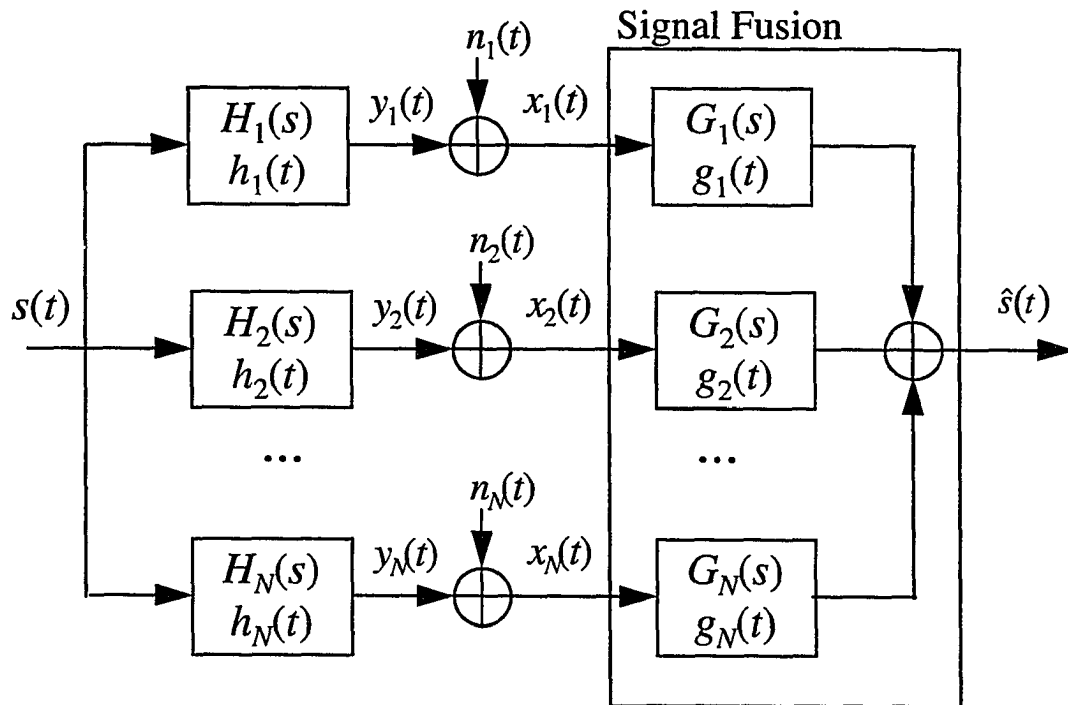


Figure 4.1. Model for linear signal fusion.

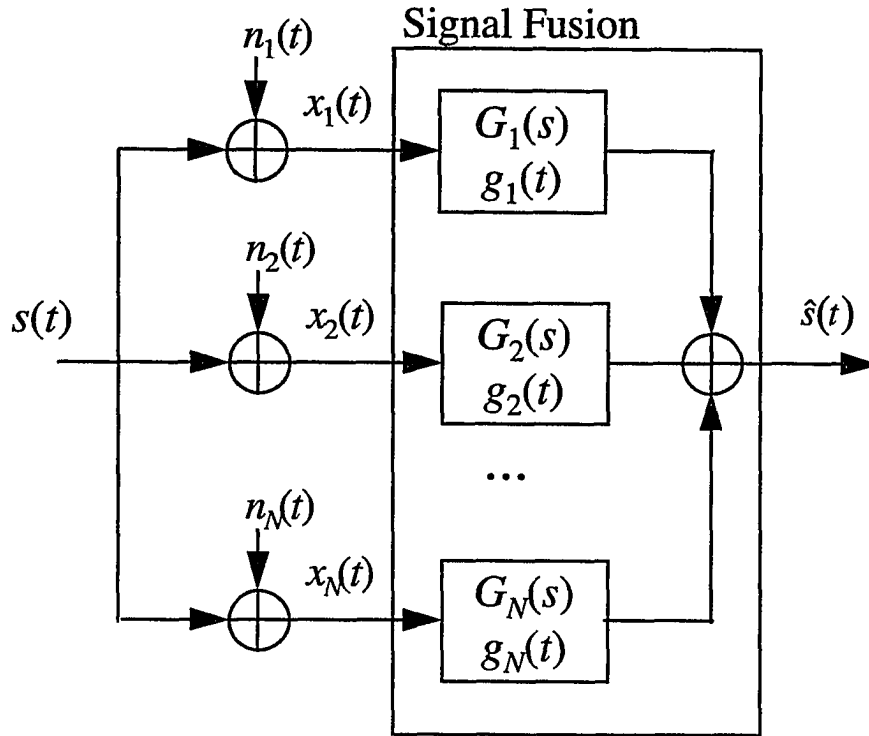


Figure 4.2. Multiple input LMMSE filter without degradation.

4.2 LMMSE Filter for a System with Multiple Inputs with Additive Noise

First, we will consider a N input LMMSE filter for one dimensional signals with additive noise only. Figure 4.2 illustrates the corresponding block diagram. The input $x_j(t)$ for the j -th stage, $1 \leq j \leq N$, is

$$x_j(t) = s(t) + n_j(t). \quad (4.1)$$

The restored signal $\hat{s}(t)$ is given by

$$\begin{aligned}
\hat{s}(t) &= \sum_{i=1}^N g_i(t) * x_i(t) \\
&= \sum_{i=1}^N \int_{-\infty}^{\infty} g_i(t-\lambda) x_i(\lambda) d\lambda
\end{aligned} \tag{4.2}$$

We design the filter by minimizing the mean square error (MSE) defined by

$$M.S.E. \equiv \mathcal{E} \left[(s(t) - \hat{s}(t))^2 \right] \tag{4.3}$$

The MSE is minimized if g_j ($1 \leq j \leq N$) satisfies the orthogonality condition [6].

$$\mathcal{E} \left[(s(t) - \hat{s}(t)) x_j(t') \right] = 0, \text{ for } t' \in \mathbf{R} \text{ and } \forall j, 1 \leq j \leq N. \tag{4.4}$$

$$\mathcal{E} \left[\left(s(t) - \sum_{i=1}^N \left\{ \int_{-\infty}^{\infty} g_i(\lambda) x_i(t-\lambda) d\lambda \right\} \right) x_j(t') \right] = 0, \text{ for } t' \in \mathbf{R} \text{ and } \forall j, 1 \leq j \leq N. \tag{4.5}$$

Here we use the correlation function which is defined as follows for a real and stationary signal.

$$R_{x,y}(\tau) = \mathcal{E} [x(t+\tau)y(t)] \tag{4.6}$$

where $\mathcal{E} [\cdot]$ denotes the expectation operator.

$$\sum_{i=1}^N \left\{ \int_{-\infty}^{\infty} \left[g_i(\lambda) R_{x_i, x_j}(t-\lambda-t') \right] d\lambda \right\} = R_{s, x_j}(t-t'), \text{ for } t' \in \mathbf{R} \text{ and } \forall j, 1 \leq j \leq N. \tag{4.7}$$

Let $\tau = t - \xi$

$$\sum_{i=1}^N \left\{ \int_{-\infty}^{\infty} [g_i(\lambda) R_{x_i, x_j}(\tau - \lambda)] d\lambda \right\} = R_{s, x_j}(\tau), \quad \text{for } \forall j, 1 \leq j \leq N. \quad (4.8)$$

If $s(t)$, $n_i(t)$ and $n_j(t)$ are uncorrelated, then

$$\begin{aligned} R_{x_i, x_j}(t) &= R_{s+n_i, s+n_j}(t) = R_s(t) + R_{n_i, n_j}(t) \\ R_{s, x_j}(t) &= R_{s, s+n_j}(t) = R_s(t) \end{aligned} \quad (4.9)$$

Substituting (4.9) into (4.8), we get

$$\sum_{i=1}^N \int_{-\infty}^{\infty} [g_i(\lambda) \{R_s(\tau - \lambda) + R_{n_i, n_j}(\tau - \lambda)\}] d\lambda = R_s(\tau), \quad \text{for } \forall j, 1 \leq j \leq N. \quad (4.10)$$

Then, taking the 2-sided Laplace transform, we have

$$\left[\sum_{i=1}^N G_i(s) S_s(s) \right] + G_j(s) S_{n_j}(s) = S_s(s), \quad \text{for } \forall j, 1 \leq j \leq N. \quad (4.11)$$

If $\sum_{i=1}^N G_i(s) = \Gamma$, then by rearranging (4.11) we obtain

$$G_j(s) = \frac{S_s(s)}{S_{n_j}(s)} (1 - \Gamma), \quad \text{for } \forall j, 1 \leq j \leq N. \quad (4.12)$$

Summing (4.12) over all channels, we get

$$\Gamma = \sum_{i=1}^N G_i(s) = \sum_{i=1}^N \left\{ \frac{S_s(s)}{S_{n_i}(s)} (1 - \Gamma) \right\} \quad (4.13)$$

Solving for Γ , we obtain

$$\Gamma = \frac{S_s(s) \sum_{i=1}^N \frac{1}{S_{n_i}(s)}}{1 + S_s(s) \sum_{i=1}^N \frac{1}{S_{n_i}(s)}} \quad (4.14)$$

or

$$\Gamma = 1 - \frac{1}{1 + S_s(s) \sum_{i=1}^N \frac{1}{S_{n_i}(s)}} \quad (4.15)$$

Substituting Γ into the equation for $G_j(s)$, (4.12), we have,

$$G_j(s) = \frac{S_s(s)}{S_{n_j}} \frac{1}{1 + S_s(s) \sum_{i=1}^N \frac{1}{S_{n_i}(s)}}, \quad \text{for } \forall j \ 1 \leq j \leq N. \quad (4.16)$$

We also observe from the N input LMMSE filter equation, that for the special case where $N = 1$, (4.16) reduces to the traditional single input LMMSE filter. Looking again at equation (4.11), we can establish the following relationship between the different restoration filters $G_j(s)$.

$$G_i(s)S_{n_i}(s) = G_j(s)S_{n_j}(s), \quad \text{for } \forall i \text{ and } \forall j \ 1 \leq i, j \leq N. \quad (4.17)$$

For the special case where $N = 2$, the two input LMMSE filter can be rearranged in the following format.

$$\begin{aligned}
G_1(s) &= \frac{1}{1 + \frac{S_{n_1}(s)}{S_s(s)} + \frac{S_{n_1}(s)}{S_{n_2}(s)}} \\
G_2(s) &= \frac{1}{1 + \frac{S_{n_2}(s)}{S_s(s)} + \frac{S_{n_2}(s)}{S_{n_1}(s)}}
\end{aligned} \tag{4.18}$$

4.3 LMMSE Filter for a System with Multiple Degenerated Inputs with Additive Noise

In this section, we will expand the previous result to a situation where the degradation process is as shown in Figure 4.1. The original signal $s(t)$ undergoes N different degradation processes, $h_j(t)$, to generate $y_j(t)$, $1 \leq j \leq N$.

$$y_j(t) = h_j(t) * s(t) \quad \text{for } 1 \leq j \leq N.$$

The inputs to the each restoration filter are given by

$$x_j(t) = y_j(t) + n_j(t) = h_j(t) * s(t) + n_j(t) \quad \text{for } 1 \leq j \leq N. \tag{4.19}$$

The restored signal $\hat{s}(t)$ is

$$\begin{aligned}
\hat{s}(t) &= \sum_{i=1}^N g_i(t) * x_i(t) \\
&= \sum_{i=1}^N \int_{-\infty}^{\infty} g_i(t - \lambda) x_i(\lambda) d\lambda
\end{aligned} \tag{4.20}$$

The MSE as defined by (4.3) is minimized if g_j ($1 \leq j \leq N$) satisfies the orthogonality condition (4.4).

$$\mathcal{E} \left[\left(s(t) - \sum_{i=1}^N \left\{ \int_{-\infty}^{\infty} g_i(\lambda) x_i(t-\lambda) d\lambda \right\} \right) x_j(t') \right] = 0, \text{ for } t' \in \mathbf{R} \text{ and } \forall j, 1 \leq j \leq N. \quad (4.21)$$

Using the same procedure as (4.6), (4.7), we have

$$\sum_{i=1}^N \left\{ \int_{-\infty}^{\infty} [g_i(\lambda) R_{x_i, x_j}(\tau - \lambda)] d\lambda \right\} = R_{s, x_j}(\tau), \text{ for } \forall j, 1 \leq j \leq N. \quad (4.22)$$

If $s(t)$, $n_i(t)$ ($1 \leq i \leq N$) are uncorrelated, then

$$\begin{aligned} R_{x_i, x_j}(t) &= R_{y_i + n_i, y_j + n_j}(t) = R_{y_i, y_j}(t) + R_{n_i, n_j}(t) \\ R_{s, x_j}(t) &= R_{s, y_j + n_j}(t) = R_{s, y_j}(t) \end{aligned} \quad (4.23)$$

Substituting (4.23) into (4.22), we have

$$\sum_{i=1}^N \int_{-\infty}^{\infty} [g_i(\lambda) \{ R_{y_i, y_j}(\tau - \lambda) + R_{n_i, n_j}(\tau - \lambda) \}] d\lambda = R_{s, y_j}(\tau), \text{ for } \forall j, 1 \leq j \leq N. \quad (4.24)$$

We will derive the expression for the cross correlation of the real signal which will be used in (4.24). Using the relation shown in Figure 4.3,

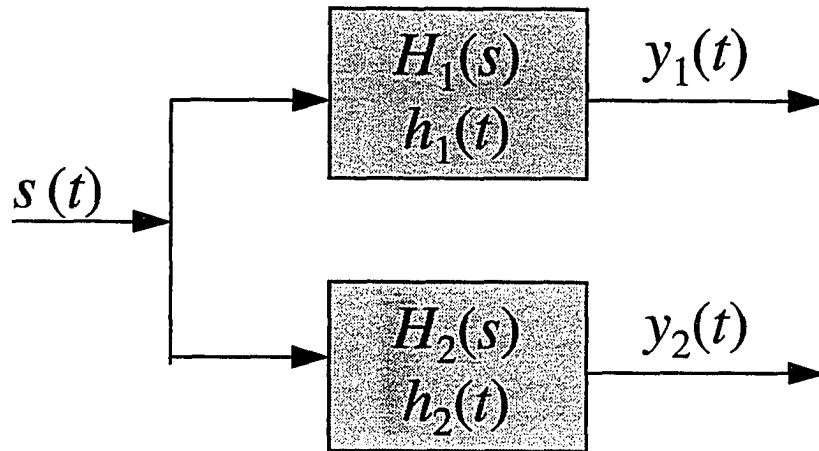


Figure 4.3. Model for computing the cross-correlation for multiple terminal outputs.

$$\begin{aligned}
 y_1(t) &= \int_{-\infty}^{\infty} s(t-\lambda)h_1(\lambda)d\lambda \\
 y_2(t) &= \int_{-\infty}^{\infty} s(t-\lambda)h_2(\lambda)d\lambda
 \end{aligned}
 \tag{4.25}$$

Multiplying the first equation by $y_2(t-\tau)$ and the second equation by $s(t+\tau)$ and using the result obtained for the multiple input system [76], we have.

$$\begin{aligned}
 y_1(t)y_2(t-\tau) &= \int_{-\infty}^{\infty} s(t-\lambda)y_2(t-\tau)h_1(\lambda)d\lambda \\
 s(t+\tau)y_2(t) &= \int_{-\infty}^{\infty} s(t+\tau)s(t-\lambda)h_2(\lambda)d\lambda
 \end{aligned}
 \tag{4.26}$$

If we compute the expected value of both sides, we have the two equations

$$\begin{aligned}
R_{y_1, y_2}(\tau) &= \int_{-\infty}^{\infty} R_{s, y_2}(\tau - \lambda) h_1(\lambda) d\lambda \\
&= R_{s, y_2}(\tau) * h_1(\tau) \\
R_{s, y_2}(\tau) &= \int_{-\infty}^{\infty} R_s(\tau + \lambda) h_2(\lambda) d\lambda \\
&= R_s(\tau) * h_2(-\tau)
\end{aligned} \tag{4.27}$$

The Laplace transform of (4.27) is given by

$$\begin{aligned}
S_{y_1, y_2}(s) &= S_{s, y_2}(s) H_1(s) \\
S_{s, y_2}(s) &= S_s(s) H_2(-s)
\end{aligned} \tag{4.28}$$

Therefore, the expression for the cross correlation becomes

$$S_{y_1, y_2}(s) = S_s(s) H_1(s) H_2(-s) \tag{4.29}$$

Using this expression for the cross correlation and taking the 2-sided Laplace transform of both sides of (4.24), we obtain

$$\left[\sum_{i=1}^N G_i(s) S_{y_i, y_j}(s) \right] + G_j(s) S_{n_j}(s) = S_{s, y_j}(s), \quad \text{for } \forall j, 1 \leq j \leq N \tag{4.30}$$

$$\left[\sum_{i=1}^N G_i(s) H_i(s) H_j(-s) S_s(s) \right] + G_j(s) S_{n_j}(s) = H_j(-s) S_s(s), \quad \text{for } \forall j, 1 \leq j \leq N. \tag{4.31}$$

$$\left[\sum_{i=1}^N G_i(s)H_i(s)H_j(-s) \right] + G_j(s) \frac{S_{n_j}(s)}{S_s(s)} = H_j(-s), \quad \text{for } \forall j, 1 \leq j \leq N \quad (4.32)$$

We now have an expression for the j -th restoration filter $G_j(s)$.

$$G_j(s) \frac{S_{n_j}(s)}{S_s(s)} = H_j(-s) - H_j(-s) \left(\sum_{i=1}^N G_i(s)H_i(s) \right), \quad \text{for } \forall j, 1 \leq j \leq N \quad (4.33)$$

Let $\Gamma(s) = \sum_{i=1}^N G_i(s)H_i(s)$, Rewriting equation (4.33), we obtain

$$G_i(s) = \frac{S_s(s)H_i(-s)}{S_{n_i}(s)} (1 - \Gamma(s)) \quad \text{for } 1 \leq j \leq N. \quad (4.34)$$

Multiplying both sides by $H_i(s)$ and summing (4.34), we get

$$\begin{aligned} \Gamma(s) &= \sum_{i=1}^N G_i(s)H_i(s) \\ &= (1 - \Gamma(s)) \sum_{i=1}^N \frac{S_s(s)}{S_{n_i}(s)} |H_i(s)|^2 \end{aligned} \quad (4.35)$$

We can solve (4.35) to obtain $\Gamma(s)$.

$$\Gamma(s) = 1 - \frac{1}{1 + \sum_{i=1}^N \frac{S_s(s)}{S_{n_i}(s)} |H_i(s)|^2} \quad (4.36)$$

Substituting $\Gamma(s)$ in the equation for $G_j(s)$, (4.34), we have

$$G_j(s) = \frac{S_s(s)}{S_{n_j}(s)} \frac{H_j(-s)}{1 + \sum_{i=1}^N \frac{S_s(s)}{S_{n_i}(s)} |H_i(s)|^2} \quad \text{for } 1 \leq j \leq N. \quad (4.37)$$

From (4.32) we can derive the following relationship between the different restoration filters.

$$\frac{G_i(s)S_{n_i}(s)}{H_i(-s)} = \frac{G_j(s)S_{n_j}(s)}{H_j(-s)}, \quad \forall i, j \quad 1 \leq i, j \leq N. \quad (4.38)$$

In the special case where $H_i(s) = 1$, for all i ($1 \leq i \leq N$). (4.38) reduces to (4.15).

If $H_i(s)H_j(-s) = 0$, for $i \neq j$, we can derive the reduced expression from (4.34).

$$G_j(s) = \frac{H_j(-s)}{|H_j(s)|^2 + \frac{S_{n_j}(s)}{S_s(s)}}, \quad \text{for } \forall j, 1 \leq j \leq N \quad (4.39)$$

which degenerates to the case of N independent LMMSE filter.

Using matrix notation for (4.32),

$$\mathbf{H}(\mathbf{s}) = \begin{bmatrix} H_1(s) \\ H_2(s) \\ \vdots \\ H_N(s) \end{bmatrix}, \quad \mathbf{G}(\mathbf{s}) = \begin{bmatrix} G_1(s) \\ G_2(s) \\ \vdots \\ G_N(s) \end{bmatrix}, \quad \mathbf{S}_{\text{NS}}(\mathbf{s}) = \frac{1}{S_s(s)} \begin{bmatrix} S_{n_1}(s) & & & \mathbf{0} \\ & S_{n_2}(s) & & \\ & & \ddots & \\ \mathbf{0} & & & S_{n_N}(s) \end{bmatrix}$$

$$\{\mathbf{H}(\mathbf{s})\mathbf{H}^T(-\mathbf{s}) + \mathbf{S}_{\text{NS}}(\mathbf{s})\}\mathbf{G}(\mathbf{s}) = \mathbf{H}(-\mathbf{s}) \quad (4.40)$$

Where $\mathbf{H}^T(-\mathbf{s})$ is the transpose of $\mathbf{H}(-\mathbf{s})$.

$$\mathbf{G}(s) = (\mathbf{H}(s)\mathbf{H}^T(-s) + \mathbf{S}_{NS}(s))^{-1} \mathbf{H}(-s) \quad (4.41)$$

As a simple example, if $N = 2$, the two input LMMSE filter can be rewritten as

$$\begin{bmatrix} |H_1(s)|^2 S_s(s) + S_{n_1}(s) & S_s(s)H_1(s)H_2(-s) \\ S_s(s)H_1(-s)H_2(s) & |H_2(s)|^2 S_s(s) + S_{n_2}(s) \end{bmatrix} \begin{bmatrix} G_1(s) \\ G_2(s) \end{bmatrix} = \begin{bmatrix} H_1(-s)S_s(s) \\ H_2(-s)S_s(s) \end{bmatrix} \quad (4.42)$$

$$G_1(s) = \frac{H_1(-s)S_{n_2}(s)}{|H_1(s)|^2 S_{n_2}(s) + |H_2(s)|^2 S_{n_1}(s) + \frac{S_{n_1}(s)S_{n_2}(s)}{S_s(s)}} \quad (4.43)$$

$$G_2(s) = \frac{H_2(-s)S_{n_1}(s)}{|H_1(s)|^2 S_{n_2}(s) + |H_2(s)|^2 S_{n_1}(s) + \frac{S_{n_1}(s)S_{n_2}(s)}{S_s(s)}}$$

Again as a special case, if the noise spectra are all identical, i.e., $S_{n_j} = S_n$,

for $\forall j, 1 \leq j \leq N$, the filter simplifies to

$$G_j(s) = \frac{H_j(-s)}{\sum_{i=1}^N |H_i(s)|^2 + \frac{S_n(s)}{S_s(s)}} \quad (4.44)$$

When the noise and signal spectra are not available, which is common in practice, we can approximate $\frac{S_n}{S_s}$ suitably with a constant $K = \frac{S_n}{S_s}$.

$$G_j(s) \cong \frac{H_j(-s)}{\sum_{i=1}^N |H_i(s)|^2 + K} \quad \text{for } 1 \leq j \leq N. \quad (4.45)$$

If the signal is noise free, i.e., $S_{n_j} = 0$, for $\forall j, 1 \leq j \leq N$, the filter reduces to

$$G_j(s) = \frac{H_j(-s)}{\sum_{i=1}^N |H_i(s)|^2} \quad (4.46)$$

Often the transfer function representing the degradation is not available. Under these circumstances it is possible to use the spectra of the acquired signals. We will derive a filter that does not require a transfer function representing the degradation, specifically.

$$S_{x_i}(s) = |H_i(s)|^2 S_s(s) + S_{n_i}(s) \quad (4.47)$$

$$|H_i(s)|^2 = \frac{S_{x_i}(s) - S_{n_i}(s)}{S_s(s)} \quad (4.48)$$

If we assume that the system has a symmetric spectrum $H(s) = H(-s)$ which is common in practice,

$$H_i(s) = H_i(-s) = \sqrt{\frac{S_{x_i}(s) - S_{n_i}(s)}{S_s(s)}} \quad (4.49)$$

In this case, by substituting (4.49) into (4.37), we have

$$G_j(s) = \frac{S_s(s)}{S_{n_j}(s)} \frac{\sqrt{\frac{S_{x_j}(s) - S_{n_j}(s)}{S_s(s)}}}{1 + \sum_{i=1}^N \frac{S_{x_i}(s) - S_{n_i}(s)}{S_{n_i}(s)}} \quad \text{for } 1 \leq j \leq N. \quad (4.50)$$

or

$$G_j(s) = \frac{\sqrt{S_s(s)(S_{x_j}(s) - S_{n_j}(s))}}{(1-N)S_{n_j}(s) + S_{n_j}(s) \sum_{i=1}^N \frac{S_{x_i}(s)}{S_{n_i}(s)}} \quad \text{for } 1 \leq j \leq N. \quad (4.51)$$

Using (4.51), we can design a multiple input LMMSE filter using the spectra of the degraded signals together with the original signal and noise spectra.

When the noise spectra are much smaller than the signal spectrum and are all identical, i.e., $S_{n_j} = S_n$ and $S_{x_j} \gg S_n$, $1 \leq j \leq N$, (4.51) becomes.

$$G_j(s) = \frac{\sqrt{S_s(s)S_{x_j}(s)}}{\sum_{i=1}^N S_{x_i}(s)} \quad \text{for } 1 \leq j \leq N. \quad (4.52)$$

When the spectrum of the original signal is not available, we can use the approximation.

$$G_j(s) = K \frac{\sqrt{S_{x_j}(s)}}{\sum_{i=1}^N S_{x_i}(s)} \quad \text{for } 1 \leq j \leq N. \quad (4.53)$$

4.4 Mean Square Error for a Multiple Input LMMSE Filter with Additive Noise

We will now compare the expressions for the MSE for the multiple input LMMSE filter case and the single input LMMSE filter, and average filter. Using the definition for MSE (4.3) and the expression for $\hat{s}(t)$ given by (4.2) and (4.20).

$$M.S.E. = \mathcal{E} \left[\left\{ s(t) - \sum_{i=1}^N \left\{ \int_{-\infty}^{\infty} g_i(\lambda) x_i(t-\lambda) d\lambda \right\} \right\}^2 \right] \quad (4.54)$$

$$\begin{aligned} M.S.E. = R_s(0) - \mathcal{E} \left[2s(t) \sum_{i=1}^N \left\{ \int_{-\infty}^{\infty} g_i(\lambda) x_i(t-\lambda) d\lambda \right\} \right] \\ + \mathcal{E} \left[\left\{ \sum_{i=1}^N \left\{ \int_{-\infty}^{\infty} g_i(\lambda) x_i(t-\lambda) d\lambda \right\} \right\}^2 \right] \end{aligned} \quad (4.55)$$

If we expand all the quadrature terms.

$$\begin{aligned} M.S.E. = R_s(0) - 2 \sum_{i=1}^N \left\{ \int_{-\infty}^{\infty} g_i(\lambda) R_{s,x_i}(\lambda) d\lambda \right\} \\ + \sum_{j=1}^N \sum_{i=1}^N \int_{v=-\infty}^{\infty} \int_{u=-\infty}^{\infty} g_i(u) g_j(v) R_{x_i, x_j}(u-v) du dv \end{aligned} \quad (4.56)$$

or

$$\begin{aligned} M.S.E. = R_s(0) - 2 \sum_{i=1}^N \left\{ \int_{-\infty}^{\infty} g_i(\lambda) R_{s,x_i}(\lambda) d\lambda \right\} \\ + \sum_{j=1}^N \int_{v=-\infty}^{\infty} g_j(v) \left\{ \sum_{i=1}^N \int_{u=-\infty}^{\infty} g_i(u) R_{x_i, x_j}(u-v) du \right\} dv \end{aligned} \quad (4.57)$$

For a system without degradation, substituting (4.9) into (4.57) we have

$$\begin{aligned}
M.S.E. = & R_s(0) - 2 \sum_{i=1}^N \left\{ \int_{-\infty}^{\infty} g_i(\lambda) R_s(\lambda) d\lambda \right\} \\
& + \sum_{j=1}^N \int_{v=-\infty}^{\infty} g_j(v) \left\{ \sum_{i=1}^N \int_{u=-\infty}^{\infty} g_i(u) R_s(u-v) du \right\} dv + \sum_{j=1}^N \int_{v=-\infty}^{\infty} g_j(v) \left\{ \int_{u=-\infty}^{\infty} g_j(u) R_{n_i, n_j}(u-v) du \right\} dv
\end{aligned} \tag{4.58}$$

In comparison, the mean square error for a single input LMMSE filter is given by [6].

$$M.S.E. = R_s(0) - 2 \int_{-\infty}^{\infty} g(\lambda) R_{s,x}(\lambda) d\lambda + \int_{v=-\infty}^{\infty} g(v) \int_{u=-\infty}^{\infty} g(u) R_x(u-v) dudv \tag{4.59}$$

We will now derive the MSE for the average filter which is commonly used for multiple input systems.

$$\hat{s}(t) = \frac{1}{N} \sum_{i=1}^N x_i(t) \tag{4.60}$$

$$M.S.E. = \mathcal{E} \left[\left\{ s(t) - \frac{1}{N} \sum_{i=1}^N x_i(t) \right\}^2 \right] \tag{4.61}$$

$$M.S.E. = R_s(0) - \frac{2}{N} \sum_{i=1}^N R_{s,x_i}(0) + \frac{1}{N^2} \sum_{i=1}^N \sum_{j=1}^N R_{x_i, x_j}(0) \tag{4.62}$$

4.5 Multiple Input LMMSE Filter for the Two -Dimensional Discrete Case

We can derive a multiple input LMMSE filter for the two dimensional discrete signal case by applying the same reasoning that was used to derive (4.37).

$$G_j(z_1, z_2) = \frac{S_s(z_1, z_2)}{S_{n_j}(z_1, z_2)} \frac{H_j(z^{-1}_1, z^{-1}_2)}{1 + \sum_{i=1}^N \frac{S_s(z_1, z_2)}{S_{n_i}(z_1, z_2)} |H_i(z_1, z_2)|^2} \quad \text{for } 1 \leq j \leq N. \quad (4.63)$$

$G_j(z_1, z_2)$ represents the j -th LMMSE filter in the filter bank for the multiple input image system.

If we assume that the spectra is much smaller than the signal spectrum and are all identical, i.e., $S_{n_j} = S_n$ and $S_{x_j} \gg S_n$, for $1 \leq j \leq N$, then.

$$G_j(z_1, z_2) = \frac{\sqrt{S_s(z_1, z_2) S_{x_j}(z_1, z_2)}}{\sum_{i=1}^N S_{x_i}(z_1, z_2)} \quad \text{for } 1 \leq j \leq N. \quad (4.64)$$

4.6 Experimental Verification

In order to verify the approach, the image shown in Figure 4.4 (a) is used as a reference image. Degraded versions of the image are generated by low and high pass filtering the image and superimposing uniformly distributed noise. The degraded images are shown in Figure 4.4 (b) and (c). Figure 4.4 (d) illustrates the reconstructed image using the two degraded images. To facilitate comparison, the results of applying a single input

LMMSE filter for the two degraded images are shown in Figure 4.5 (a) and (b). It is clear that the results are not satisfactory due to the additive noise components. The average of these two reconstructed images, as shown in Figure 4.5 (c), is also much worse than the result obtained using the two input LMMSE filter shown in Figure 4.4 (d). The use of the cross-correlation parameters of the two images allows the two-input LMMSE filter to outperform the traditional LMMSE filter.

In real applications, we only have the acquired image data rather than the true spectrum for it. To overcome this problem, we can assume that the images are ergodic, and estimate the spectrum by partitioning the image, and taking the average spectra of the each of the blocks.

In summary, a multiple input LMMSE filter for image fusion was derived. The validity of the approach was demonstrated by comparing the performance of the filter with the results obtained with a traditional one input LMMSE filter. This method outperforms reconstruction algorithms that use only one input by exploiting the information contained in the cross-correlation of two images that have undergone different degradation processes. The performance improvements are apparent from the expression derived for the mean square error as well as from the experimental results.

Further improvements can be obtained if we have explicit knowledge of the degradation transfer function, and estimates of the noise and signal spectra.

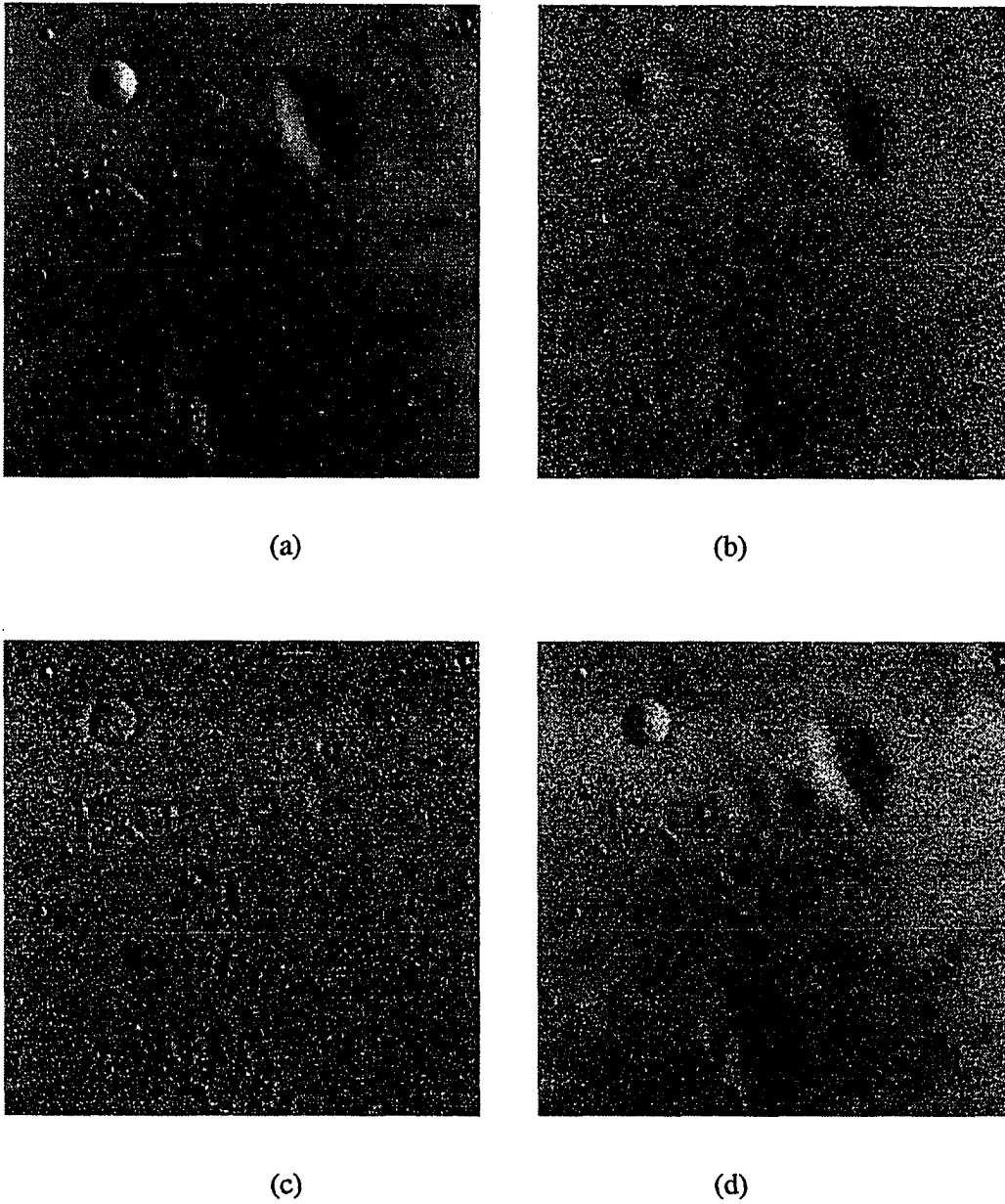


Figure 4.4. Multiple input LMMSE filtered image.(a) Original image; (b) Degraded image 1 with additive noise; (c) Degraded image 2 with additive noise; (d) Multiple input LMMSE filtered image.

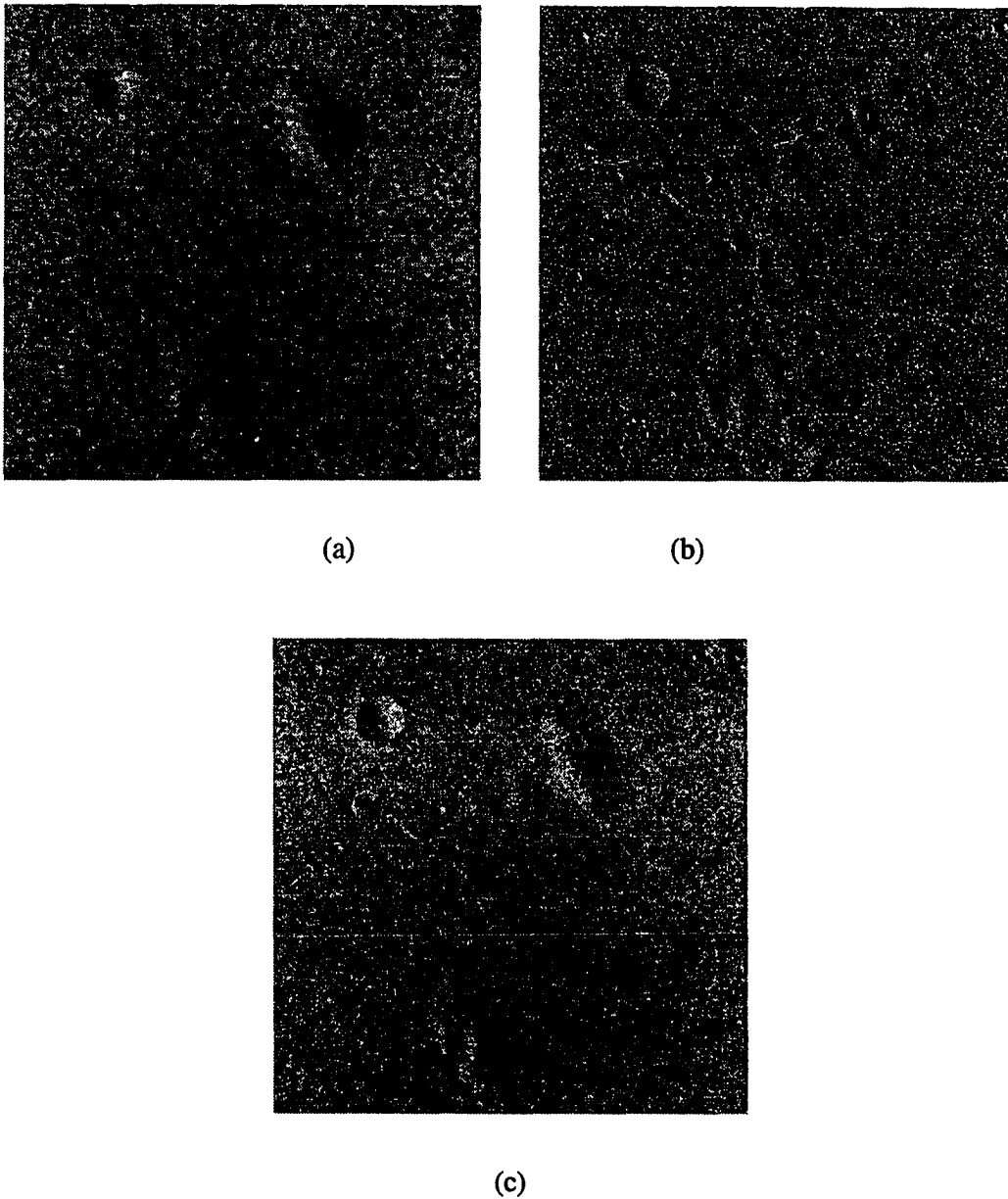


Figure 4.5. Comparison with one input LMMSE filter. (a) 1-input LMMSE filtered image of Figure 4.3 (b); (b) 1-input LMMSE filtered image of Figure 4.3 (c); (c) Average of images shown in (a) and (b).

CHAPTER V

DATA FUSION USING MULTI-RESOLUTION DECOMPOSITION TECHNIQUES

This chapter presents an image fusion algorithm using multi-resolution decomposition techniques for combining ultrasonic and eddy current images. The approach uses a model that assumes we have multiple input images that have experienced various linear degradations and have additive noise. This chapter shows how the multi-resolution decomposition method can be utilized to implement a linear minimum mean square error (LMMSE) filter using this model, and presents a wavelet based LMMSE filter designed to fuse multiple images.

5.1 Two Input Multi-resolution Filter

To implement the LMMSE filter, we need to know statistical characteristics of signals and noise along with the transfer functions associated with the degradation processes. Unfortunately it is often difficult to estimate the transfer function or frequency response associated with the degradation process. Fortunately we can exploit the fact that the processes are ergodic and the frequency responses are reasonably smooth. Under these conditions we can use multi-resolution decomposition techniques to obtain sub-band signals, and use them to obtain block estimates of the spectrum.

The linear minimum mean square error (LMMSE) filter for a two input system is given by (5.1).

$$G_j(\omega_1, \omega_2) = \frac{S_s(\omega_1, \omega_2)}{S_{n_j}(\omega_1, \omega_2)} \frac{H_j^*(\omega_1, \omega_2)}{1 + \sum_{i=1}^2 \frac{S_s(\omega_1, \omega_2)}{S_{n_i}(\omega_1, \omega_2)} |H_i(\omega_1, \omega_2)|^2} \text{ for } 1 \leq j \leq 2. \quad (5.1)$$

The equation can be modified to the following form using the spectra of the acquired data instead of transfer function associated with the degradations.

$$G_j(\omega_1, \omega_2) = \frac{\sqrt{S_s(\omega_1, \omega_2)} (S_{x_j}(\omega_1, \omega_2) - S_{n_j}(\omega_1, \omega_2))}{-S_{n_j}(\omega_1, \omega_2) + S_{n_j}(\omega_1, \omega_2) \sum_{i=1}^2 \frac{S_{x_i}(\omega_1, \omega_2)}{S_{n_i}(\omega_1, \omega_2)}} \text{ for } 1 \leq j \leq 2. \quad (5.2)$$

When the noise spectrum is much smaller than the signal spectrum and identical to each other, i.e., $S_{n_1}(\omega_1, \omega_2) = S_{n_2}(\omega_1, \omega_2) = S_n(\omega_1, \omega_2)$ and $S_{x_j}(\omega_1, \omega_2) \gg S_n(\omega_1, \omega_2)$, for $1 \leq j \leq 2$, the estimated image is given by

$$\hat{S}(\omega_1, \omega_2) = \frac{\sqrt{S_s(\omega_1, \omega_2)}}{S_{x_1}(\omega_1, \omega_2) + S_{x_2}(\omega_1, \omega_2)} \times \left\{ \sqrt{S_{x_1}(\omega_1, \omega_2)} X_1(\omega_1, \omega_2) + \sqrt{S_{x_2}(\omega_1, \omega_2)} X_2(\omega_1, \omega_2) \right\} \quad (5.3)$$

When we do not have the spectrum for the original signal, we can use the approximation.

$$\hat{S}(\omega_1, \omega_2) = K \left\{ \sqrt{S_{x_1}} X_1 + \sqrt{S_{x_2}} X_2 \right\} \quad (5.4)$$

Unfortunately, unless we have enough number of sample images, this variance associated with the estimate is very high and consequently the filter may not work reliably.

As we usually have only one set of images for each trial, we are confronted with the task of estimating the spectral distribution with a single image for each case. A commonly

used method [101] to estimate the image spectrum under these conditions is to partition the image into several sub-regions and obtain the spectral estimates for each sub-region. This partitioning can be accomplished using sub-band coding techniques. The basic idea of sub-band coding of images is to decompose an image into several sub-images instead of using the original image, and estimate the block spectrum of each sub-band. The block spectra are used for estimating the spectrum of the full image.

5.2 Multi-resolution Decomposition

According to the Nyquist's sampling theorem, an image should be sampled with at a rate that is at least twice the maximum spatial frequency in the image. The Fourier transform of the discrete image covers the frequency range from dc to the half the spatial sampling frequency. Image processing algorithms that exploit features representing shapes have difficulty dealing with this wide spectrum. The wide spectrum represents a range of shapes including both fine and coarse shapes. This is true unless the image is known to have limited range of shapes and consequently has a band-pass spectrum. Often we can divide the image signal into the several sets of narrow spatial frequency bands. This operation is equivalent to isolating the fine structures from the coarse structures in the image. Thus we can isolate and process the image features easily using the set of narrow band image signals. Multi-resolution decomposition techniques involve signal decomposition into frequency bands of constant bandwidth on a logarithmic scale. Multi-

resolution decomposition techniques have been used extensively in applications ranging from image understanding, machine vision and image compression [89].

When we decompose multiple images that have undergone various degradations, we can identify image regions using multi-resolution techniques that provide the shape information. One heuristic method of fusing images is to selectively choose sub-regions from multiple images, that are related to the degradations in the different frequency bands. Using this approach we will decompose the image into sub-bands using multi-resolution techniques first and then apply the fusion method described by equation (5.4).

Given a sequence of increasing resolutions $(r_j)_{j \in \mathbf{Z}}$, the vector spaces, W_{r_j} , of the details of an image at resolution r_j are defined as the difference of vector spaces of information between its approximation $V_{r_{j+1}}$ at the higher resolution r_{j+1} and its approximation V_{r_j} at the lower resolution r_j [104].

$$W_{r_j} = V_{r_{j+1}} - V_{r_j}, \quad j \in \mathbf{Z} \quad (\mathbf{Z} \text{ is the set of integer}) \quad (5.5)$$

Then image $V_{r_{n+1}}$ at the original resolution r_{n+1} is given by:

$$V_{r_{n+1}} = \sum_{j=-\infty}^n W_{r_j} \quad (5.6)$$

A multi-resolution representation can be rendered scale-invariant if the sequence of resolution parameters $(r_j)_{j \in \mathbf{Z}}$ varies exponentially. Let us suppose that we chose the resolution step as 2 so that $r_j = 2^j$. If the step size is 2 times smaller, each object of the

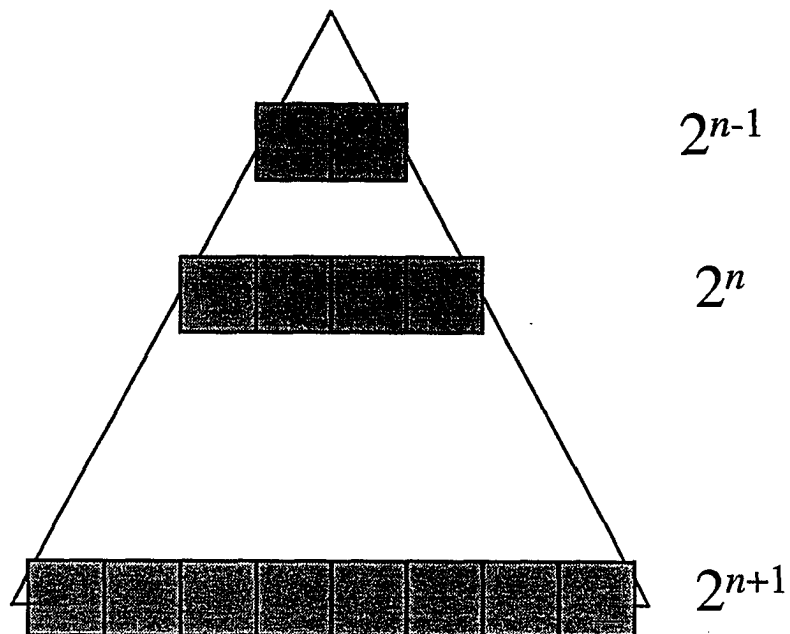


Figure 5.1. Pyramidal image structure for one-dimensional signal.

scene is projected on an area that is $2^j \times 2^j$ times larger in the obtained image. That is, each object is measured at a resolution that is 2 times larger. Hence, the details of this new image at resolution 2^j corresponds to the details of the previous image at resolution 2^{j-1} . Rescaling the image by 2 translates the image details along the resolution axis. Figure 5.1 and Figure 5.2 show the pyramid multi-resolution structure for one and two dimension signals.

The Laplacian pyramid has been used commonly to regroup the details at different resolutions into a pyramid structure [91,93]. The Laplacian pyramid data structures, suffer from the difficulty that data at separate levels are correlated. A simple approach for handling this correlation is not available. It is therefore difficult to know whether the

similarity between the image details at different resolutions is due to a property of the image itself or due to the intrinsic redundancy associated with the representation. Furthermore, the Laplacian multi-resolution representation does not introduce any spatial orientation selectivity into the decomposition process.

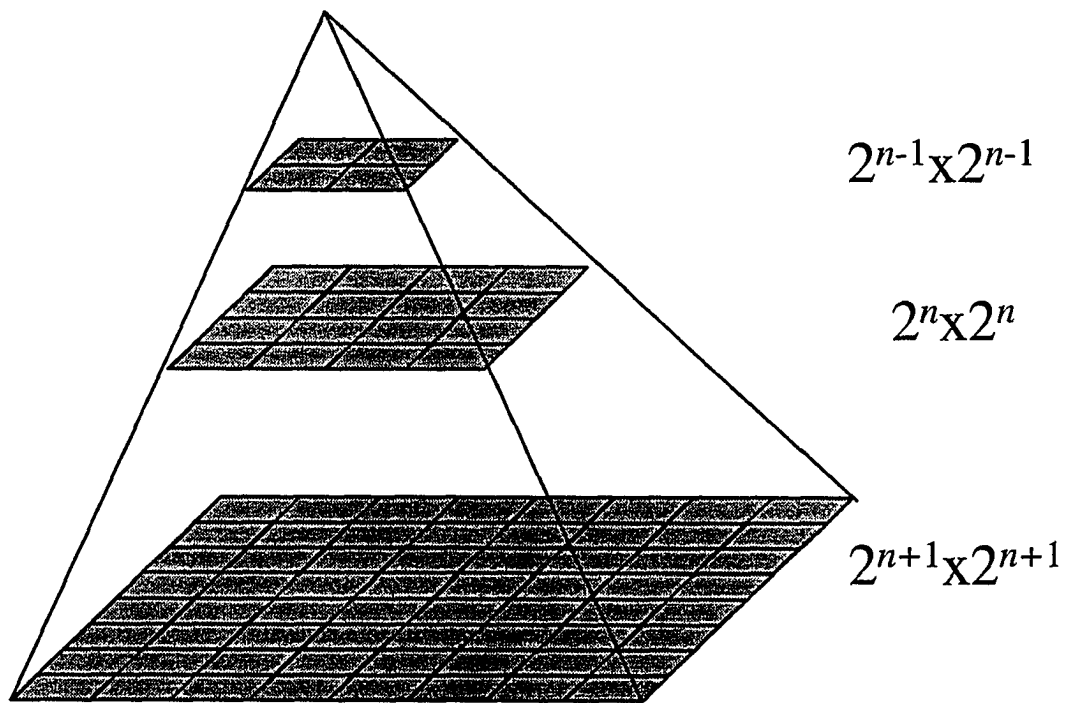


Figure 5.2. Pyramidal image structure for two-dimensional signals.

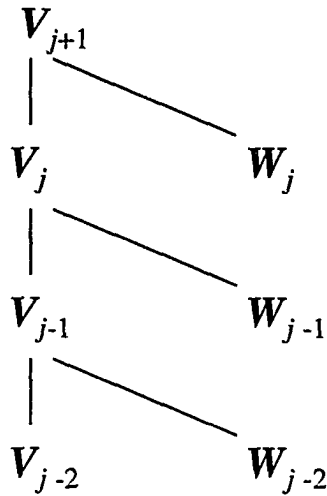


Figure 5.3. Vector decomposition.

The difference in information between the two approximations at resolutions 2^{j+1} and 2^j is called the detail signal at resolution 2^j . The approximation at resolution 2^{j+1} and 2^j of a signal are respectively equal to its orthogonal projection on $V_{2^{j+1}}$ and V_{2^j} . The detail signal at resolution 2^j is given by the orthogonal projection of the original signal on the orthogonal complement of V_{2^j} in $V_{2^{j+1}}$. Let W_{2^j} be this orthogonal complement. To compute the orthogonal projection of a function $f(x)$ on W_{2^j} , we need to find an orthonormal basis of W_{2^j} . The approximated signal at a resolution 2^j is equal to the orthogonal projection on a space V_{2^j} . The decomposition scheme is illustrated in Figure 5.3. The domain for the decomposed vector is illustrated as shown in Figure 5.4.

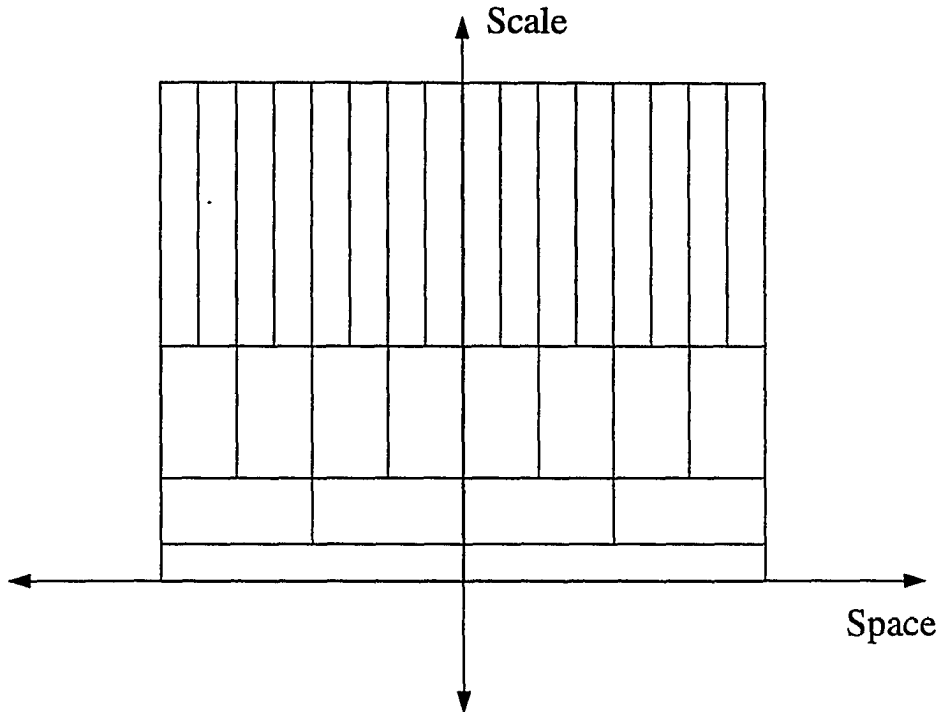


Figure 5.4. Scale-space resolution.

5.3 Multi-resolution Decomposition Using Orthogonal Transform

5.3.1 Signal Representation Using Orthogonal Functions

As a practical example of the multi-resolution decomposition method, we will show how orthogonal transforms can be used to decompose the signal. A set of real-valued discrete functions $\{u_k(n): k = 0, 1, \dots, N-1\}$ is orthogonal on the interval $(0, N-1)$ if

$$\sum_{n=0}^{N-1} u_m(n)u_n(n) = \begin{cases} c, & \text{if } m = n \\ 0, & \text{if } m \neq n \end{cases} \quad (5.7)$$

When $c = 1$, $\{u_n(n)\}$ is said to be an orthonormal set. If $x(n)$ is a real-valued signal defined on the interval $(0, N-1)$, then it can be represented by the expansion

$$x(n) = \sum_{k=0}^{N-1} a_k u_k(n) \quad (5.8)$$

where a_k denotes the k -th coefficient in the expansion.

A unitary transformation is a specific type of linear transformation in which the basic linear operation of (5.8) is exactly invertible and the operation kernel satisfies orthogonality conditions (5.7). The discrete Fourier transform (DFT) and the discrete cosine transform (DCT) are examples of well known discrete unitary transforms.

We restrict the basis function that satisfies the following property.

$$u_{2k}(n) = u_k(2n) \quad (5.9)$$

Again, Fourier and cosine transforms are some of the examples satisfying the above scalable property. We can rewrite (5.8) as follows.

$$x(n) = a_0 u_0(n) + \sum_{j=0}^{\log_2 N-1} \left\{ \sum_{k=2^j}^{2^{j+1}-1} a_k u_k(n) \right\} \quad (5.10)$$

If we define the basis for resolution j as follows :

$$V_{2^j} = \{u_k(n) | 0 \leq k < 2^{j+1}\} \quad (5.11)$$

and the basis for the detail signal as :

$$W_{2^j} = V_{2^{j+1}} - V_{2^j} \quad (5.12)$$

and define

$$A_j = \{a_k | 0 \leq k < 2^j\} \quad (5.15)$$

then we have a multi-resolution transform structure based on unitary transforms. Here A_j represents j -th sub-band decomposed signal of $x(n)$.

5.3.2 Fourier Representation of Signals

Fourier series is an example of the general treatment of orthogonal representations, where the set of functions $\{u_k(n)\}$ are the Fourier sinusoidal functions $\{e^{2\pi kn/N}\}$. The series expansion corresponding to equation (5.8) is given by

$$x(n) = \frac{1}{\sqrt{N}} \sum_{k=0}^{N-1} a_k e^{j \frac{2\pi kn}{N}}, \quad 0 \leq n < N-1 \quad (5.14)$$

$$u_k(n) = \frac{1}{\sqrt{N}} e^{j \frac{2\pi kn}{N}}, \quad 0 \leq k, n < N-1 \quad (5.15)$$

$$a_k = \frac{1}{\sqrt{N}} \sum_{n=0}^{N-1} x(n) e^{-j \frac{2\pi kn}{N}}, \quad 0 \leq k < N-1 \quad (5.16)$$

The transforms discussed thus far can easily be extended to the two-dimensional case. The $M \times N$ two-dimensional transforms and their inverses can be computed by means of $M \times N$ applications of the algorithms used to compute the corresponding one-dimensional

transforms. We showed here DFT as a method of multi-resolution decomposition. However, other orthogonal transformations like the DCT can be used to decompose images.

We can estimate the block spectrum in the resolution region given by (5.11).

$$\begin{aligned}
 \hat{S}_x(k) \Big|_{\text{resolution-}j} &= \mathbf{E}_j \left[|a_k|^2 \right] \\
 &\equiv \frac{1}{2^j} \sum_{k=2^j}^{2^{j+1}-1} |a_k|^2 \\
 &= \frac{1}{2^j} \|\mathbf{A}_{j+1} - \mathbf{A}_j\|^2
 \end{aligned} \tag{5.17}$$

5.3.3 Discrete Cosine Transform (DCT)

It is well known that the Fourier series of any continuous real and symmetric function contains only real coefficients corresponding to the cosine terms of the series. The result can be extended to the discrete Fourier transform of a signal by forcing symmetry. Let a symmetrical signal be formed by the reflection of the signal array about its boundary according to the relation

$$x_s(n) = \begin{cases} x(n) & n \geq 0 \\ x(-1-n) & n < 0 \end{cases} \tag{5.18}$$

By this construction, $x_s(n)$ is symmetrical about the point $n = -1/2$.

Taking a Fourier transform about the point of symmetry results in

$$\mathcal{F}_s(k) = \frac{1}{2N} \sum_{n=-N}^{N-1} x_s(n) e^{\frac{-2\pi j}{2N} k \left(n + \frac{1}{2} \right)} \quad \text{for } k = -N, \dots, 0, \dots, N-1. \tag{5.19}$$

Because $x_s(n)$ is real and symmetric, equation (5.19) reduces to

$$\mathcal{F}_s(k) = \frac{2}{N} \sum_{n=0}^{N-1} x(n) \cos\left\{\frac{\pi}{N} k \left(n + \frac{1}{2}\right)\right\}, \quad 0 \leq k < N-1. \quad (5.20)$$

$$x(n) = \frac{2}{N} \sum_{k=0}^{N-1} a(k) \mathcal{F}_s(k) \cos\left\{\frac{\pi}{N} k \left(n + \frac{1}{2}\right)\right\}, \quad 0 \leq n < N-1. \quad (5.21)$$

$$u_k(n) = \frac{2}{N} a(k) \cos\left\{\frac{\pi}{N} k \left(n + \frac{1}{2}\right)\right\} \quad 0 \leq k, n < N-1. \quad (5.22)$$

The DCT has the important property that its basis vectors closely approximate the eigen vectors of a class of matrices called Toeplitz matrices

Often the DCT is used to approximate the Fourier transform. It is apparent that the DCT is equivalent to the Fourier transform for certain types of symmetric signals. The properties of the DCT are similar to the Fourier transform, and the transformed domain is often called the frequency domain. One of merits of the DCT is its computational convenience since it does not involve calculations involving complex numbers. Unlike the Fourier transform which generates a conjugate symmetric frequency spectrum, the DCT produces a real transform. As a result of these merits, the DCT is commonly used in image processing, especially for image compression.

We will now examine the use of the DCT for data fusion.

5.4 Fusion in Transform Domain

One possible option for fusing images in the transform domain is to mix the two images based on the spectrum of the signal. However, in order to obtain a consistent spectral estimate with a single image, we divide the spectral domain to several sub-regions, and obtain the estimate of the spectrum for each sub-region. The estimate of the spectrum for the full image is obtained by combining the spectra of these sub-regions. One of the strategies employed for obtaining the full image spectrum from the sub-regions is based on sub-band coding.

Sub-band coding was introduced to code speech signals in 1976 [74]. Successes obtained in applying the sub-band coding technique in the field of speech coding have led to its expanded use in such areas as audio signal coding, and image coding [101].

The basic idea of image sub-band coding is to decompose an image into several sub-images. We partition the image into sub-bands similar to the method used in speech sub-band coding and estimate the block spectrum of each sub-band. The strategy is based on the assumption that the transfer functions associated with the degradation are functions of frequency and the signals in the each sub-band undergo similar effects.

Figure 5.5 shows the ultrasonic and eddy current image used in the experiment for validating the approach. Figure 5.6 shows sub-images of each sub-band divided image for the ultrasonic image, and Figure 5.7 shows sub-images of each sub-band image for the eddy current case.

The Linear minimum mean square error (LMMSE) filter for the two input system is given by (5.23).

$$G_j(z_1, z_2) = \frac{S_s(z_1, z_2)}{S_{n_j}(z_1, z_2)} \frac{H_j(z^{-1}_1, z^{-1}_2)}{1 + \sum_{i=1}^N \frac{S_s(z_1, z_2)}{S_{n_i}(z_1, z_2)} |H_i(z_1, z_2)|^2} \quad \text{for } 1 \leq j \leq N. \quad (5.23)$$

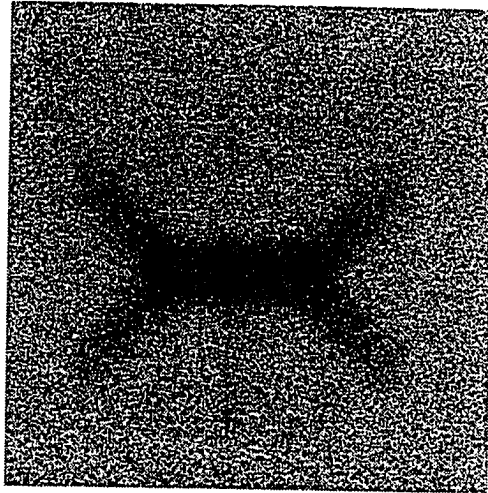
This can be modified to a form where we use the spectrum of the acquired data instead of transfer function associated with the degradation.

$$G_j(z^1, z^2) = \frac{\sqrt{S_s(z^1, z^2)} (S_{x_j}(z^1, z^2) - S_{n_j}(z^1, z^2))}{-S_{n_j}(z^1, z^2) + S_{n_j}(z^1, z^2) \sum_{i=1}^2 \frac{S_{x_i}(z^1, z^2)}{S_{n_i}(z^1, z^2)}} \quad \text{for } 1 \leq j \leq 2. \quad (5.24)$$

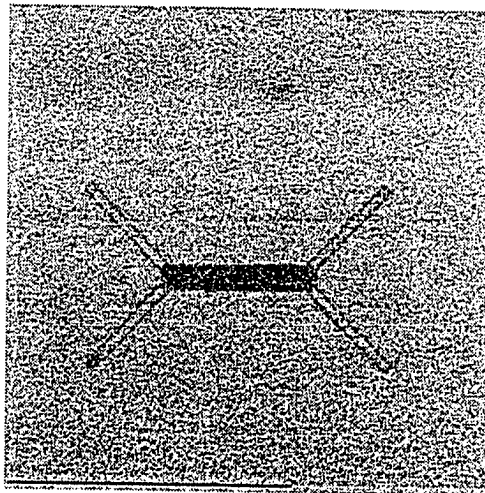
When the noise spectra are much smaller than the signal spectrum and are all identical, i.e., $S_{n_j} = S_n$ and $S_{x_j} \gg S_n$, for $1 \leq j \leq 2$, (5.24) becomes.

$$G_j(z^1, z^2) = \frac{\sqrt{S_s(z^1, z^2)} S_{x_j}(z^1, z^2)}{S_{x_1}(z^1, z^2) + S_{x_2}(z^1, z^2)} \quad \text{for } 1 \leq j \leq 2. \quad (5.25)$$

When we do not have the spectrum for the original signal, we can use the approximation :



(a)



(b)

Figure 5.5. Ultrasonic image and eddy current image. a) Ultrasonic image with noise; b) Eddy current image with noise.

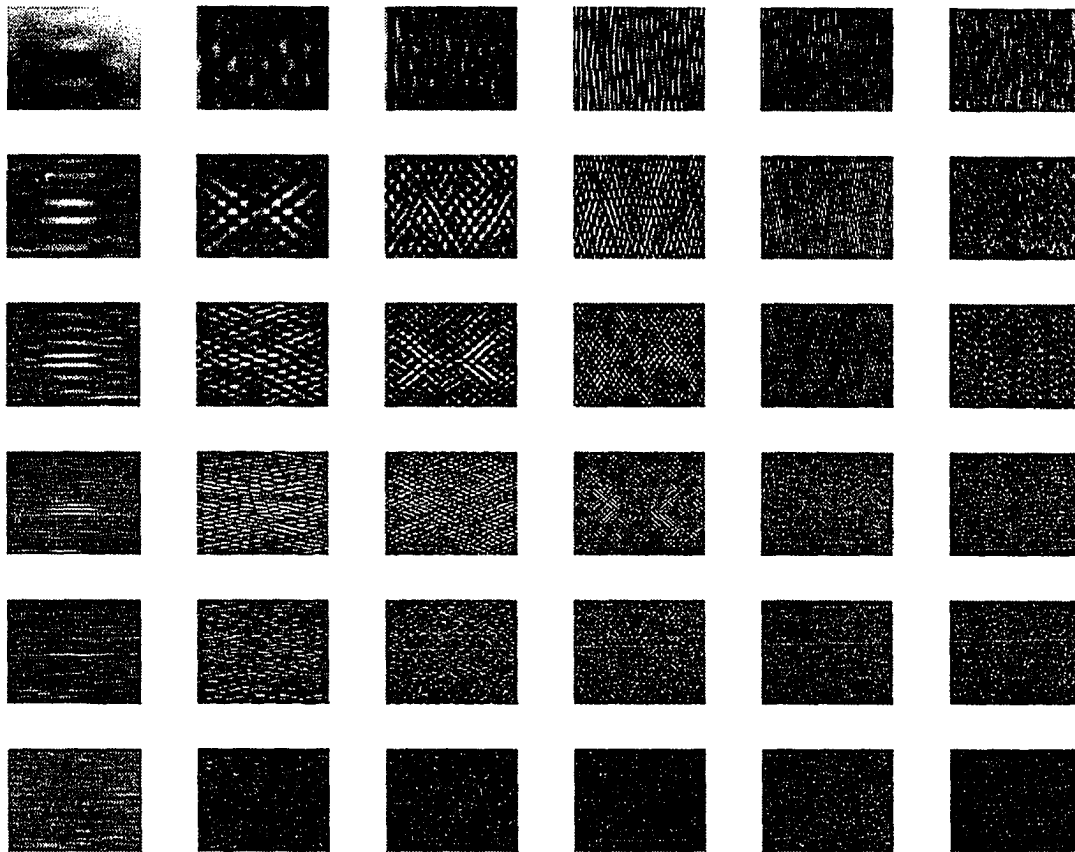


Figure 5.6. Sub-band images for ultrasonic image.

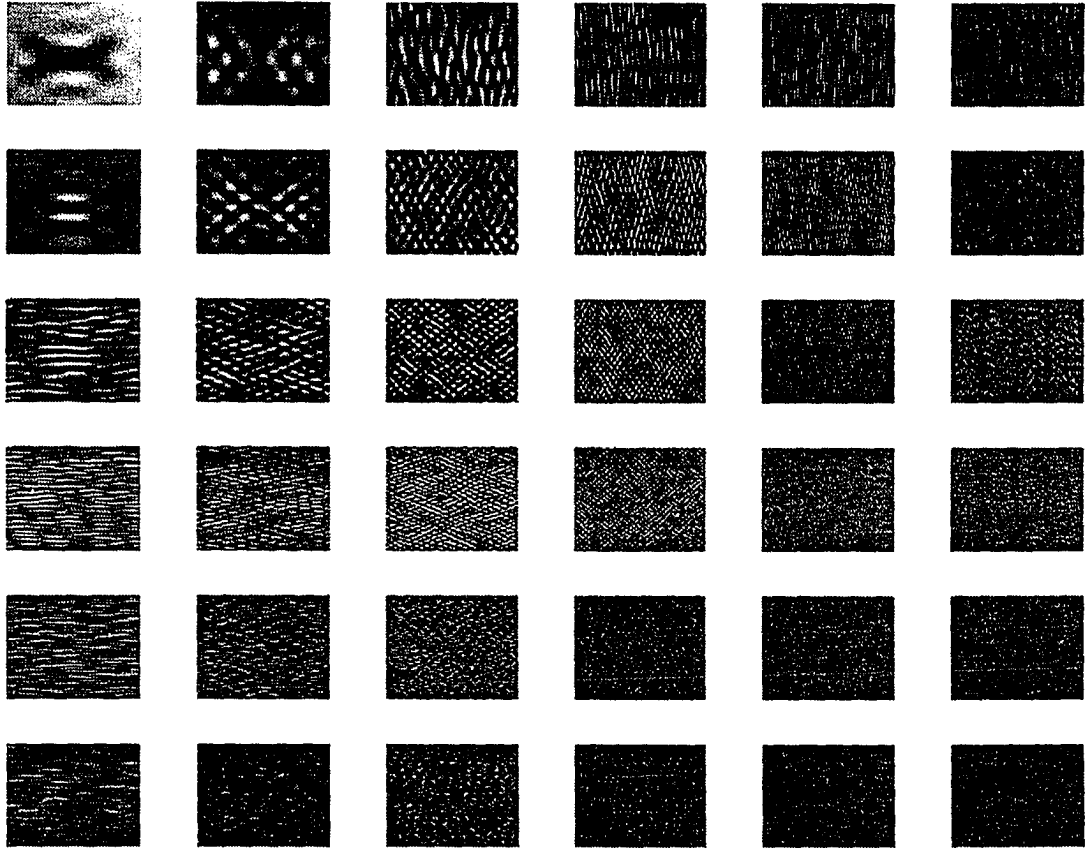


Figure 5.7. Sub-band images for eddy current image.

$$G_j(z^1, z^2) = K \frac{\sqrt{S_{x_j}(z^1, z^2)}}{S_{x_1}(z^1, z^2) + S_{x_2}(z^1, z^2)} \text{ for } 1 \leq j \leq 2. \quad (5.26)$$

Figure 5.8 shows the ratio of spectra for the ultrasonic and eddy current images.

Figure 5.9, 5.10, 5.11 shows the result of fusing the images using this approach.

5.5 Wavelet Based Decomposition

Wavelets were introduced by Grossmann and Morlet [94] as functions $\psi(x)$ whose translations and dilations can be used for expansions of $L^2(\mathbf{R})$ functions. It was shown that there exists wavelets $\psi(x)$ such that translations and dilations of $\psi(x)$ is an orthonormal basis of $L^2(\mathbf{R})$ [104]. Wavelet transforms are being used extensively to decompose images into sub-bands, in such areas as image compression.

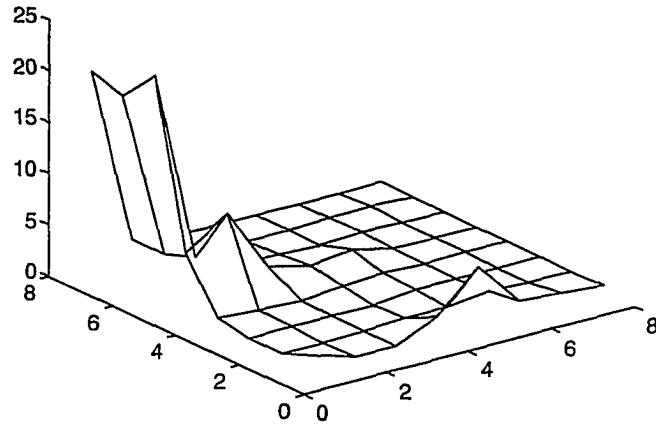
We begin by presenting the notation used in deriving the algorithm.

\mathbf{Z} : the set of integers

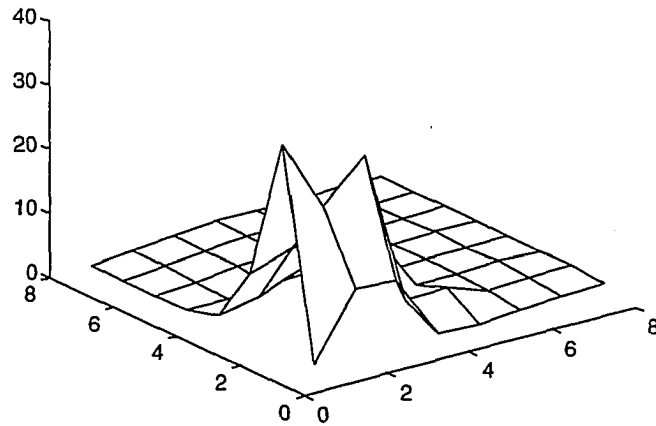
\mathbf{R} : the set of real numbers

$L^2(\mathbf{R})$ denotes the vector space of measurable, square-integrable one-dimensional functions $f(x)$.

$L^2(\mathbf{R}^2)$ denotes the vector space of measurable, square-integrable two-dimensional functions $f(x,y)$.



(a)



(b)

Figure 5.8. Ratio of spectra of ultrasonic and eddy current images. a) Ratio of spectrum of ultrasonic / eddy current images; b) Ratio of spectrum of eddy current / ultrasonic images.

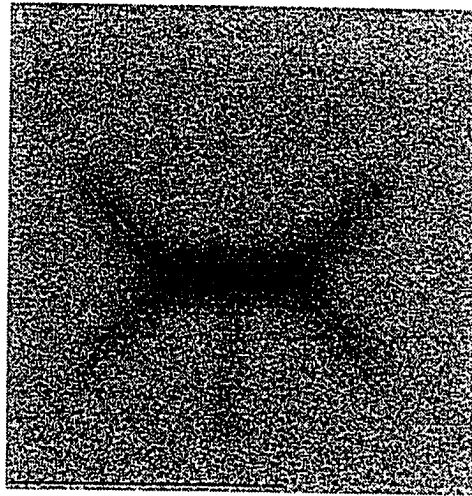


Figure 5.9. Fused image obtained using transform domain techniques employing a 4x4 block.

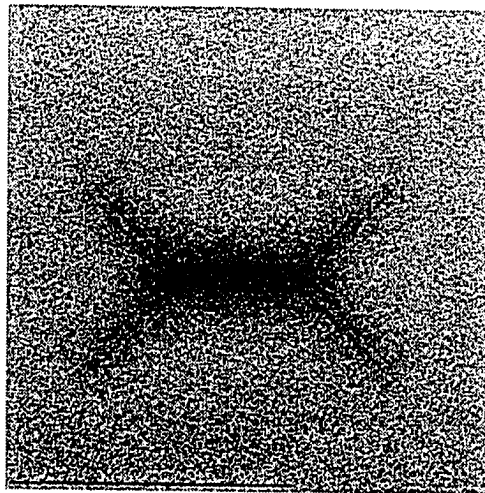


Figure 5.10. Fused image obtained using transform domain techniques employing a 6x6 block.

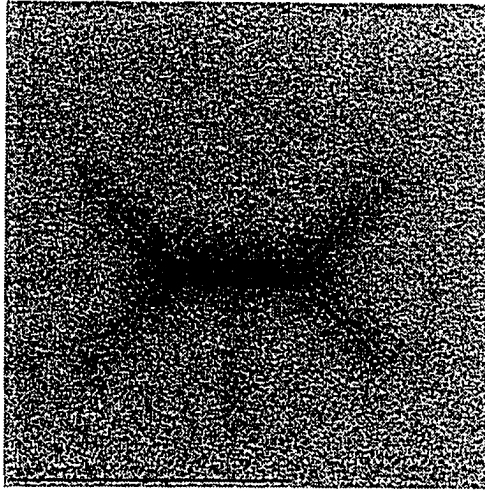


Figure 5.11. Fused image obtained using transform domain techniques employing a 8×8 block.

It is known that the computation associated with the wavelet representation may be accomplished using a pyramidal algorithm based on convolutions with quadrature mirror filters. The signal can also be reconstructed from a wavelet representation with a similar pyramidal algorithm.

The approximation of a signal $f(x)$ at a resolution 2^j is equal to its orthogonal projection on the vector space V_{2^j} . We use the scaling function $\varphi(x) \in L^2(\mathbf{R})$ such that $\varphi_{2^j}(x) = \sqrt{2^j} \varphi(2^j x)$ for $j \in \mathbf{Z}$, is an orthonormal basis of V_{2^j} . Similarly we call wavelet function $\psi(x) \in L^2(\mathbf{R})$ such that $\psi_{2^j}(x) = \sqrt{2^j} \psi(2^j x)$ then is an orthonormal basis of W_{2^j} . The scaling function $\varphi(x)$ and wavelet function ψ are unique with respect to a particular multi-resolution approximation of $L^2(\mathbf{R})$. For any resolution 2^j , the family of functions

$$\left(\varphi_{2^j}(x-2^{-j}n)\right)_{n \in \mathbb{Z}}, \left(\psi_{2^j}(x-2^{-j}n)\right)_{n \in \mathbb{Z}}$$

constitute an orthonormal basis of V_{2^j} and W_{2^j} . We can regard the scaling function and wavelet function as a low pass filter kernel and band pass filter kernel with non-ideal characteristics. The wavelet model can be easily generalized to any dimension $n > 0$ [73]. A multi-resolution approximation of $L^2(\mathbb{R}^2)$ is a sequence of sub-spaces of $L^2(\mathbb{R}^2)$ which satisfies a straightforward two-dimensional extension of the properties associated with the one-dimensional case.

Now we will study the two-dimensional case for image processing applications. We assume that the signal is a finite energy function $f(x,y) \in L^2(\mathbb{R}^2)$. A multi-resolution approximation of $L^2(\mathbb{R}^2)$ is a sequence of sub-spaces of $L^2(\mathbb{R}^2)$ which satisfies a straightforward two-dimensional extension of the properties (5.3) to (5.5). Let (V_{2^j}) be such a multi-resolution approximation of $L^2(\mathbb{R}^2)$. The approximation of a signal $f(x,y)$ at a resolution 2^j is equal to its orthogonal projection on the vector space V_{2^j} . Let $\varphi_{2^j}(x,y) = 2^{2j} \varphi(2^j x, 2^j y)$. The family of functions forms an orthonormal basis of V_{2^j} . The factor 2^{2j} normalizes each function in the $L^2(\mathbb{R}^2)$ norm. The function $\varphi(x,y)$ is unique with respect to a particular multi-resolution approximation of $L^2(\mathbb{R}^2)$.

For separable multi-resolution approximations of $L^2(\mathbb{R}^2)$, each vector space V_{2^j} can be decomposed as a tensor product of two identical sub-spaces of $L^2(\mathbb{R})$. As in the one-dimensional case, the detail signal at the resolution 2^j is equal to the orthogonal projection of the signal on the orthogonal complement of V_{2^j} in $V_{2^{j+1}}$.

$$V_{2^j} = V_{2^{j-1}} \times V_{2^{j-1}} \quad (5.27)$$

The sequence of vector spaces $(V_{2^j})_{j \in \mathbf{Z}}$ forms a multi-resolution approximation of $L^2(\mathbf{R})$. One can then easily show that the scaling function $\varphi(x,y)$ can be written as

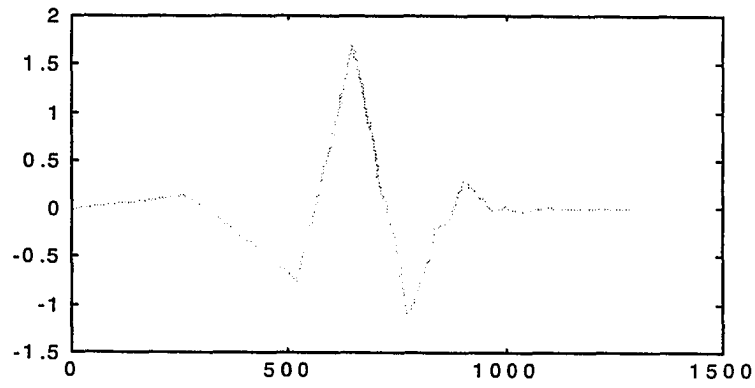
$$\varphi(x,y) = \varphi(x) \varphi(y) \quad (5.28)$$

where $\varphi(x)$ is the one-dimensional scaling function of the multi-resolution approximation $(V_{2^j})_{j \in \mathbf{Z}}$.

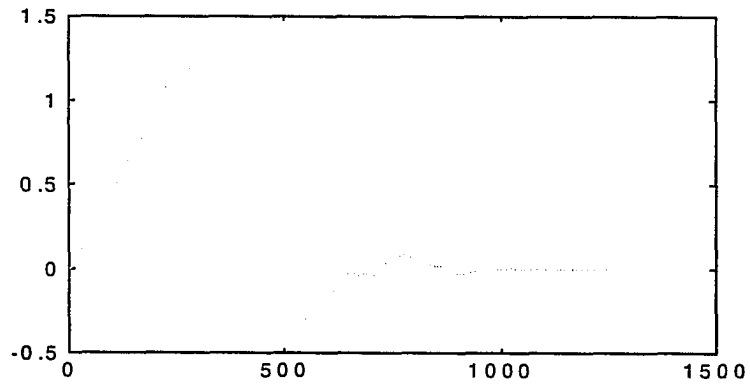
As in the one-dimensional case, the detail signal at the resolution 2^j is equal to the orthogonal projection of the signal on the orthogonal complement of V_{2^j} in $V_{2^{j+1}}$. Let O_{2^j} be this orthogonal complement. We can build an orthonormal basis of O_{2^j} by scaling and translating the wavelets function $\psi(x,y)$.

The wavelet decomposition can thus be interpreted as a signal decomposition in a set of independent, spatially oriented frequency channels. Let us suppose that $\varphi(x)$ and $\psi(x)$ are, respectively, a perfect low-pass and a perfect band-pass filter. Figure 5.12 shows the wavelet function and scale function used for experiment. Figure 5.13 and 5.14 show the QMF (Quadrature Mirror Filter) used to implement forward wavelet transform and inverse wavelet transform.

We can call the decomposed set of images as an orthogonal wavelet representation in two dimensions. The total number of pixels in this new representation is equal to the number of pixels in the original image, so we do not increase the volume of data. Once again, this occurs due to the orthogonality of the representation.



(a)



(b)

Figure 5.12. Scale and wavelet functions used. (a) Wavelet function $\psi(x)$; (b) Scale function $\phi(x)$.

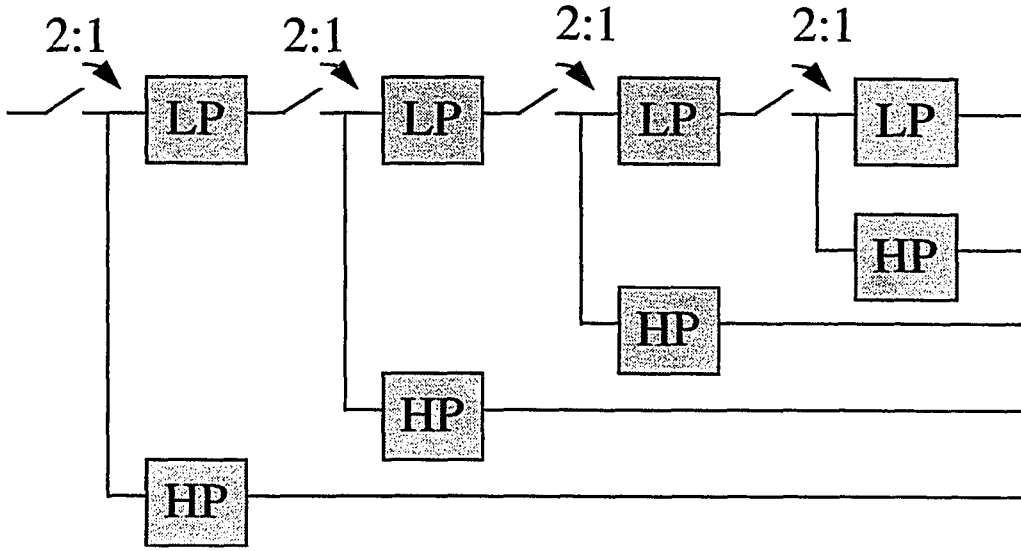


Figure 5.13. QMF for forward wavelet transform.

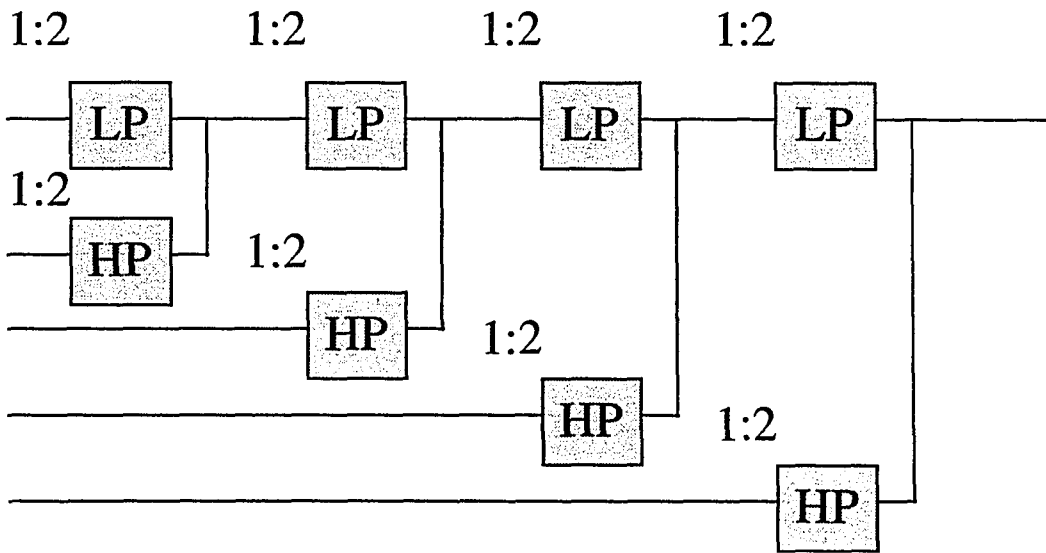


Figure 5.14. QMF for inverse wavelet transform.

In a correlated multi-resolution representation such as the Laplacian pyramid, the total number of pixels representing the signal is increased by a factor of 2 in one dimension and of $4/3$ in two dimensions.

In two dimensions, the wavelet representation can be computed with a pyramidal algorithm similar to the one-dimensional algorithm. The one-dimensional reconstruction algorithm described can also be extended to two dimensions.

Using the wavelet transform as a tool to decompose image into sub-bands, we can use same fusion strategy as was used to fuse the transform domain block.

We estimate the block spectrum for the decomposed sub-band images and apply the fusion algorithm based on (5.28). Figure 5.15 and 5.16 shows the sub-band wavelet images for ultrasonic and eddy current images respectively. Figure 5.17, 5.18 and 5.19 show the fused images using the wavelet transform based multi-resolution decomposition techniques. The performance improves by increasing the number of sub-bands to a certain degree. After the number of sub-bands reaches 7×7 , the improvement is not noticeable any more.

5.6 Decomposition and Reconstruction Algorithm in Two Dimensions

In two dimensions, the wavelet representation can be computed using a pyramidal algorithm similar to the one-dimensional algorithm.

The two-dimensional wavelet transform can be seen as a one-dimensional wavelet transform along the x and y axis. It is known that a two-dimensional wavelet transform can be computed with a separable extension of the one-dimensional decomposition algorithm.

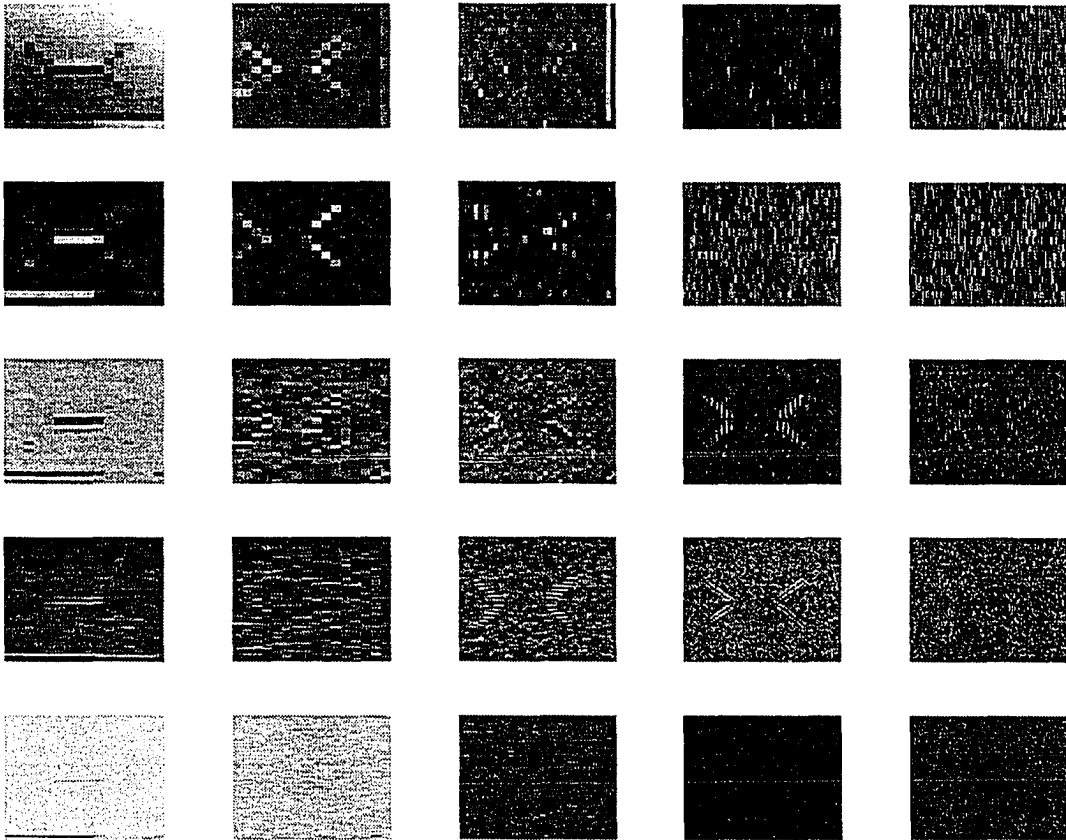


Figure 5.15. Sub-band wavelet images for the ultrasonic image.

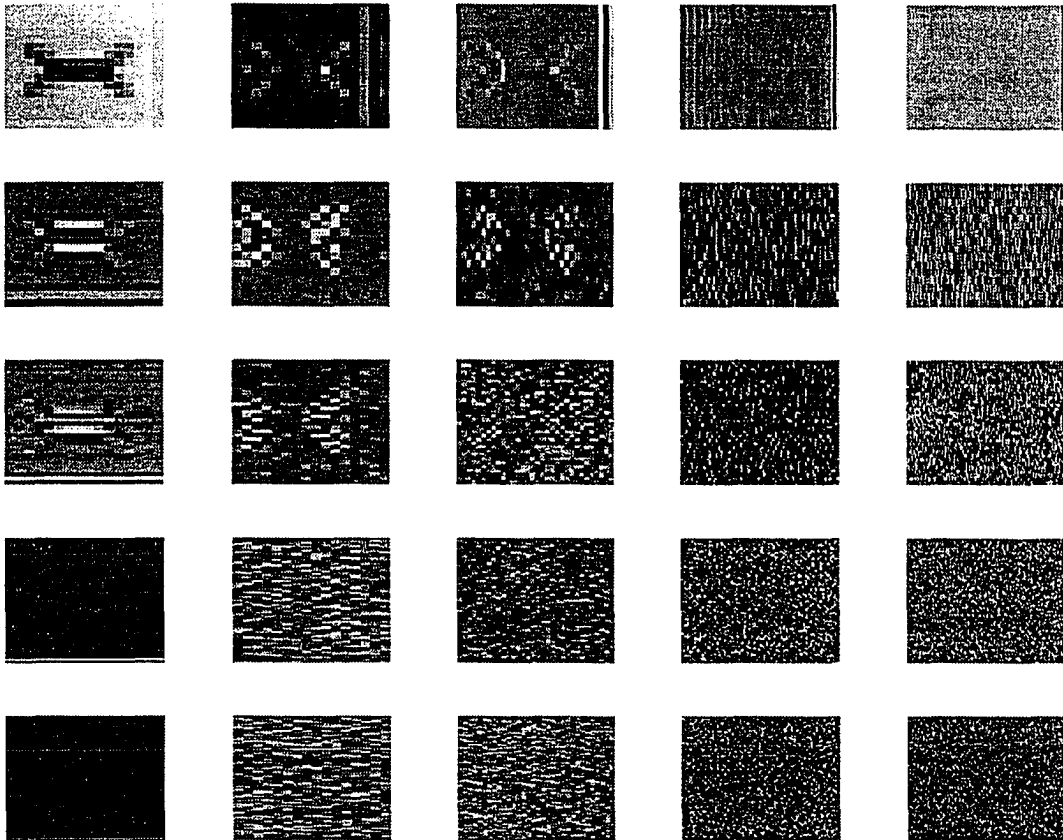


Figure 5.16. Sub-band wavelet images for the eddy current image.

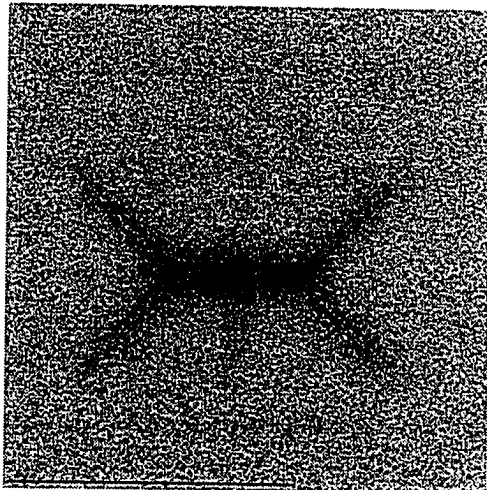


Figure 5.17. Fused image obtained using wavelet transformation employing a 4x4 block.

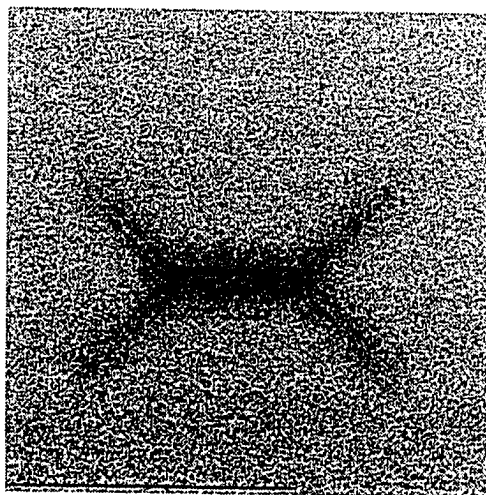


Figure 5.18. Fused image obtained using wavelet transformation employing a 6x6 block.

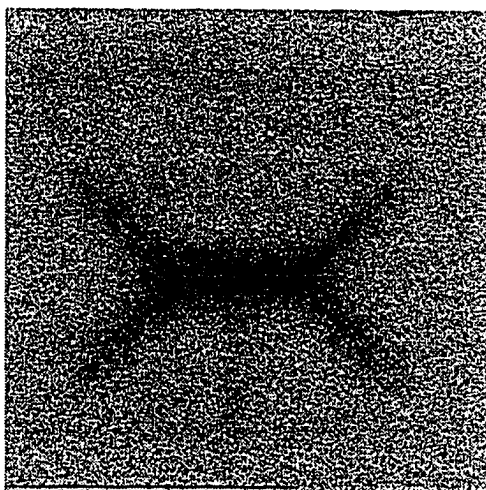


Figure 5.19. Fused image obtained using wavelet transformation employing a 8x8 block.

We first convolve the rows of image $u(x,y)$ with a one dimensional filter, retain every other row, convolve the columns of the resulting signals with another one-dimensional filter and retain every other column.

The one-dimensional reconstruction algorithm described in the previous section can also be extended to two dimensions. At each step, the image $u(x,y)$ is reconstructed using the following method. We add a column of zeros between each column of the images, convolve the rows with a one dimensional filter, add a row of zeros between each row of the resulting image, and convolve the columns with another one-dimensional filter.

The filters used in the reconstruction are the quadrature mirror filters [95]. The image $u(x,y)$ is reconstructed from its wavelet transform by repeating this process for $-J \leq j \leq -1$. J was varied from 4 to 8.

5.7 Image Fusion Using Wavelet Transform

Using the multiple input linear minimum mean square error filter, we derive an approximate form of a filter which can be used without an explicit knowledge of the transfer functions associated with the degradation process. The estimated signal spectra is used to restore the signal. The fused image obtained using this approach appears to be satisfactory. The wavelet transform was shown as a tool for multi-resolution decomposition and used to fuse ultrasonic and eddy current images.

CHAPTER VI

CONCLUSIONS

6.1 Summary of Dissertation

Several image fusion methods have been presented in this dissertation. This chapter summarizes the work done in this dissertation and suggests areas for pursuing additional research activity. Data fusion approaches presented in the dissertation range from those using neural networks, linear filters designed to minimize mean square error, to those based on sub-band decomposition and wavelet transforms.

The first technique makes use of a multilayer perceptron network for fusing the images. The MLP network is trained using known pixel values in the region of interest. The second technique employs radial basis function networks where the output image pixel values are a linear combination of the basis functions. The center and weight vectors associated with the basis function are calculated using known pixel values in the region of interest and the K-means clustering algorithm respectively. The eddy current and ultrasonic images fused using both MLP and RBF networks are compared with each other. The results are dependent on the quality of the images used for fusion. In general, however, the RBF network appears to offer better results relative to MLP networks.

Chapter IV presents a multiple input linear minimum mean square error filter for image fusion. Using the cross-correlation of multiple images that have undergone different degradation processes and statistical information about the additive noise, this method out-

performs reconstruction algorithms that employ a single filter. The performance improvement is evident both from the expression for the mean square error as well as experimental results.

An approximate form of the filter was also derived for the situation where we do not have the degradation transfer function, noise, or signal spectrum. Results obtained using the approximate filter indicate the validity of the approach.

Chapter V presents image fusion methods based on frequency domain techniques. By partitioning the spectral domain into several sub-regions, the spectrum for each sub-region can be estimated. These estimates are then employed to estimate the fused image. The method is based on the assumption that the transfer functions associated with the degradation are functions of frequency and the signals in the each sub-band experience similar degradation effects.

Experimental results presented in chapter V involving the use of wavelet transforms as a tool for decomposing image into sub-bands show that the method offers considerable promise.

6.2 Future Work

This dissertation introduces the use of optimal methods for fusing multiple images. In addition to the optimal methods, techniques relying on multi-resolution techniques are also presented. Using an approach similar to that used for deriving the LMMSE fusion filter, it may be possible to derive an optimal filter for the multi-resolution procedure also.

Chapter III presented neural network based image fusion methods while Chapter IV described LMMSE filter based fusion methods. It may be an interesting exercise to determine if the neural network and LMMSE filter based methods implemented in parallel can produce data that can be compared and fused with each other. This step would constitute a second level of fusion.

In this dissertation, only pixel level data fusion techniques are studied. Alternative procedures utilizing features such as boundaries of shapes may offer better performance or reduced computational effort.

BIBLIOGRAPHY

- [1] E. Waltz and J. Llinas, *Multisensor Data Fusion*, Boston, MA: Artech House, 1990.
 - [2] S. Kai, S. Udpa and L. Udpa "Data Fusion for Electromagnetic NDE - A Feasibility Study," to be appear on *Progress in Electromagnetics Research Symposium*, Washington, Seattle, 1995.
 - [3] M. A. Abidi, and R. C. Gonzalez, *Data Fusion in Robotics and Machine Intelligence*. Boston, MA: Academic Press, 1992.
 - [4] D. L. Hall, *Mathematical Techniques in Multisensor Data Fusion*, Artech House, Inc., MA, 1992.
 - [5] Y. Barniv and D. Casasent, "Multisensor Image Registration: Experimental Verification," *Proc. SPIE, Process. Images and Data from Optical Sensors*, vol. 292, San Diego, CA, pp. 160-171, 1981.
 - [6] A. Akerman III, "Pyramidal Techniques for Multisensor Fusion," *Sensor Fusion V*, SPIE vol. 1828, pp. 124-131, 1992.
 - [7] R. Haberstroh and I. Kadar, "Multi-Spectral Data Fusion Using Neural Networks," *Signal Processing, Sensor Fusion, and Target Recognition II*, SPIE vol. 1955, pp. 65-75, 1993.
 - [8] J. Yim, S. S. Udpa, L. Udpa and M. Mina, "Fusing Ultrasonic Image and Eddy Current Image Using Radial Basis Function," *Proceedings of the 3rd Annual Midwest Electro-Technology Conference*, Ames, IA. pp. 10-13, April, 1994.
 - [9] M. Abdulghafour and M. A. Abidi, "Data Fusion Through Non-Deterministic Approaches - A Comparison," *Sensor Fusion VI*, SPIE vol. 2059, pp. 37-53, 1993.
 - [10] T. Huntsberger and B. Jawerth, "Wavelet Based Sensor Fusion," *Sensor Fusion VI*, SPIE vol. 2059, pp. 488-498, 1993.
 - [11] I. Edwards, X. E. Gros, D. W. Lowden and P. Strachan, "Fusion of NDT Data," *British Journal of NDT*, vol. 35, no. 12, pp. 710-713, December 1993.
 - [12] T. E. Bell, "When bust is best," *IEEE Spectrum*, vol. 28, pp. 56 - 59, March 1991.
-

- [13] H. L. Libby, *Introduction to Electromagnetic Nondestructive Test Methods*, New York, NY: Wiley-Interscience, 1971.
 - [14] L. Udpa and W. Lord, "A Discussion of the Inverse Problem in Electromagnetic NDT," in *Review of Progress in Quantitative Nondestructive Evaluation* vol. 5, Edited by D. O. Thompson and D. E. Chimenti, New York, NY: Plenum, pp. 375-382, 1985.
 - [15] J. Blitz. *Electrical and Magnetic Methods of Nondestructive Testing*, Bristol, Philadelphia : Adam Hilger, 1991.
 - [16] R. Halmshaw, *Non-destructive testing*, London, Baltimore: Edward Arnold Publishers Ltd., 1987.
 - [17] S. R. Satish, "Parametric Signal Processing for Eddy Current NDT," Ph.D. Dissertation, Colorado State University, Fort Collins, CO, 1983.
 - [18] W. Lord and R. Palanisamy, "Development of Theoretical Models for Nondestructive Testing Eddy-Current Phenomena," *Eddy-Current Characterization of Materials and Structures, ASTM STP 722*, George Birnbaum and George Free, Eds., American Society for Testing and Materials, pp. 5-21, 1981.
 - [19] R. Palanisamy and W. Lord, "Finite Element Analysis of Eddy Current Phenomena," *Materials Evaluation*, Philadelphia, PA: ASNT, pp. 39-43, October 1980.
 - [20] N. Ida and W. Lord, "Finite Element Model for Three Dimensional Eddy Current NDT Phenomena," *IEEE Transactions on Magnetism*, vol. MAG-21, no. 6, pp. 2635-2643, November 1985.
 - [21] D. J. Hagemaiier, "Eddy Current Impedance Plane Analysis," *Materials Evaluation*, vol. 41, Philadelphia, PA: ASNT, pp. 211-218, February 1983.
 - [22] R. E. Beissner and J. L. Fisher, "A Model of Pulsed Eddy Current Crack Detection," in *Review of Progress in Quantitative Nondestructive Evaluation* vol. 5A, Edited by D. O. Thompson and D. E. Chimenti, New York, NY: Plenum, pp. 189-197, 1985.
-

- [23] D. L. Waidelech, "Pulsed Eddy-Current Testing of Steel Sheets," In *Eddy-Current Characterization of Materials and Structures*, edited by G. Birnbaum and G. Free, pp. 367-373. Philadelphia, PA: ASNT, 1979.
- [24] Z. Mottl, "The Quantitative Relations between True and Standard Depth of Penetration for Air-Cored Probe Coils in Eddy Current Testing," *NDT International*, vol. 23. no. 1, pp. 11-17, February 1990.
- [25] N. Ida and W. Lord, "Simulating Electromagnetic NDT Probe Fields," *IEEE Transactions on Magnetics*, vol. 21, pp. 21-28, May/June 1985.
- [26] N. Ida, R. Palanisamy, and W. Lord, "Eddy Current Probe Design Using Finite Element Analysis," *Materials Evaluation*, vol. 41, Philadelphia, PA: ASNT, pp. 1389-1394, November 1983.
- [27] W. Lord, Y. S. Sun, S. S. Udpa and S. Nath, "A Finite Element Study of the Remote Field Eddy Current Phenomenon," *IEEE Transactions on Magnetics*, vol. 24, no. 1, pp. 435-438, January 1988.
- [28] W. Lord. "Applications of Numerical Field Modeling to Electromagnetic Methods of Nondestructive Testing," *IEEE Transactions on Magnetics*, vol. MAG-19, no. 6, pp. 2437-2442, November 1983.
- [29] D. E. Bray and R. K. Stanley, *Nondestructive Evaluation: A Tool for Design, Manufacturing, and Service*. New York, NY: McGraw-Hill, 1989.
- [30] R. W. E. Shannon and L. Jackson, "Flux Leakage Testing Applied to Operational Pipelines," *Materials Evaluation*, vol. 46, Philadelphia, PA: ASNT, pp. 1516-1524, 1988.
- [31] W. Lord and D. J. Oswald, "Leakage Field Methods of Defect Detection," *International Journal of NDT*, vol. 4 ,pp. 249-274, 1972.
- [32] W. Lord and J. H. Hwang, "Defect Characterization from Magnetic Leakage Fields," *British Journal of NDT*, pp. 14-18, January 1977.
- [33] W. Lord, J. M. Bridges, W. Yen, and R. Palanisamy, "Residual and Active Leakage Fields Around Defects in Ferromagnetic Materials," *Materials Evaluation*, vol. 36, Philadelphia, PA: ASNT, pp. 47-54, 1978.

- [34] J. F. Hinsley, *Non-destructive Testing*. London: MacDonald and Evans Ltd., 1959.
- [35] W. Lord, "A Survey of Electromagnetic Methods of Nondestructive Testing," Chapter 3 in *Mechanics of Nondestructive Testing*, edited by W. W. Stinchcomb, New York, NY: Plenum Press, pp. 77-100, 1980.
- [36] S. R. Satish, "Finite Element Modeling of Residual Magnetic Phenomena," M.S. Thesis, Colorado State University, Fort Collins, CO, 1980.
- [37] R. C. McMaster, *Nondestructive Testing Handbook II*. New York: Ronald Press Co., 1959.
- [38] W. C. Harmon, "Automatic Production Testing of Electric Resistance Welded Steel Pipe," *Materials Evaluation*, pp. 136-144, Philadelphia, PA: ASNT, March 1966.
- [39] J. R. Barton, F. N. Kuesenberger, R. E. Beissner, and G. A. Matzkanin, "Advanced Quantitative Nondestructive Evaluation Methods - Theory and Experiment," *Nondestructive Evaluation of Materials*, Edited by J. J. Nurke and V. Weiss, New York, NY: Plenum Publishing Co., pp. 435-477, 1979.
- [40] W. J. McGonnagle, *Nondestructive Testing*. 2nd ed., New York, NY: Gordon and Breach Science Publishers, 1966.
- [41] L. Udpa and W. Lord, "A Search-Based Imaging System," *IEEE Expert*, pp. 18-26, Winter 1989.
- [42] W. Lord and D. J. Oswald, "The Generated Reaction Field Method of Detecting Defects in Steel Bars," *Materials Evaluation*, vol. 29, no. 2, Philadelphia, PA: ASNT, pp. 21-28, 1971.
- [43] F. Förster, "Non-destructive Inspection of Tubing and Round Billets by Means of Leakage Flux Probes," *British Journal of NDT*, vol. 19, pp. 26-32, January 1977.
- [44] W. Lord, "Magnetic Flux Leakage for Measurement of Crevice Gap Clearance and Tube Support Plate Inspection," *EPRI NP-1427, Project S125-1, Final Report*, June 1980.
- [45] L. Udpa, "Imaging of Electromagnetic NDT Phenomena," Ph.D. Dissertation, Colorado State University, Fort Collins, CO, 1986.

- [46] C. A. Balanis, *Advanced Engineering Electromagnetic*, New York, NY: Wiley, 1989.
 - [47] J. Krautkramer and H. Krautkramer, *Ultrasonic Testing of Materials*, 4th Edition, Berlin; New York: Springer-Verlag, 1990.
 - [48] G. S. Kino, *Acoustic Waves: Devices, Imaging, and Analog Signal Processing*, Englewood Cliffs, NJ: Prentice-Hall, 1987.
 - [49] B. A. Auld, *Acoustic Fields and Waves in Solids*, 2nd ed. , Malabar, Fla.: Robert E. Krieger Publishing Company, 1990.
 - [50] W. Lord, D. Hsu, S. Ghoryayeb, A. Minachi, and Z. You, "Finite Element Application in NDE Engineering," *Ultrasonics International 91 Conference Proceedings*, pp. 464-466, 1991.
 - [51] J. Stolte, L. Udpa, and W. Lord, "Multifrequency Eddy Current Testing of Steam Generator Tubes using Optimal Affine Transformation," in *Review of Progress in Quantitative Nondestructive Evaluation* vol. 7, Edited by D. O. Thompson and D. E. Chimenti, New York, NY: Plenum, pp. 821-830, 1987.
 - [52] C. W. Gilstad, M. F. Dersch and R. DeNale, "Multi-frequency Eddy Current Testing of Ferromagnetic Welds," in *Review of Progress in Quantitative Nondestructive Evaluation*, vol. 9. Edited by D. O. Thompson and D. E. Chimenti, New York, NY: Plenum, pp. 1363-1370, 1990.
 - [53] L. Udpa, W. Lord and S. S. Udpa, "Frequency Domain Methods for the Analysis of Multi-Frequency Eddy Current Data," in *Review of Progress in Quantitative Nondestructive Evaluation* vol. 8, Edited by D. O. Thompson and D. E. Chimenti, New York, NY: Plenum, 1988.
 - [54] H. Djelouah, J. C. Baboux and M. Perdrix, "Experimental Determination of the Impulse Response of Axisymmetric Focused Ultrasonic Transducers," *J. Phys. D: Appl. Phys.* vol. 23. pp. 1135-1142, 1990.
 - [55] C. H. Chen and S. K. Sin, "Application of High Resolution Deconvolution Techniques To Ultrasonic NDE," *Acoustical Imaging*, vol. 18, Edited by H Lee and G. Wade, New York, NY: Plenum Press, pp. 163-177, 1991.
-

- [56] S. K. Sin and C. H. Chen, "A Comparison of Deconvolution Techniques for the Ultrasonic Nondestructive Evaluation of Materials," *IEEE Transactions on Image Processing*, vol. 1, no. 1, pp. 3-10, January 1992.
 - [57] B. G. Frock and R. W. Martin, "Digital Image Enhancement for Ultrasonic Imaging of Defects in Composite Materials," *Materials Evaluation*, vol. 47, Philadelphia, PA: ASNT, pp. 442-447, April 1989.
 - [58] R. Ludwig and W. Lord, "Development in the Finite Element Modeling of Ultrasonic NDT Phenomena," in *Review of Progress in Quantitative Nondestructive Evaluation*, vol. 5, Edited by D. O. Thompson and D. E. Chimenti, New York, NY: Plenum, 1985.
 - [59] W. Lord and L. Udpa, "Imaging of Electromagnetic NDT Phenomena," in *Review of Progress in Quantitative Nondestructive Evaluation*, vol. 5, Edited by D. O. Thompson and D. E. Chimenti, New York, NY: Plenum, pp. 465-472, 1985.
 - [60] R. P. Lippmann, "An Introduction to Computing with Neural Nets," *IEEE ASSP Magazine*, vol. 4, no. 2, pp. 4-22, April 1987.
 - [61] D. S. Broomhead and D. Lowe, "Multivariable Functional Interpolation and Adaptive Networks," *Complex Systems 2*, Complex Systems Publications, Inc. pp. 321-355, 1988.
 - [62] D. R. Hush and B. G. Horne, "Progress in Supervised Neural Networks," *IEEE Signal Processing Magazine*, pp. 8-39, January 1993.
 - [63] D. R. Kincaid, and W. Cheney, *Numerical Analysis*, Belmont, CA: Brooks/Cole, 1990.
 - [64] S. C. A. Thomopoulos and N. N. Okello, "Design and Experimental Validation of a Multiband Radar Data Fusion System," *Sensor Fusion*, SPIE vol. 2059, pp. 26-36, 1993.
 - [65] R. B. Thompson and D. O. Thompson, "Ultrasonics in Nondestructive Evaluation," *Proceedings of the IEEE*, vol. 73, no 12, pp. 1716-1755, December 1985.
 - [66] R. S. Gilmore, K. C. Tam, J. D. Young and D. R. Howard, "Acoustic Microscopy From 10 to 100 MHz for Industrial Application," *Phil. Trans. R. Soc.*, vol. A 320, London, pp. 215-235, 1986
-

- [67] H. K. Wickramasinghe, "Scanning Acoustic Microscopy: a Review," *Journal of Microscopy*, vol. 129, Pt 1, London : The Royal Microscopical Society, pp. 63-73, January 1983.
- [68] M. G. Somekh, H. L. Bertoni, G. A. D. Briggs and N. J. Burton, "A Two-dimensional Imaging Theory of Surface Discontinuities with the Scanning Acoustic Microscope," *Proc. R. Soc.*, London, vol. A 401, pp. 29-51, 1985.
- [69] C. B. Scurby, C. W. Lawrence, D. G. P. Fatkin, G. A. D. Briggs, A. Dunhill, A. E. Gee and C-L Chao, "Non-Destructive Testing of Ceramics by Acoustic Microscopy," *Br. Ceram. Trans. J.* vol. 88, pp. 127-131, 1989.
- [70] S. P. Neal, P. L. Speckman, and M. A. Enright, "Flaw Signature Estimation in Ultrasonic Nondestructive Evaluation Using the Wiener Filter with Limited Prior Information," *IEEE Transactions on Ultrasonics, Ferroelectrics, and Frequency Control*, vol. 40, no. 4, July 1993.
- [71] C. W. Lawrence, C. B. Scruby, G. A. D. Briggs and A. Dunhill, "Crack detection in Silicon Nitride by Acoustic Microscopy", *NDT International*, Butterworth & Co, pp. 3-10, February 1990.
- [72] J. Yim, S. S. Udpa, and L. Udpa, "Image Fusion Using Multi-Resolution Decomposition Techniques," *Proceedings of the 4th Annual Midwest Electro-Technology Conference*, Ames, IA, 1995.
- [73] S. G. Mallat, "A Theory for Multiresolution Signal Decomposition: The Wavelet Representation", *IEEE Transactions on Pattern Analysis and Machine Intelligence*, vol. 2, no. 7, pp. 674-692, July 1989.
- [74] J. W. Woods, "Subband Coding of Images", *IEEE Transactions on Acoustics, Speech, and Signal Processing*, vol. ASSP-34, no. 5, pp. 1278-1288, October, 1986.
- [75] W. Li and Y. Zhang, "A Study of Vector Transform Coding of Subband - Decomposed Images", *IEEE Transactions on Circuits and Systems for Video Technology*, vol. 4, no. 4, pp. 383-391, August, 1994.
- [76] A. Papoulis, *Probability, Random Variables, and Stochastic Processes*, New York, NY: McGraw-Hill, Inc., 1965.

- [77] W. Li, "Vector Transform and Image Coding", *IEEE Transactions on Circuits and Systems for Video Technology*, vol. 1, no. 4, pp. 297-307, December 1991.
 - [78] R. E. Ziemer and W. H. Tranter, *Principles of Communication*, Houghton Mifflin co., 1976.
 - [79] T. N. Cornsweet, *Visual Perception*, New York, NY: Academic Press, 1970.
 - [80] S. Hecht. "The Visual Discrimination of Intensity and the Weber-Fechner Law." *J. Gen. Physiol.* 7, 241, pp. 235-267, 1924.
 - [81] A. N. Netravali and B. Prasada. "Adaptive Quantization of Picture Signals Using Spatial Masking." *Proceedings of the IEEE*, vol. 65, pp. 536-548, April 1977.
 - [82] A. K. Jain, *Fundamentals of Digital Image Processing*, Englewood Cliffs, NJ: Prentice-Hall, pp. 51-52, 1989.
 - [83] A. Rosenfeld and M. Thurston, "Edge and Curve Detection for Visual Scene Analysis", *IEEE Transactions on Computer*, vol. C-20, no. 5, pp. 562-569, May 1971.
 - [84] S. G. Mallat, "Multifrequency Channel Decomposition of Images and Wavelet Models," *IEEE Transactions on Acoustics, Speech and Signal Processing*, vol. 37, no. 12, pp. 2091-2110, December 1989.
 - [85] J. Max, "Quantizing for Minimum Distortion," *Transactions on IRE Information Theory*, vol. 6, pp. 7-14, March 1960.
 - [86] A. Rosenfeld and M. Thurston, "Coarse-Fine Template Matching", *IEEE Transactions on System, Man, Cybern.*, vol. SMC-7, pp. 104-107, February 1977.
 - [87] J. Koenderlink, "The Structure of Images," in *Biological Cybernetics*. New York: Springer-Verlag, pp. 363-370, 1984.
 - [88] W. Grimson, "Computational Experiments with a Feature Based Stereo Algorithm," *IEEE Transactions on Pattern Analysis and Machine Intelligence*, vol. PAMI-7, no. 1, pp. 17-34, January 1985.
 - [89] J. M. Jolion and A. Rosenfeld, *A Pyramid Framework for Early Vision : Multiresolution Computer Vision*, Dordrecht; Boston, MA: Kluwer Academic Publishers, 1994.
-

- [90] B. G. Frock, P. Karpur and M. J. Ruddell, "Effects of Axial-Wiener Deconvolution on the Lateral Resolution in Ultrasonic C-Scan Images," in *Review of Progress in Quantitative Nondestructive Evaluation* vol. 10A, Edited by D. O. Thompson and D. E. Chimenti, New York, NY: Plenum, pp. 781-788, 1991.
- [91] P. J. Burt and E. H. Adelson, "The Laplacian Pyramid as a Compact Image Code," *IEEE Transactions on Communication*, vol. COM-31, no. 4, pp. 532-540, April 1983.
- [92] B. Julesz, "Textons, the Elements of Texture Perception and Their Interactions," *Nature*, vol. 290, no. 12, pp. 91-97, March 1981.
- [93] P. W. Besslich, "Pyramidal Transforms in Image Processing and Computer Vision," *Pyramidal Systems for Computer Vision*, Edited by V. Cantoni and S. Levialdi, Berlin, Springer-Verlag, vol. F 25, pp. 215-246, 1986.
- [94] A. Grossmann and J. Morlet, "Decomposition of Hardy Functions into Square Integrable Wavelets of Constant Shape," *SIAM Journal on Mathematical Analysis*, vol. 15, pp. 723-736, 1984.
- [95] P. P. Vaidyanathan, "Quadrature Mirror Filter Banks, M-Band Extensions and Perfect Reconstruction Techniques," *IEEE ASSP Magazine*, vol. 4, no. 3, pp. 4-20, July 1987.
- [96] J. Yim, S. S. Udpa, L. Udpa, M. Mina and W. Lord, "Neural Network Approaches to Data Fusion," in *Review of Progress in Quantitative Nondestructive Evaluation*, vol. 14A, Edited by D. O. Thompson and D. E. Chimenti, New York, NY: Plenum, pp. 819-826, August 1994.
- [97] F. Mokhtarian, and A. Mackworth, "Scale-Based Description and Recognition of Planar Curves and Two-dimensional Shapes," *IEEE Transactions on Pattern Analysis and Machine Intelligence*, vol. PAMI-8, no. 1, pp. 34-43, 1986.
- [98] J. Babaud, A. P. Witkin, M. Baudin, and R. O. Duda, "Uniqueness of the Gaussian Kernel for Scale-Space Filtering", *IEEE Transactions on Pattern Analysis and Machine Intelligence*, vol. PAMI-8, no. 1, pp. 26-33, 1986.
- [99] O. Rioul and M. Vetterli, "Wavelets and Signal Processing", *IEEE Signal Processing Magazine*, pp. 14-38, October 1991.
-

- [100] L . G. Weiss, "Wavelets and Wideband Correlation Processing", *IEEE Signal Processing Magazine*, pp. 13-32, January 1994.
 - [101] J. W. Woods, *Subband Image Coding*, Boston, MA: Kluwer Academic Publishers, 1991.
 - [102] M. B. Henke-Reed, "Cloth Texture Classification Using the Wavelet Transform", *Journal of Imaging Science and Technology*, vol. 37, no. 6, pp. 610-614, November/December 1993.
 - [103] L. H. Siew, R. M. Hodgson, and E. J. Wood, "Texture Measure for Carpet Wear Assessment", *IEEE Transactions on Pattern Analysis and Machine Intelligence*, vol. 10, no. 1, pp. 92-105, January 1988.
 - [104] I. Daubechies, *Ten Lectures on Wavelets*, CBMS-NSF Regional Conference Series in Applied Mathematics, vol. 61, Philadelphia, PA: Society for Industrial and Applied Mathematics, 1992.
 - [105] B. Jawerth and Wim Sweldens, "An Overview of Wavelet Based Multiresolution Analysis", vol. 36, no. 3, SIAM, pp. 377-412, September 1994.
 - [106] M Kunt, A. Iknomopoulos, and M. Kocher, "Second-Generation Image-Coding Techniques," *Proceedings of the IEEE*, vol. 73, no. 4, pp. 549-574, April 1985.
 - [107] J. Katto, J. Ohki, S. Nogaki, and M. Ohta, "A Wavelet Codec with Overlapped Motion Compensation for Very Low Bit-Rate Environment", *IEEE Transactions on Circuits and Systems for Video Technology*, vol. 4, no. 3, pp. 328-338, June 1994.
 - [108] P. P. Vaidyanathan, "Multirate Digital Filters, Filter Banks, Polyphase Networks, and Applications: A Tutorial," *Proceedings of the IEEE*, vol. 78, no. 1, pp. 56-93, January 1990.
-